Water mass variability in the eastern South Pacific and the ventilation of the oxygen minimum zone

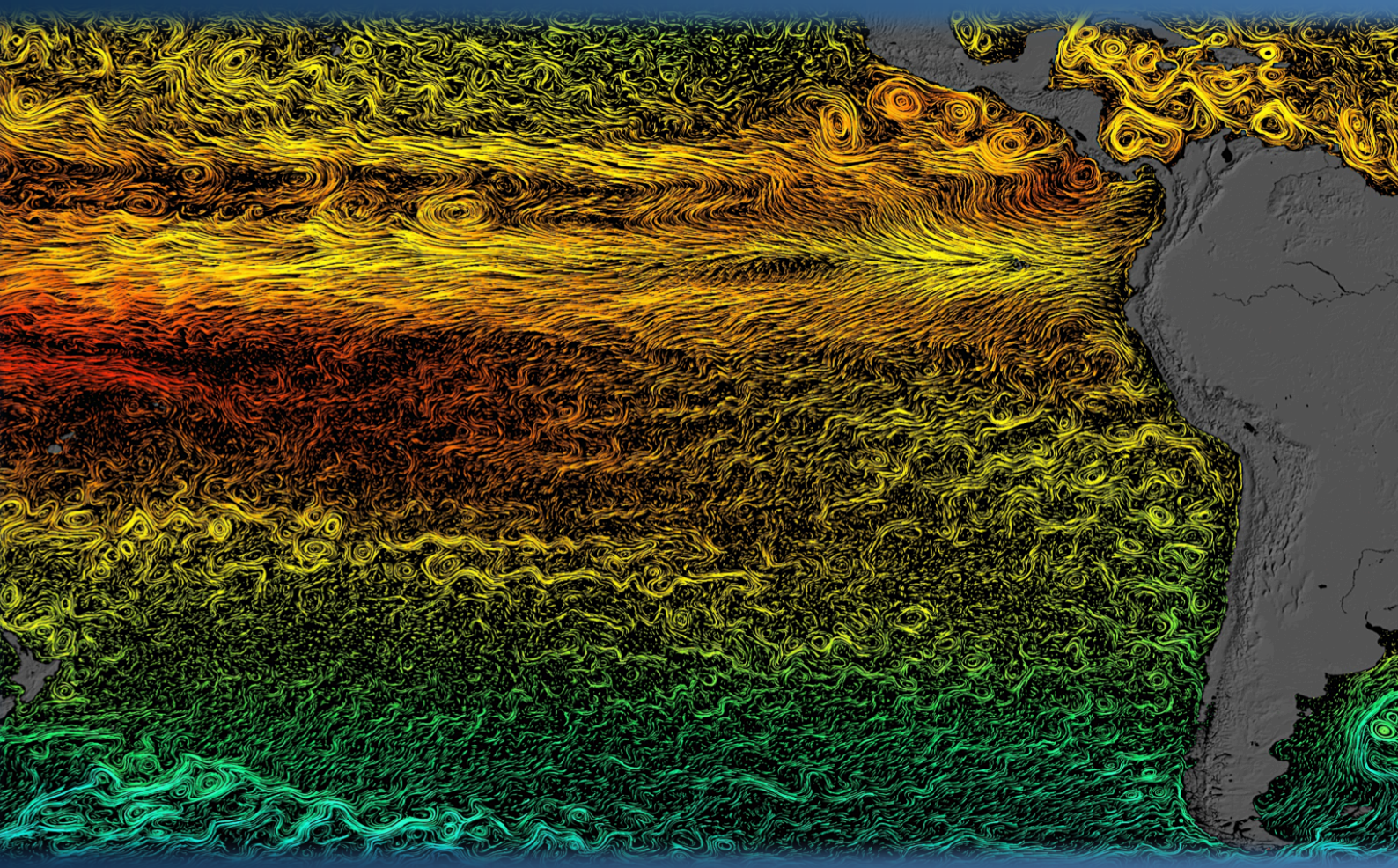

Pedro José Llanillo del Río

Barcelona, Septiembre 2014

Water mass variability in the Eastern South Pacific and the ventilation of the oxygen minimum zone

Pedro José Llanillo del Río

Barcelona, a 25 de Septiembre de 2014

Tesis presentada para obtener el título de Doctor por la Universitat Politècnica de Catalunya
Programa de Doctorado en Ciencias del Mar.
Departament d'Enginyeria Hidràulica, Marítima i Ambiental

Director: José Luis Pelegrí Llopart

Instituto de Ciencias del Mar
Departamento de Oceanografía Física y Tecnológica
Consejo Superior de Investigaciones Científicas (CSIC)
Laboratorio Internacional de Cambio Global (CSIC-PUC)

“How inappropriate to call this planet Earth when it is quite clearly Ocean.”
Arthur C. Clarke

A mi madre y a mi hermano,
A los que tuvisteis que partir antes de tiempo,
A Bea.

Cover: Sea surface currents and temperatures on the eastern Pacific Ocean from ECCO2 High Resolution Ocean and Sea Ice Model. Source: NASA/Goddard Space Flight Center Scientific Visualization Studio. http://svs.gsfc.nasa.gov/goto?3912

“Only the ocean remains as the last great unexplored portion of our globe; so it is to the sea that man must turn to meet the last great challenge of exploration this side of outer space.”
H. B. Stewart

PREFACE

This dissertation, entitled WATER MASS VARIABILITY IN THE EASTERN SOUTH PACIFIC AND THE VENTILATION OF THE OXYGEN MINIMUM ZONE, is presented as a partial requirement to obtain the Doctoral degree from the Universitat Politècnica de Catalunya. This investigation is the compilation of three studies aimed at describing the water mass structure and its variability under two opposite phases of ENSO, and to examine the pathways and terms involved in the ventilation of the eastern South Pacific oxygen minimum zone. The research presented here was conducted between 2009 and 2014 under the guidance of Dr. José Luis Pelegrí Llopart, who is a Research Professor from the Marine Sciences Institute (ICM) – Council for Scientific Research (CSIC), mainly in the frame of the International Global Change Lab (LINCGlobal).

This doctoral dissertation is structured with an introductory chapter which describes the hydrography, circulation and variability found in the eastern South Pacific and summarizes the goals and chapters of the thesis. The following three chapters constitute the core of the dissertation; each of them is presented as a scientific article. While writing this thesis, the first two chapters have been published in peer-review international scientific journals (Ciencias Marinas and Biogeosciences) and the third article is in the last phases prior to its submission to a scientific journal. The thesis concludes with a discussion of the main results from this work, as well as with comments on potential future lines of research. Asides the above-mentioned articles, along this period of research the author of this thesis has engaged in three collaborative research stays abroad (Chile, Germany and USA), has presented his research at seven scientific conferences, has attend two international training schools and has participated in four research cruises.

ABSTRACT

The eastern South Pacific (ESP) is a key region of the world ocean with direct influence on the global climate. Two clear examples are the El Niño-Southern Oscillation (ENSO), which occurs in the Pacific but influences the weather worldwide, and the observed slowdown in the rise of global air temperatures since 2001, recently explained in terms of a more vigorous upwelling of cold waters in the ESP and in the Equatorial Pacific. Over the last decade, the oceanographic scientific community has turned its attention to the oxygen minimum zones (OMZs) found in the world oceans, with one of the most intense being located in the ESP. OMZs are apparently expanding under the ongoing global warming, threatening productive marine habitats and weakening the ocean's ability to sequester atmospheric carbon dioxide by promoting nitrogen loss. Inside suboxic OMZs, the oceanic-fixed nitrogen is released to the atmosphere, partially as nitrous oxide, a powerful greenhouse gas that further disrupts the atmospheric radiative balance.

This dissertation aims at extending our knowledge of the ESP OMZ through two main approaches. The first approach is based on tracer analysis and inverse modeling techniques. Such techniques are applied to hydrographic datasets in order to examine the water mass structure, its variability and its role on the ventilation of the ESP OMZ. The second approach brings a more dynamical perspective to the study of the ventilation of the ESP OMZ, with the assessment of the annual-mean advective and turbulent oxygen transports into the ESP OMZ from Argo and dissolved oxygen datasets.

We describe the distribution of water masses offshore Chile, Peru and Ecuador and discuss their spreading pathways. A thorough characterization of the water masses has been accomplished, resulting in the first set of ESP water types accounting for inorganic nutrients and dissolved oxygen. The low oxygen waters that compose the ESP OMZ are mainly Equatorial Subsurface Water (ESSW). The ESP OMZ is ventilated from the south by the Antarctic Intermediate Water (AAIW) and by the shallower Subantarctic Water (SAAW). These water masses are transported into this region by the Peru Chile Current (PCC) or by the adjacent flow that forms part of the subtropical gyre.

We also examine the changes induced by two opposite phases of ENSO in water mass distribution and biogeochemical activity. During La Niña, vigorous upwelling promotes the rise in depth of the upper part of the ESP OMZ and denitrification strengthens in the subsurface layer. Furthermore, the upward displacement of isopycnals induced by La Niña favors the ventilation of a different depth range of the OMZ by the upper portion of the AAIW. The opposite occurs during El Niño conditions. We find that, with a larger oxygen supply, respiration increases balancing most of the extra oxygen gain. This suggests that there is an excess of organic matter waiting to be remineralized whenever oxygen supply increases slightly and this situation favors the maintenance of the ESP OMZ. Furthermore, our results show that AAIW flowed along shallower isopycnals in 2009 than in 1993. Such shoaling is not caused by the ENSO phenomenon and changes the way AAIW ventilates the ESP OMZ. This finding might explain why an increase in oxygen content has been reported between 200 and 700m off Chile.

A global picture of the main processes and predominant paths of oxygen supply into ESP OMZ is provided here for the first time. Two main advective routes are found, the traditional equatorial pathway and a previously unreported subtropical pathway. Remarkably, the subtropical pathway provides more net oxygen gain than the equatorial pathway at the core of the ESP OMZ. This finding challenges the common assumption that the ESP OMZ is only ventilated by the eastward flowing zonal currents of the Equatorial Current System. This result is endorsed by the independent water mass analyses accomplished in the first part of this dissertation where the fingerprint of AAIW and SAAW is clearly found in the ESP OMZ. In addition, an unreported eastward zonal current, located at intermediate depths between 12-15ºS, is found flowing all the way from the central Pacific into the ESP OMZ and its oxygen supply is quantified.

Mean advection dominates oxygen supply in the upper layers due to the large supply by the eastward flowing equatorial zonal currents. However, epineutral turbulent diffusion becomes the dominant term at levels deeper than $\gamma_n = 26.75$ kg m^{-3}. The annual mean oxygen budget for the whole volume of the ESP OMZ is unveiled. Epineutral turbulent diffusion provides a net oxygen supply of 417.4 ± 43.0 kmol s^{-1}, advection supplies 292.7 ± 25.2 kmol s^{-1} and dianeutral turbulent diffusion provides 85.8 ± 17.6 kmol s^{-1}. The mean biological consumption of oxygen required to close the budget is 795.9 ± 195.0 kmol s^{-1}.

RESUMEN

El Pacífico Suroriental (ESP) es una región clave del océano con influencia directa sobre el clima global. Dos claros ejemplos son el fenómeno de El Niño-Oscilación del Sur (ENSO), el cual sucede en el Pacífico pero altera el tiempo atmosférico a nivel mundial, y el reciente descubrimiento de que la ralentización observada desde el 2001 en el incremento de la temperatura media mundial se debe parcialmente a un fortalecimiento del afloramiento de aguas frías en el ESP. Durante la última década la comunidad científica ha puesto su atención en las zonas de mínimo de oxígeno (OMZs) del océano global, estando una de las más intensas localizada en el ESP. Las OMZs parecen estar expandiéndose con el cambio climático, esto amenaza la existencia de productivos hábitats marinos a la vez que provoca una pérdida del nitrógeno oceánico, y la pérdida de este nutriente debilita la productividad primaria oceánica y por tanto la capacidad del océano para secuestrar dióxido de carbono. Dentro de las OMZs con núcleo subóxico, el nitrógeno disuelto es degradado y liberado a la atmósfera en forma de varios gases, uno de ellos es un gas de potente efecto invernadero, el óxido nitroso, y su emisión altera aún más el balance radiativo de la atmósfera.

Esta tesis tiene como objetivo principal avanzar en el conocimiento de la OMZ del ESP a través de dos estrategias principales. La primera estrategia está basada en análisis de trazadores y en el uso de modelos inversos. Estos modelos han sido aplicados a datos hidrográficos con el objetivo de averiguar la distribución de masas de agua, su variabilidad y su papel en la ventilación de la OMZ del ESP. En la segunda estrategia se estudia la ventilación de la OMZ del ESP desde la perspectiva de la dinámica, mediante el cálculo de los transportes promedios anuales de oxígeno por advección y por turbulencia a partir de datos de oxígeno disuelto y de perfiladores Argo.

En esta tesis se describe la distribución de masas de agua del océano abierto frente a Chile, Perú y Ecuador y se discuten las rutas que siguen al esparcirse por el océano. Para ello se ha realizado una caracterización rigurosa las propiedades (valores tipo) de las mismas. Se proporciona aquí el primer conjunto de valores tipo de nutrientes y oxígeno disuelto para las masas de agua presentes en el ESP. El agua pobre en oxígeno que constituye la OMZ del ESP es principalmente Agua Ecuatorial Subsuperficial (ESSW). Dicha OMZ se ventila desde el sur con Agua Antártica Intermedia (AAIW) y, a niveles más someros, con Agua Subantártica (SAAW). Estas masas de agua llegan a esta región transportadas por la Corriente de Perú-Chile (PCC) o por el flujo adyacente que forma parte del giro subtropical situado más al oeste.

También se describen los cambios inducidos en la distribución de masas de agua y en la actividad biogeoquímica por fases opuestas del fenómeno ENSO. El vigoroso afloramiento característico de La Niña produce una ascensión en profundidad de la parte superior de la OMZ del ESP a la vez que favorece el proceso de denitrificación en capas subsuperficiales. La Niña induce un desplazamiento hacia capas más someras de las isopicnas y esto favorece la ventilación de un rango de profundidades distinto de la OMZ del ESP con la parte superior de la AAIW. Durante El Niño sucede lo contrario. Por otro lado, se ha observado que la respiración aumenta cuando se incrementa el aporte de oxígeno a

la OMZ, balanceando de esta manera la ganancia extra de oxígeno. Esto sugiere que existe un exceso de materia orgánica esperando a ser remineralizada en cuanto se produzca un ligero incremento en el aporte de oxígeno. Este exceso de materia orgánica favorece por tanto la estabilidad de la OMZ del ESP.

Nuestros resultados muestran que AAIW fluye en isopicnas más someras en 2009 respecto a 1993 y este cambio no es debido al fenómeno ENSO. Este cambio altera el patrón de ventilación de la OMZ del ESP por AAIW y podría ser la causa del incremento de oxígeno disuelto encontrado recientemente entre 200 y 700 m en el Pacífico chileno.

En esta tesis se proporciona la primera imagen global de los principales procesos y rutas de aporte de oxígeno a la OMZ del ESP. Se han encontrado dos rutas principales, la tradicional ruta ecuatorial y la inexplorada ruta subtropical. La ruta subtropical proporciona una mayor ganancia neta de oxígeno que la ruta ecuatorial en el núcleo de la OMZ del ESP. Este hallazgo desafía la asunción generalizada de que la OMZ del ESP se ventila únicamente por el Sistema Ecuatorial de Corrientes. Los análisis de masas de agua realizados en la primera parte de esta tesis de manera independiente respaldan dicho hallazgo al delatar la presencia de AAIW y SAAW en la OMZ del ESP.

Por otro lado, se ha descrito por primera vez una corriente que fluye hacia el este en capas intermedias entre 12-15ºS desde el Pacífico central hasta la región de la OMZ del ESP. El aporte de oxígeno de dicha corriente a la OMZ del ESP ha sido cuantificado aquí por primera vez.

En lo referente al aporte de oxígeno, la advección es el término dominante en las capas superiores debido al gran aporte de las corrientes ecuatoriales zonales que fluyen hacia el este. Sin embargo por debajo de $\gamma_n = 26.75$ kg m^{-3}, el término dominante es la difusión turbulenta epineutra de oxígeno. El balance medio anual de oxígeno para todo el volumen de la OMZ del ESP es el siguiente. La difusión turbulenta epineutra proporciona una ganancia neta de oxígeno de 417.4 ± 43.0 kmol s^{-1}, la advección aporta 292.7 ± 25.2 kmol s^{-1} y la difusión turbulenta dianeutra la difusión turbulenta epineutra 85.8 ± 17.6 kmol s^{-1}. Finalmente, el consumo biológico de oxígeno necesario para cerrar es 795.9 ± 195.0 kmol s^{-1}.

ACRONYMS LIST

AAIW: Antarctic Intermediate Water
ACC: Antarctic Circumpolar Current
ADCP: Acoustic Doppler Current Profiler
AOU: Apparent oxygen utilization
aOUR: Apparent oxygen utilization rate
AVISO: Archiving, Validation and Interpretation of Satellite Oceanographic data
CCC: Chile Coastal Current
CHC: Cape Horn Current
CT: Conservative temperature
CTD: Conductivity-Temperature-Depth
DT-MADT: Delayed-time maps of absolute dynamic topography
EIC: Equatorial Intermediate Current
EIC: Equatorial Intermediate Current
ENP: eastern North Pacific
ENSO: El Niño-Southern Oscillation
ESP: eastern South Pacific
ESSW: Equatorial Subsurface Water
EUC: Equatorial Undercurrent
GEOMAR: Helmholtz Centre for Ocean Research, Kiel, Germany
GLODAP: Global Ocean Data Analysis Project
IOC: Intergovernmental Oceanographic Commission
ITCZ: Intertropical Convergence Zone
LINCGlobal: Laboratorio Internacional de Cambio Global
NADW: North Atlantic Deep Water
NEC: North Equatorial Current
NECC: North Equatorial Counter Current
NEIC: North Equatorial Intermediate Current
NICC: North Intermediate Counter Current
NSCC: Northern Subsurface Counter Current
OMP: Optimum Multiparameter Analysis
OMZ: Oxygen minimum Zone
OMZs: Oxygen minimum zones
ONI: Oceanic Niño Index
PcC: Peru coastal Current
PCCC: Peru Chile Countercurrent
PCCS: Peru-Chile Current System
PDO: Pacific decadal oscillation
PDW: Pacific Deep Water

PIC: Polynesian Intermediate Current
PUC: Poleward Undercurrent
SA: Absolute salinity
SAAW: Subantarctic Water
SEC: South Equatorial Current
SECC: South Equatorial Counter Current
SEIC: South Equatorial Intermediate Current
SICC: South Intermediate Counter Current
SPC/WWD: South Pacific Current or West Wind Drift
SSAW: Summer Subantarctic Water
SSCC: Southern Subsurface Countercurrent
sSSCC: Secondary Southern Subsurface Countercurrent
STG: Subtropical gyre
STSW: Subtropical Surface Water
STW: Subtropical Water
Sv: Sverdrup (10^6 m^3 s^{-1})
TEOS-10: The new standard for the calculation of the thermodynamic properties of seawater
UCDW: Upper Circumpolar Deep Water
UCSD: University of California, San Diego, United States
WOA-13: World Ocean Atlas 2013
WOCE: World Ocean Circulation Experiment
XBTs: Expendable bathythermographs (XBTs)

LIST OF CONTENTS

Abstract…….. I

Resumen……...…….. III

Acronyms list ……. V

List of contents ……. VII

1- General introduction…… 1
1.1 Wind-driven circulation and interannual variability in the Eastern South Pacific…. 3
1.2 Water masses in the eastern South Pacific…….. 9
1.3 Oxygen minimum zones…….. 12
1.4 The eastern South Pacific oxygen minimum zone…… 16
1.5 Aims and outline of the thesis……..... 17

2- Meridional and zonal changes in water properties along the continental slope off central and northern Chile…… 19
2.1 Introduction…….. 22
2.2 Data set and Methodology…..……. 24
2.2.1 Data set……..... 24
2.2.2 Optimum Multi-Parameter Analysis…..……..... 25
2.2.3 Implementation of the classic OMP analysis..... 28
2.2.4 Implementation of the quasi-extended OMP analysis..... 30
2.3 Results…….……. 31
2.3.1 Vertical distribution of properties……..... 31
2.3.2 Property-property diagrams ……..... 34
2.4 Discussion..……..……. 36
2.4.1 Property-property diagrams per water type…….. 36
2.4.2 Vertical distributions per water type…… 37
2.5 Conclusions.....……..……. 40

3- Physical and biogeochemical forcing of oxygen and nitrate changes during El Niño/El Viejo and La Niña/La Vieja upper-ocean phases in the tropical eastern South Pacific along 86ºW……. 45
3.1 Introduction……...……... 48
3.2 Data and Methods…..……... 51
3.2.1 Observational data……..…….. 51
3.2.2 Extended Optimum Multi-Parameter analysis..... 52
3.2.3 Source water masses..... 54
3.3 Results…….……..……. 57
3.3.1 Water mass distribution……..……..... 57
3.3.2 Respiration and Denitrification…..……..... 61
3.3.3 Changes along 85º50’ W between 1993 and 2009……..... 62
3.3.3.1 Measured changes in oxygen and nitrate content..... 62
3.3.3.2 Changes in water mass distribution ……..……..... 64
3.3.3.3 Physical and biogeochemical contributions to oxygen and nitrate changes 66
3.4 Conclusions……..……..……. 68
3.5 Supplementary material…..……..……..……. 70

4- Oxygen supply pathways and closed oxygen budget for the Eastern South Pacific oxygen minimum zone ……. 75
4.1 Introduction…..……...……... 78
4.2 Data and Methods…..……... 80
4.2.1 Annual mean advective field……..…….....……. 81
4.2.2 Annual-mean turbulent diffusive field..... 83
4.2.3 Integrated transports..... 84
4.2.4 Closed oxygen budget terms..... 85
4.2.5 Error propagation analysis..... 87
4.3 Results…….……..……. 89

LIST OF CONTENTS

4.3.1 Oxygen supply pathways into the ESP OMZ..... 89
4.3.2 Oxygen supply terms and closed oxygen budget for the ESP OMZ..... 98
4.4 Conclusions…..…….…..……. 100

Conclusions and future research…… 103
References…… 111

Acknowledgements…… 125

CHAPTER

1

General Introduction

"Equipped with his five senses, man explores the universe around him and calls the adventure science."
Edwin Powell Hubble

1.1 Wind-driven circulation and interannual variability in the Eastern South Pacific

The mean upper-ocean circulation in the eastern South Pacific (ESP) is the result of large-scale atmospheric forcing (Strub et al., 1998). The atmospheric Hadley cell describes the vertical and meridional motions of air within the tropical and equatorial troposphere. At the poleward end of the Hadley cell, large-scale atmospheric circulation promotes air convergence at the top of the troposphere and thus subsidence of air towards the Earth's surface. This creates an area of high surface pressure centered at about 25-30ºS (depending on the season) known as the South Pacific anticyclone. In the absence of rotation, the resulting horizontal pressure gradient would drive air flow in the counter-gradient direction. However, because of the Earth's rotation, the Coriolis force causes this air flow to be deflected to its left, flowing approximately parallel to the isobars (anticlockwise in southern hemisphere) in near-geostrophic balance. At the atmospheric boundary layer, the friction with the surface breaks the geostrophic balance and causes the winds to cross the isobars with a small angle.

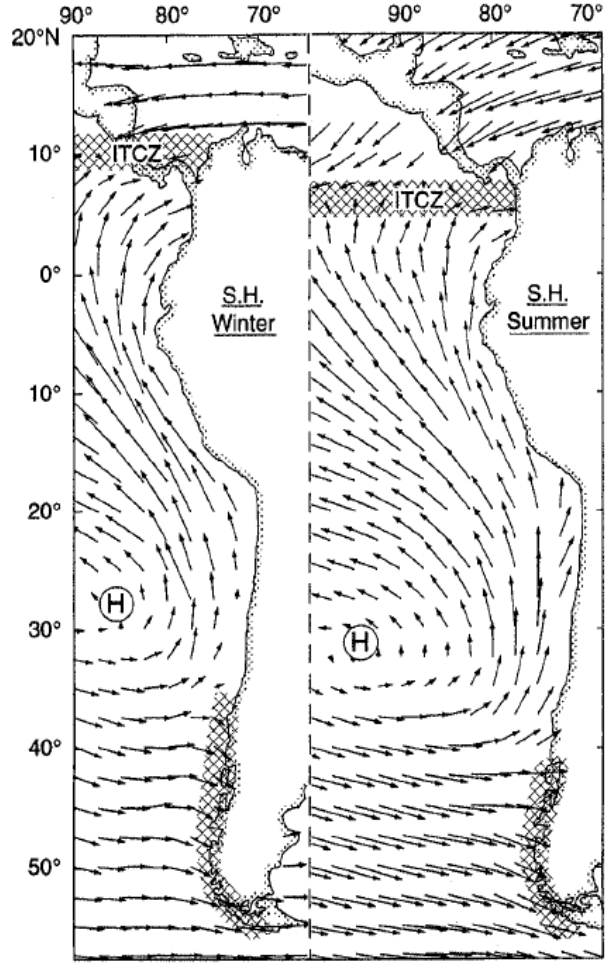

Figure 1. Climatological winds during austral winter and summer. Winds are from the NCEP reanalysis at 1000 mb, averaged over austral summer (December-February) and winter (June-August). Regions of heavy precipitation are shown by hatching. Source: From Strub et al. (1998).

The resulting bands of winds, the westerlies south of 30ºS and the trade winds north of this latitude, are of huge relevance for the circulation in the upper-ocean (Figure 1). They induce a net Ekman transport of surface water to the left of the winds (e.g. Talley et al., 2011). The waters pushed by the wind converge at about 20-30ºS (Figure 2a) leading to both their piling up and their subduction into the ocean interior (Ekman pumping). The outcome is the creation of horizontal pressure gradients, the characteristic bowl-shape of the isopycnals, and the induced equatorward Sverdrup's transport (Figure 2b) (e.g. Talley et al., 2011). Mirroring what happens in the atmospheric anticyclone, the geostrophic balance is achieved and the water flows anticlockwise (southern hemisphere) around contours of constant steric height (a proxy for isobars in the ocean) (Figure 3). This creates a huge wind-driven anticyclonic circulation feature known as the South Pacific subtropical gyre, which drives ocean circulation down to ~1800 m, where the horizontal pressure gradients vanish.

In this thesis we are interested in the mean circulation pattern in the eastern edge of the subtropical gyre, affecting the ESP region. At the southern part of the subtropical gyre, there is a broad eastward flow known as the West Wind Drift (WWD) or South Pacific Current (SPC) (Stramma et al., 1995). The weak SPC should not be confused with the energetic Antarctic Circumpolar Current (ACC), found poleward of the Subantarctic Front (Figure 2a). When the SPC approaches the South

(a)

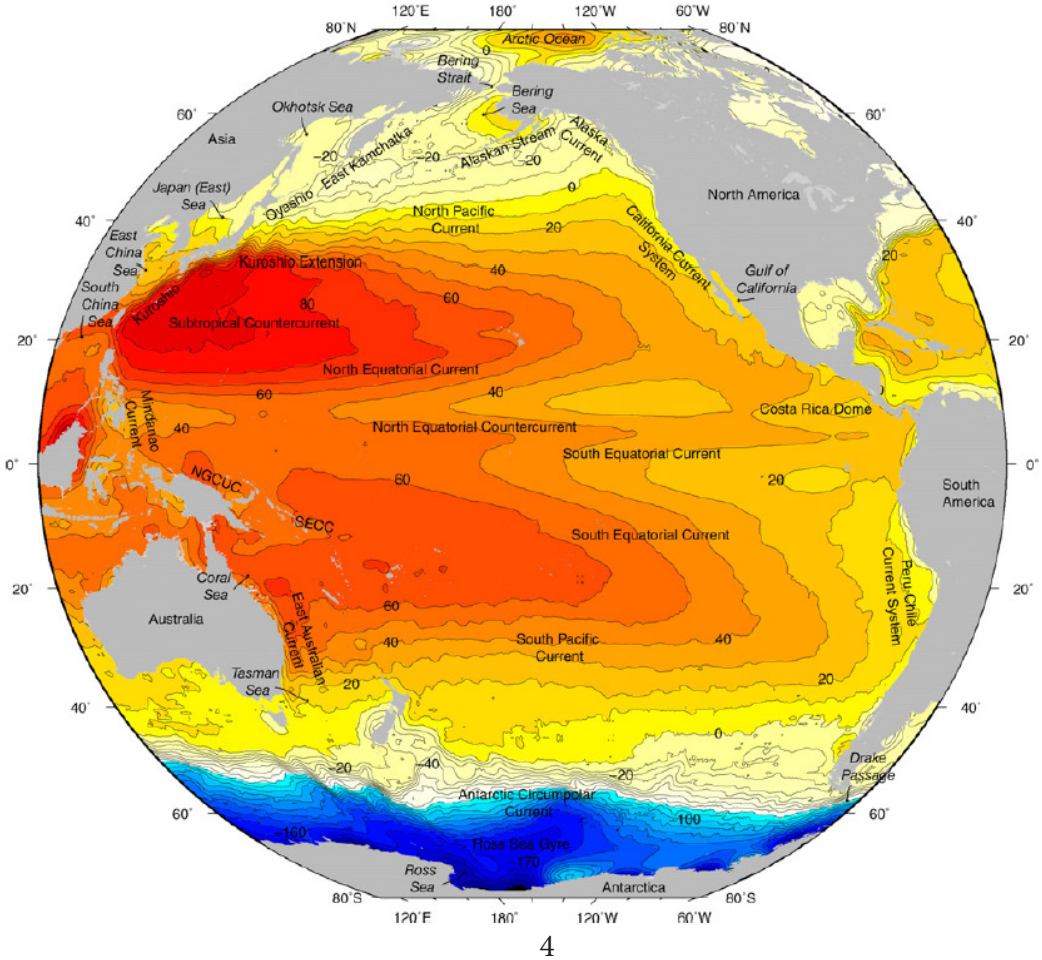

(b)

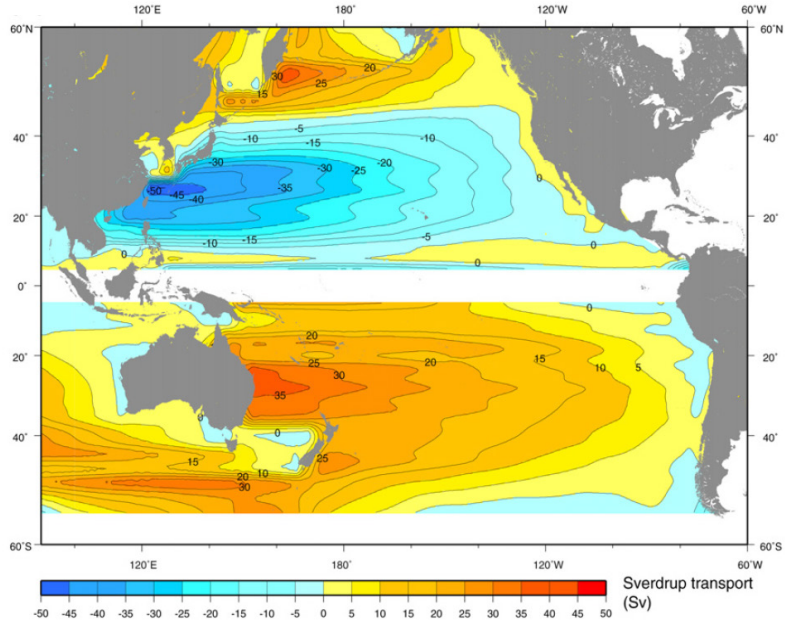

Figure 2. (a) Pacific Ocean: mean surface geostrophic circulation with the current systems described in this text. Mean surface height (cm) relative to a zero global mean height, based on surface drifters, satellite altimetry, and hydrographic data. (NGCUC: New Guinea Coastal Undercurrent and SECC: South Equatorial Countercurrent). Data from Niiler, Maximenko, and McWilliams (2003). **(b)** Sverdrup transport (Sv), where blue is clockwise and yellow-red is counterclockwise circulation. Data from NCEP reanalysis (Kalnay et al.,1996). Source: From Talley et al. (2011).

American coast it splits into two branches. One of them, the Cape Horn Current (CHC) flows poleward and joins the ACC crossing through the Hoces Sea (i.e. Drake Passage) into the South Atlantic Ocean (Strub et al., 1998). The other branch feeds the open-ocean portion of the equatorward Peru-Chile Current (PCC), also named the Humboldt Current (HC) (Silva et al. 2009). The PCC commonly refers to both the broad equatorward flow of the subtropical gyre and to the swifter eastern boundary current, although they have a different dynamic origin (Talley et al., 2011). Throughout this thesis we will use PCC/HC only to refer to the eastern boundary current and will use STG to refer to the equatorward flow of the easternmost part of the subtropical gyre. The PCC eventually connects with the South Equatorial Current (SEC) at about 14ºS (Czeschel et al., 2011). Most of the SEC flows towards the northwest within the subtropical gyre, but a fraction of its northern part flows across the equator (Strub et al., 1998). The SEC strengthens west of 85ºW at the equator as it gains mass from the eastward Equatorial Undercurrent (EUC) flowing below (Wyrtki, 1966).

The EUC is located outside the subtropical gyre and belongs to the Equatorial Current System (Figure 4). The EUC is the result of the zonal pressure gradient arising through the convergence of waters in the western end of the Pacific basin, transported by the westward flowing SEC and North Equatorial Current (NEC). The EUC flows eastward in the upper thermocline and is confined within

the equatorial channel by the Coriolis effect (e.g. Talley et al., 2011). The EUC rises in depth to the east and, during the boreal spring, reverses the usual westward flow at the surface from about 140ºW to at least 95ºW (Johnson et al., 2002). For the purpose of this thesis, we focus only on the eastward flowing currents of the Equatorial Current System. Besides the EUC, the southern Subsurface Counter Current (SSCC) or South Pacific Tsuchiya Jet (Tsuchiya 1975) flows eastward under the SEC between 4-6ºS. The intermittent flow of the weak South Equatorial Counter Current (SECC) is sometimes observed in the ESP. Czeschel et al. (2011) found the SECC at 12°S and 85°50′W and suggested that it may later rejoin the westward SEC.

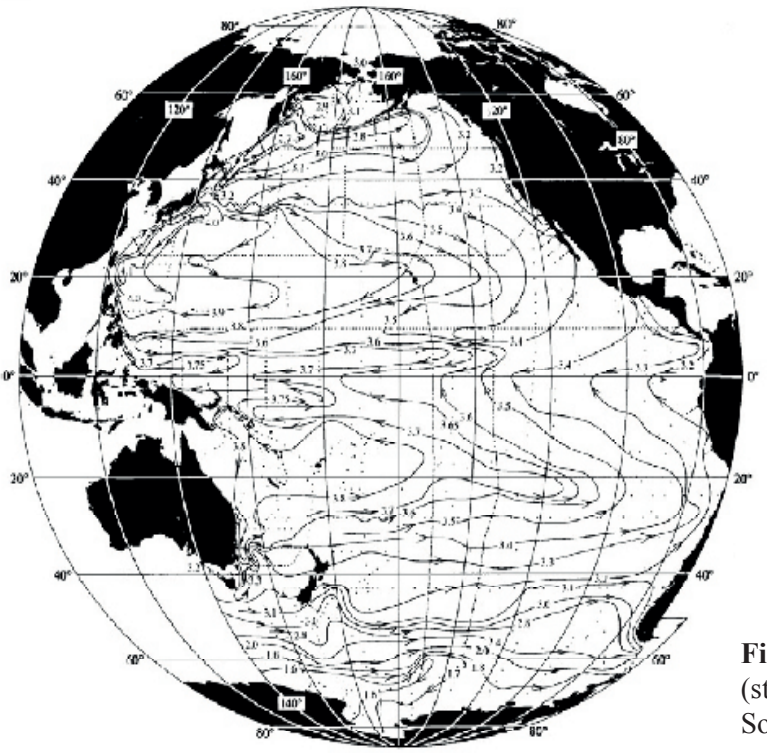

Figure 3. Adjusted geostrophic streamfunction (steric height, 10 m^2 s^{-2}) at the sea surface. Source: From Reid (1997).

The Peru-Chile Current System (PCCS) extends between 4ºS and 40°S at the eastern boundary of the South Pacific (Strub et al., 1998). The winds flow along the South American coast inducing Ekman transport divergence and thus upwelling of nutrient-rich waters that promote phytoplankton blooms (Figure 5). The PCCS is a complex system with mesoscale eddies, filaments of upwelled waters and several currents whose meridional limits change seasonally according to the location of the South Pacific atmospheric anticyclone. The eastern boundary current of the ESP (the PCC/HC), is the result of geostrophic adjustment between open-ocean waters and the denser waters upwelled along the coast (Talley et al., 2011). The PCC flows equatorward above ~500 m, taking place offshore of the upward sloping isothermals/isopycnals induced by the upwelling (Figure 6). Onshore of the continental slope, we still find two other meridional jets which are associated to the upwelling system (Strub et al., 1998). The first one is the Peru Coastal Current (PcC), which may be thought as an equatorward extension of the Chile Coastal Current (CCC). Furthermore, upwelling stretches the

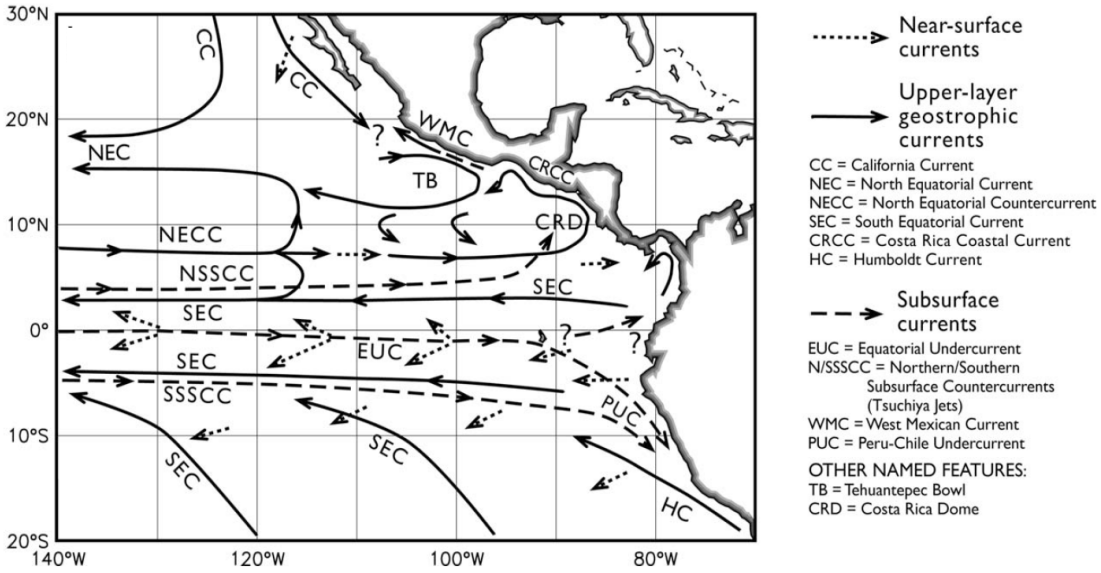

Figure 4. Schematic three-dimensional circulation in the eastern tropical Pacific based on modern data. The legend at the right lists the names of currents and features referred to in the text. Several question marks indicate regions where the interconnections among the currents remain unknown. Source: From Kessler et al. (2006).

water column upwards inducing poleward Sverdrup flow. Underneath and onshore from the PCC, the Poleward Undercurrent (PUC) flows over the continental slope. The PUC, also known as the Gunther Current, is recognized by the characteristic spreading of the isotherms/isopycnals, upward above the PUC and downward below it (Talley et al., 2011). The PUC carries high nutrient content and low oxygen values as it is fed by the EUC (Strub et al. 1998) with waters that spent a long time

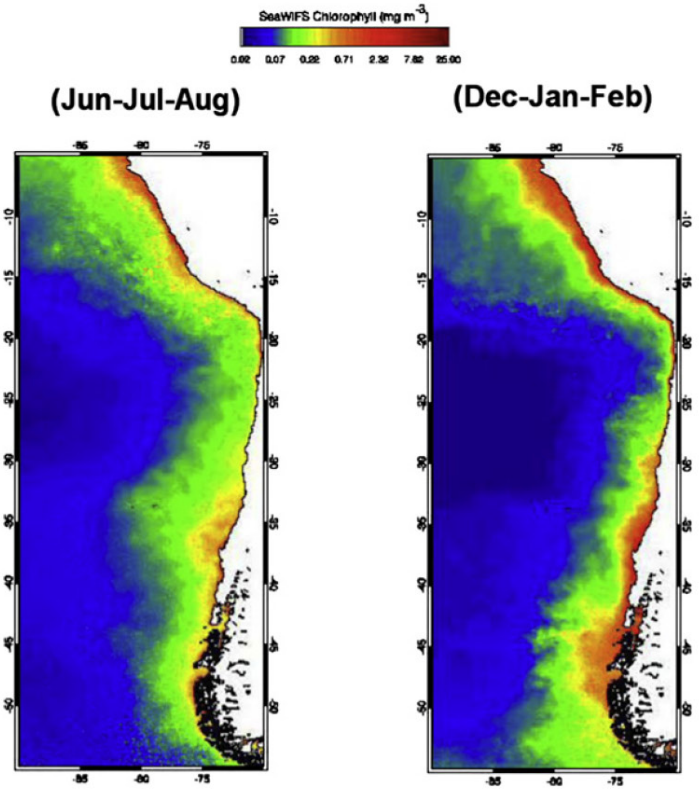

Figure 5. Surface chlorophyll concentration in austral winter (June, July, August) and summer (December, January, February), derived from SeaWiFS satellite observations. Source: From Mackas, Strub, Thomas and Montecino (2006).

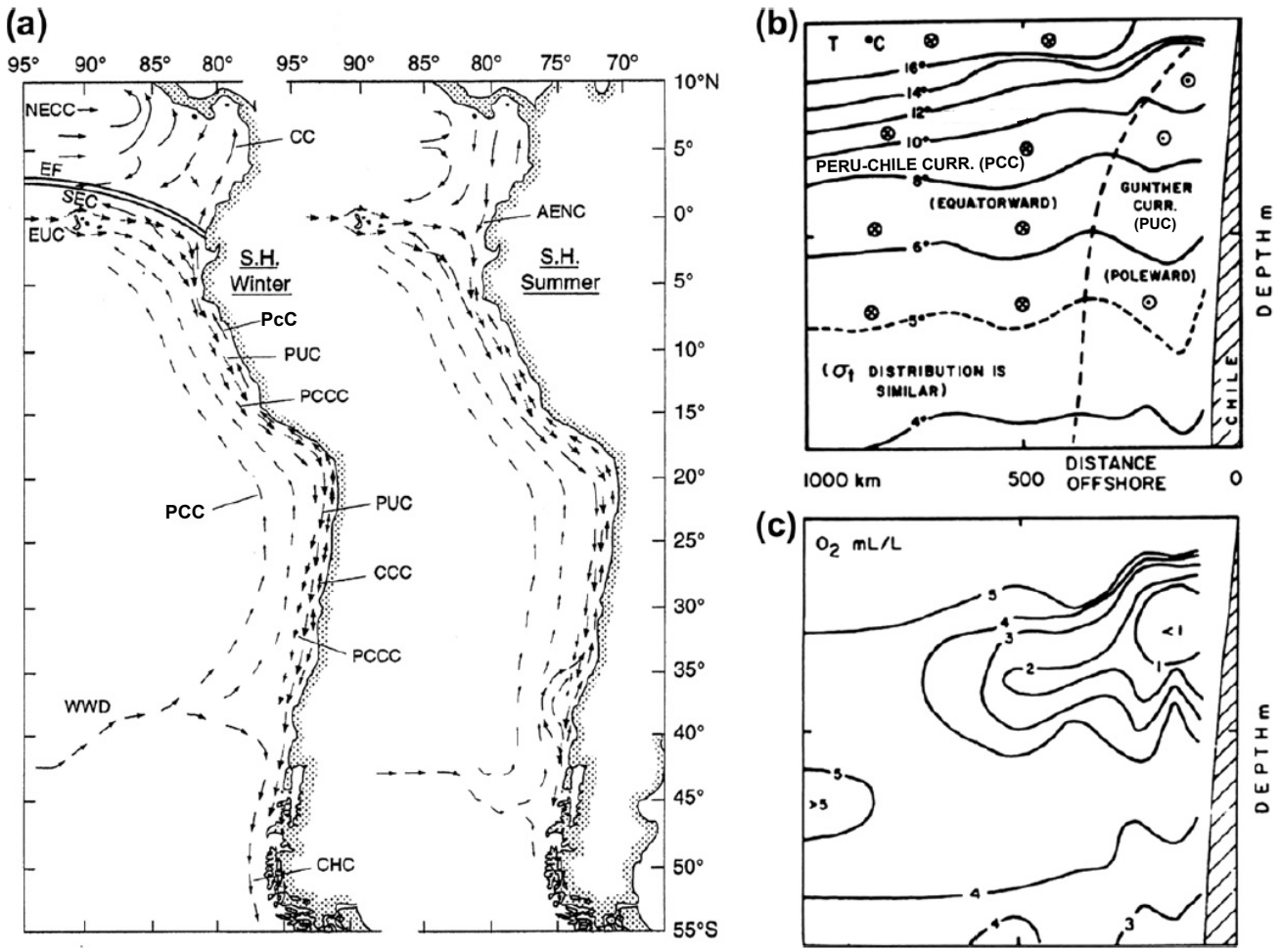

Figure 6. The Peru-Chile Current System: **a)** Maps in austral winter and summer. Acronyms: WWD, West Wind Drift; PCC, Peru-Chile Current; PCCC, Peru-Chile Countercurrent; PUC, Poleward Undercurrent; PcC, Peru Coastal Current; CCC, Chile Coastal Current; and CHC, Cape Horn Current. Also, near the equator: CC, Colombia Current; AENC, Annual El Niño Current; NECC, North Equatorial Countercurrent; SEC, South Equatorial Current; EUC, Equatorial Undercurrent. Eastern South Pacific zonal vertical sections at 33ºS: **b)** temperature (ºC) with meridional current directions and **c)** dissolved oxygen (ml L^{-1}). Source: Adapted from Strub et al. (1998) and Talley et al., (2011).

in a region with stagnant circulation. At about 100–300 km offshore, another poleward flow is found near the surface: the Peru-Chile Counter Current (PCCC) (Strub et al., 1998), which has been found to be connected to the SSCC (Czeschel et al., 2011).

The eastern Pacific is influenced by El Niño-Southern Oscillation (ENSO), one of the strongest modes of interannual variability in the global ocean/atmosphere system (Philander, 1983). The regional and global effects of ENSO are immense, in particular the ENSO phenomenon influences weather around the globe through atmospheric teleconnections (e.g. Talley et al., 2011). During an El Niño (warm) event the trade winds weaken and the upwelling off the South American coast is suppressed, bringing a major decrease in the primary production of this region and potentially leading to a collapse in the local fisheries (Barber and Chavez, 1983). The opposite occurs during a La Niña

(cold) event, with reinforced trade winds, more vigorous upwelling and increased primary production (Strub et al., 1998) (Figure 7).

This region is also under the influence of a longer variability mode known as the Pacific decadal oscillation (PDO) (Mantua et al., 1997; Chavez et al., 2003). As it happens with El Niño/La Niña, the PDO also oscillates between warm (El Viejo) and cold (La Vieja) phases. These oscillations induce changes in the sea surface height, sea surface temperature, thermocline depth and ocean currents. Since the middle to late 1990s the ESP has been found in a La Vieja phase (Chavez et al., 2003, 2008). The ESP has been recently blamed for part of the observed slowdown in the rise of global mean air temperatures due to a more vigorous upwelling (England et al., 2014).

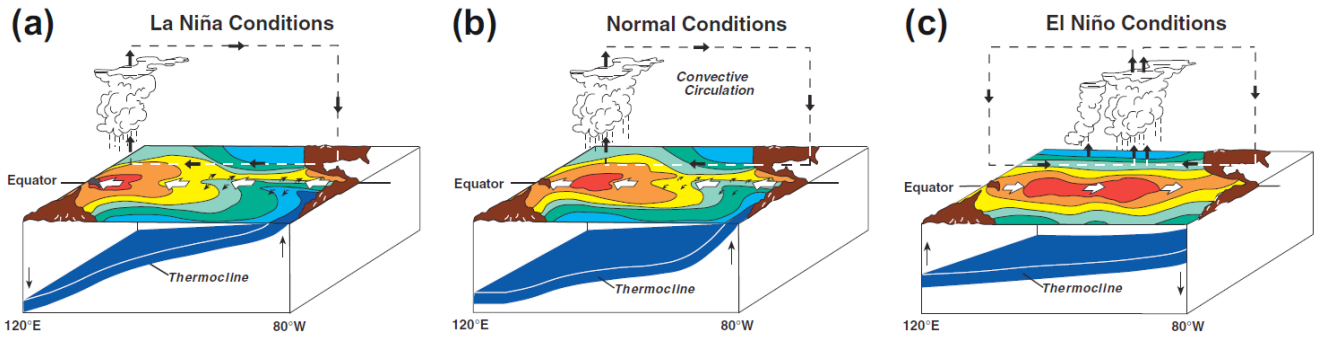

Figure 7. a) La Niña, **b)** normal, and **c)** El Niño conditions. Source: Talley et al. (2011) adapted from NOAA PMEL (2009).

1.2 Water masses in the eastern South Pacific

A volume of water formed in a particular region of the ocean, subject to some characteristic atmospheric conditions, is usually referred to as water mass. As a result of this atmospheric forcing, the water mass has some distinguishable hydrographic properties (water types). In addition, subsurface mixing is another plausible mechanism for water mass formation (Tomczak, 1999). Water mass formation can be seasonal or intermittent in time. In some instances the water mass may be formed during some specific season, typically after the intense subsurface mixing during the winter, as part of it gets below the shallower mixed layer in spring (Tomczak, 1999). When a surface water mass leaves its source region and flows below the mixed layer, carrying the atmospheric signature (dissolved gasses) and the hydrographic properties acquired in its formation region. As this water mass enters the ocean interior circulation it spreads mainly along neutral surfaces (Jacket and MacDougall, 1997), ageing and mixing progressively with other water masses. (Hereafter, we will refer to distributions over constant neutral-density surfaces as isoneutral distributions, while along- and across-isoneutral motions will be referred to as epineutral and dianeutral motions). Eventually, mixing and biogeochemical cycling erode its characteristic properties up to a point that the water mass is no longer recognizable (Tomczak, 1999).

Chapter 1

Ventilation of the ocean interior is achieved when young and oxygen-rich surface water masses reach below the mixed layer and join the geostrophic flow field of the ocean interior. This can be caused by wind-driven Ekman convergences that promote water mass subduction into the thermocline (i.e. the anticyclonic curl of the wind stress induces Ekman pumping) (Stommel, 1979; Luyten et al., 1983) or by vertical convection caused by density modifications due to the air-sea-ice buoyancy fluxes (e.g. the overturning circulation) (Tomczak, 1999). The waters subducted and entering the ocean interior spread their signature via large-scale advection (i.e. mean ocean currents) and turbulent diffusion (both epineutral and dianeutral). Turbulent diffusive processes can occur at many different scales, from mesoscale eddies (tens to hundreds of kilometres) to the local breaking of internal waves or double diffusion processes (scale of meters) (Fischer et al., 2013). Once a water mass has escaped from the surface mixed layer it becomes isolated from the atmosphere and its oxygen content starts to decrease due to the biological remineralisation of the dissolved organic matter (Redfield et al., 1963).

Several water masses are found in the ESP. Tsuchiya and Talley (1998) provide a description of such water masses based on the distribution of hydrographic properties observed during a meridional section (P19) along about 85°50'W (March 1993) within the frame of the World Ocean Circulation Experiment (WOCE). In addition, Leth et al. (2004) described water mass properties along three zonal transects carried out along 28º15', 35º15' and 43º15'S, from the Chilean coast to 86–88ºW (May–June 1995). Furthermore, Silva et al. (2009) have recently examined the water mass structure off Chile with a dataset from the SCORPIO (May–June 1967), PIQUERO (May–June 1969), and KRILL (June 1974) cruises. Fiedler and Talley (2006) provide a review of the water masses found in the eastern tropical Pacific (Figure 8).

The Subtropical Surface Water (STSW in Fiedler and Talley, 2006; STW in Silva et al., 2009; Tropical Surface Water in Tsuchiya and Talley, 1998) occupies the upper 200 m of the water column. It is formed in a region where evaporation exceeds precipitation (Stramma et al. 1995) in the South Pacific subtropical anticyclone (Wyrtki, 1967). Thus, it is a very salty (~35.2) and warm (~20 ºC) water mass (Silva et al., 2009). STW subducts northward of 10ºS into the upper thermocline creating a shallow salinity maximum in the upper 100 m (Fiedler and Talley, 2006). Closer to the coast, STW is advected poleward by the PCCC (Strub et al., 1998) and spreads as far south as the Subtropical Front (~35ºS), where it encounters another surface water mass originated farther south, the Subantarctic Water (SAAW) (Tsuchiya and Talley, 1998). SAAW originates north of the subantarctic front and flows north with the PCC (Wyrtki, 1967) and northwest within the South Pacific subtropical gyre. SAAW is formed under the stormy conditions of the sub-polar low pressure systems, where high rates of precipitation markedly reduce the salinity of the surface layers (Silva et al., 2009). Hence, it is a fresh (~33.8) and temperate (~11.5 ºC) surface water mass (Silva et al., 2009). SAAW is subducted

below STW near 35ºS as explained by Luyten et al. (1983), originating a Shallow Salinity minimum found at about 150-250 m depth (Tsuchiya and Talley, 1998; Leth et al. 2004) which partially ventilates the central layer before eroding completely.

The water mass found below STW (north of 15ºS) and below SAAW (between 35º-15ºS) at 150-250 m depth (shallower equatorward) is a mass of equatorial origin, the Equatorial Subsurface water (ESSW). ESSW is slightly less salty (~34.9) and colder (~12.5 ºC) (Silva et al., 2009) than the overlaying STW and presents low oxygen content (Leth et al., 2004). ESSW is centered at about 250 m depth and is advected mainly by the EUC (Stramma et al. 2010b) to the northeast of the subtropical gyre into a region known as 'the shadow zone' where, partly due to the long residence time (Wyrtki, 1967) and partly due to the intense biological activity, it loses most of its oxygen giving rise to an intense oxygen minimum zone (OMZ). The EUC eventually feeds the PUC, which flows along the continental slope spreading the ESSW southwards (Strub et al., 1998). Part of the nutrient rich ESSW within the PUC is occasionally upwelled along the coast (Brink et al. 1983), giving rise to a phytoplankton bloom and to an increase in the organic matter reaching below the photic zone; this organic matter will eventually be remineralized, reducing the dissolved oxygen available (Helly and Levin, 2004). ENSO warm events are believed to help extend the ESSW further south, by means of low frequency pulses of the PUC associated to the poleward propagation of Kelvin waves (Pizarro et al. 2002).

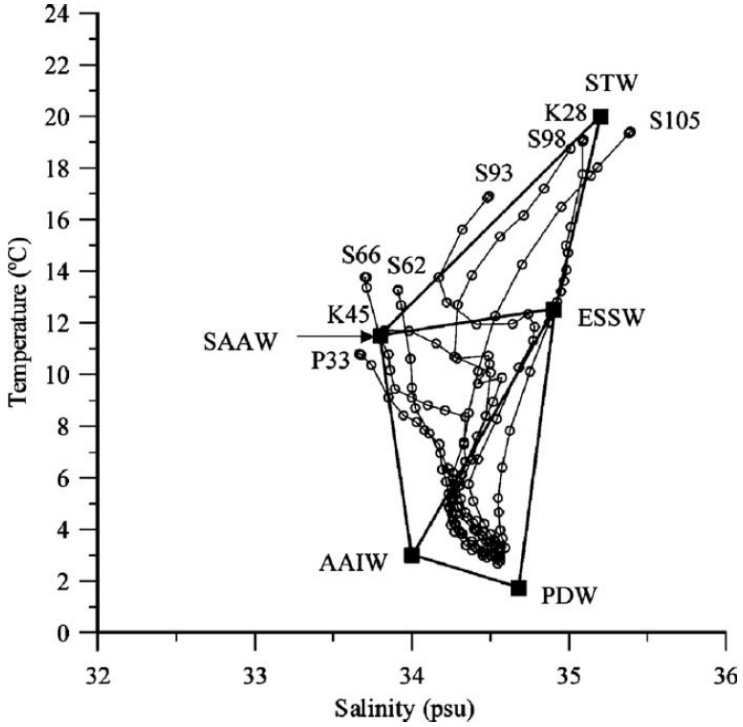

Figure 8. TS diagram for selected KRILL, SCORPIO and PIQUERO stations off Peru and Chile and mixing triangles (STW: Subtropical Water; SAAW: Subantarctic Water; ESSW: Equatorial Subsurface Water; AAIW: Antarctic Intermediate Water; PDW: Pacific Deep Water). Source: From Silva et al. (2009).

Below SAAW and ESSW, we find Antarctic Intermediate Water (AAIW). This water mass is formed by vertical convection of the deep winter mixed layer located north of the Polar Front (Hartin et al., 2011). AAIW spreads northward and westward within the South Pacific subtropical gyre, characterized by a salinity minimum (<34.5) found at 600-900 m depth (Tsuchiya and Talley, 1998). AAIW has been reported to fully cross the equator before completely losing its characteristics (Strub et al., 1998).

Below AAIW, we find North Pacific Deep Water (PDW), a colder (~1.75 ºC) and saltier (34.68) water mass mainly characterized by a broad silicate maximum, with its core located between 2500 and 3000 m depth (Tsuchiya and Talley, 1998). PDW spreads southward as a tongue of low dissolved oxygen (~105 μmol kg^{-1}) associated with slightly shallower cores of high nutrient values (Tsuchiya and Talley, 1998). PDW comes to this region following a complicated path through the North Pacific; it is believed to be the return flow of modified bottom waters originated at the South Pacific in the Antarctic Circumpolar Current (ACC) (Reid, 1973; Tsuchiya and Talley, 1998).

Near the bottom, flowing equatorward, we find the Upper Circumpolar Deep Water (UCDW), a water mass of similar salinity (~34.69) but colder (~1.23 ºC) and with much more dissolved oxygen (~176.6 μmol kg^{-1}) and less nutrients than the PDW (Tsuchiya and Talley, 1998). UCDW carries the signal of modified North Atlantic Deep Water (NADW) and flows out of the ACC into the Southeast Pacific Basin. UCDW spreads north over the Chile Rise to ventilate the bottom of the Chile Basin (Leth et al. 2004) from where it continues north until the Peru Basin through a gap between the Nazca and Sala y Gómez Ridges or through a deep passage along the Peru-Chile Trench (Tsuchiya and Talley, 1998). UCDW continues north into the Panama Basin through a gap in the Carnegie Ridge, greatly modified by both ageing and geothermal activity (Laird, 1971).

1.3 Oxygen minimum zones

The water volumes in the ocean with very low dissolved oxygen levels are known as oxygen minimum zones (OMZs) (Cline and Richards, 1972). OMZs provide hints of how life may have thrived in the primitive ocean (Paulmier and Ruiz-Pino, 2009). Permanent OMZs are found with different intensities in the upper thermocline at the eastern boundaries of the tropical Atlantic and Pacific Oceans (Karstensen et al., 2008) and in the northern Indian Ocean (Paulmier and Ruiz-Pino, 2009) (Figure 9; Table 1). Currently, there is no consensus upon which oxygen concentration should be used to delimit the boundary of an OMZ and such threshold is selected depending on the research interests of each study (Paulmier and Ruiz-Pino, 2009). Approximately, ~8% of the total oceanic surface area has permanent subsurface OMZs, with cores that reach suboxic values (<20 μM) (Paulmier and Ruiz-Pino, 2009).

The Atlantic and Pacific OMZs are located equatorward of the wind-driven subtropical gyres, within the sluggish circulation regions known as shadow zones. The combination of dynamical and biogeochemical factors can explain the existence of OMZs in these regions. The ventilation of the thermocline occurs mainly within the subtropical gyres, which connect the outcrop regions of the isopycnal surfaces at high latitudes with the anticyclonic recirculating ocean interior (Stommel, 1979; Luyten et al., 1983). In contrast, there is no direct connection between the outcrop regions and the shadow zones so little oxygen from the subtropical gyres is expected to reach the OMZs (Reid, 1965). In addition, the oceanic eastern boundaries are regions with high biological productivity due to the upwelling of nutrient-rich waters (Helly and Levin, 2004). This results in a large export of organic matter to the central layers where it is remineralized by microbial activity, leading to intense oxygen consumption (e.g. Kalvelage et al., 2013).

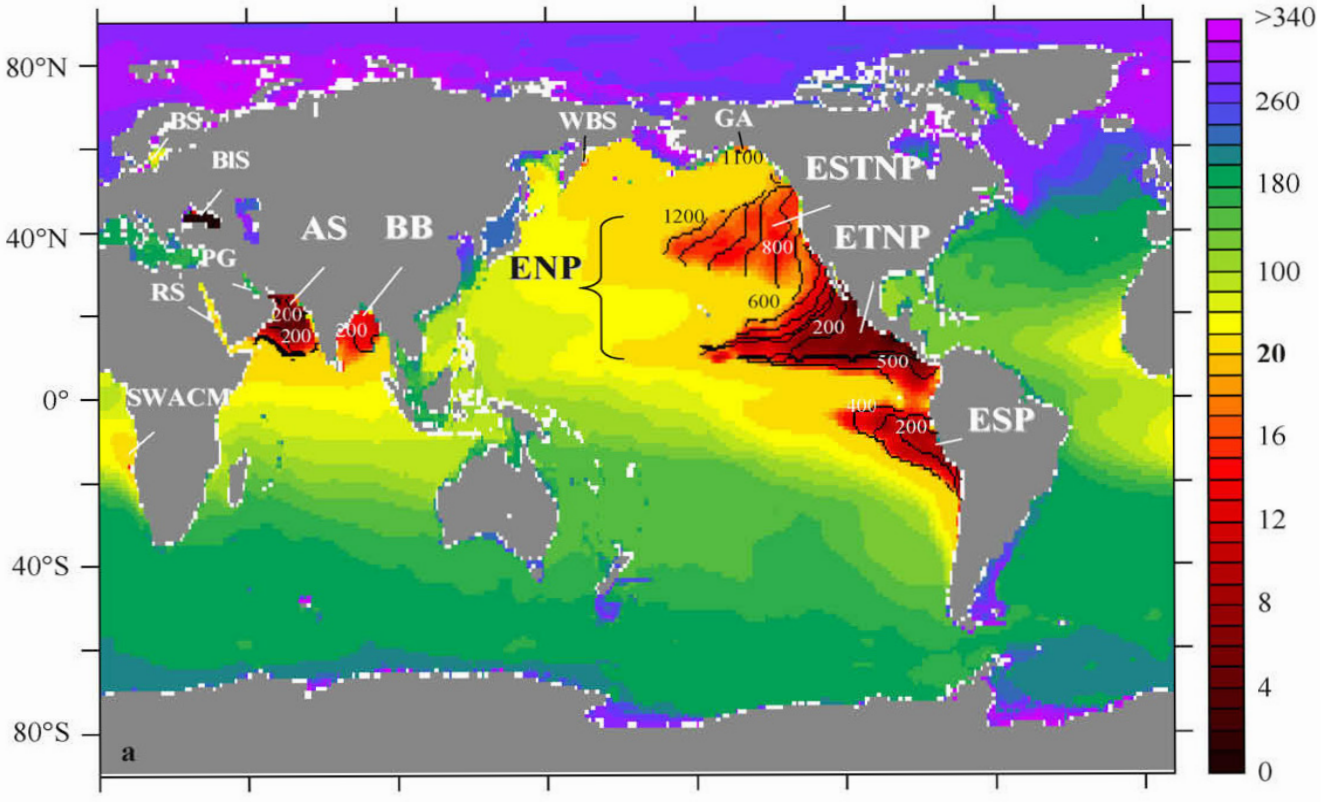

Figure 9. Oxygen distribution (µM) at depth where oxygen concentration is minimal, indicating the extent of the oxygen minimum zones (in red) according to the World Ocean Atlas 2005 (WOA-2005) 1º mean climatology. The color bar scale corresponds to a 1 ± 2 µM intervals between 0 and 20 µM, and a 20 ± 2 µM intervals between 20 and 340 µM. The isolines indicate the limit of the upper OMZ core depth in meters with a 100 m contour interval. Acronyms: AS: Arabian Sea; BB: Bay of Bengal; BlS: Black Sea; BS: Baltic Sea; ESP: eastern South Pacific; ESTNP: eastern subtropical North Pacific; ETNP: eastern tropical North Pacific; GA: Gulf of Alaska; PG; Persian Gulf; RS: Red Sea; SWACM: southwest African continental margin; WBS: western Bering Sea. Source: From Paulmier et al. (2009).

Table 1. Climatological summary of the mean characteristics of OMZs based on direct observations (GLODAP dataset, Sabine et al., 2005) and a gridded climatology (WHP-SAC, Gouretski and Jahnke, 1998). [a]Using 1 μmol kg^{-1} above and below the absolute minimum as threshold. Source: From Karstensen et al. (2008).

	Characteristics GLODAP dataset (σ_Θ < 27.2 kg m^{-3})			Total volume (10^{15} m^3), WHP-SAC (σ_Θ < 27.2 kg m^{-3})		
	O_2 minimum (μmol kg^{-1})	Depth of minimum (m)	σ_Θ of minimum (kg m^{-3})	O_2 < 4.5 μmol kg^{-1} (suboxic)	O_2 < 45 μmol kg^{-1} (GLODAP based σ_Θ range)	O_2 < 90 μmol kg^{-1} (GLODAP based σ_Θ range)
North Atlantic	~40	~420	~27.05	0	0 (26.96–27.08)	0.9 (26.5 to >27.2)
South Atlantic	~20	~400	~26.95	0	0.2 (26.50–27.15)	1.6 (26.3 to >27.2)
North Pacific	~0.1	250–400	26.0–27.2[a]	0.44	11.3 (24.5 to >27.2)	21.3 (23.5 to >27.2)
South Pacific	~0.3	150–300	26.2–26.8[a]	0.001	4.4 (26.0 to >27.2)	8.4 (25.5 to >27.2)
Indian Ocean	~0.3	100–650	24.1–27.2[a]	0.02	2.7 (23.0 to > 27.2)	6.1 (22.5 to >27.2)

OMZs play an important role in the carbon and nitrogen cycles (Bange et al., 2005). When oxygen levels fall below the suboxic upper threshold of 20 μM (~19.5 μmol kg^{-1}), the aerobic respiration decreases and nitrate (NO_3) instead of oxygen, begins to be used for the respiration of the organic matter (Smethie, 1987; Oguz et al., 2000; Paulmier and Ruiz-Pino, 2009). This is achieved via denitrification (i.e. the heterotrophic reduction of NO_3) through several steps, with gaseous dinitrogen (N_2) released to the atmosphere as the final product (Codispoti et al., 2001; Kalvelage et al., 2011). Although denitrification starts taking place at oxygen concentrations below 19.5 μmol kg^{-1}, this process is much more intense at concentrations <5 μmol kg^{-1} (Kalvelage et al., 2011). In the first step, NO_3 is reduced into nitrite (NO_2), which can be further reduced emitting nitrous oxide (N_2O), a powerful greenhouse gas; OMZs are responsible for at least 30% of all natural N_2O released to the atmosphere (Naqvi et al., 2010). Alternatively, NO_2 can enter the anammox process, i.e. the anaerobic oxidation of ammonium (NH_4^+) with NO_2, which produces N_2 and water as the final products (Kuypers et al., 2005; Lam et al., 2009; Kalvelage et al., 2011). Anammox is considered to be the most important pathway for nitrogen removal within the OMZs (Kuypers et al., 2005; Thamdrup et al., 2006; Hamersley et al., 2007; Kalvelage et al., 2011). The combination of denitrification and anammox processes leads to the loss of ~20–40% of the global oceanic-fixed nitrogen (Gruber, 2004). Consequently when these waters eventually upwell to the photic zone, nitrogen becomes a limiting nutrient for phytoplankton growth, weakening the biological sequestration of atmospheric carbon dioxide (Kalvelage et al., 2011).

Under global warming conditions, disrupted atmosphere-ocean buoyancy fluxes are expected to decrease dissolved oxygen levels in the ocean as less oxygen can be dissolved in warmer waters (Keeling and Garcia, 2002; Bopp et al., 2002; Plattner et al., 2002; Frölicher et al., 2009). Furthermore, increased stratification may shift the thermocline ventilation patterns to shallower isopycnals with direct implications for the OMZs.

Decreasing oxygen concentration and expansion of the OMZs have been found for all tropical oceans (Stramma et al., 2008, 2010b), possibly partially related to a long-term decadal type variability (Deutsch et al., 2011). Model studies also predict the expansion of the OMZs under global warming

conditions (Matear and Hirst, 2003; Schmittner et al., 2008; Shaffer et al., 2009). Models reproduce well the global trend of oxygen decrease but they are yet limited at correctly reproducing the regional oxygen changes (Stramma et al., with Oschlies 2012b). The model results are largely influenced by the parameterization of diapycnal mixing (Duteil and Oschlies 2011) and by their capacity of resolving mesoscale eddies (Duteil et al., 2014).

Expansion of the OMZs may disrupt the marine ecosystems and reduce the habitable depth range for marine organisms (Figure 10); these factors, superimposed with overfishing, may threaten the sustainability of the important pelagic fisheries maintained by the high biological productivity overlying the OMZs (Vaquer-Sunyer and Duarte; 2008, Keeling et al., 2010; Stramma et al., 2012a). Another impact of the expansion of the OMZs will be an increased loss of dissolved oceanic-fixed nitrogen, with immediate consequences for ocean primary production and the carbon cycle (Kalvelage et al., 2013), together with the release of larger amounts of the powerful greenhouse gas N_2O.

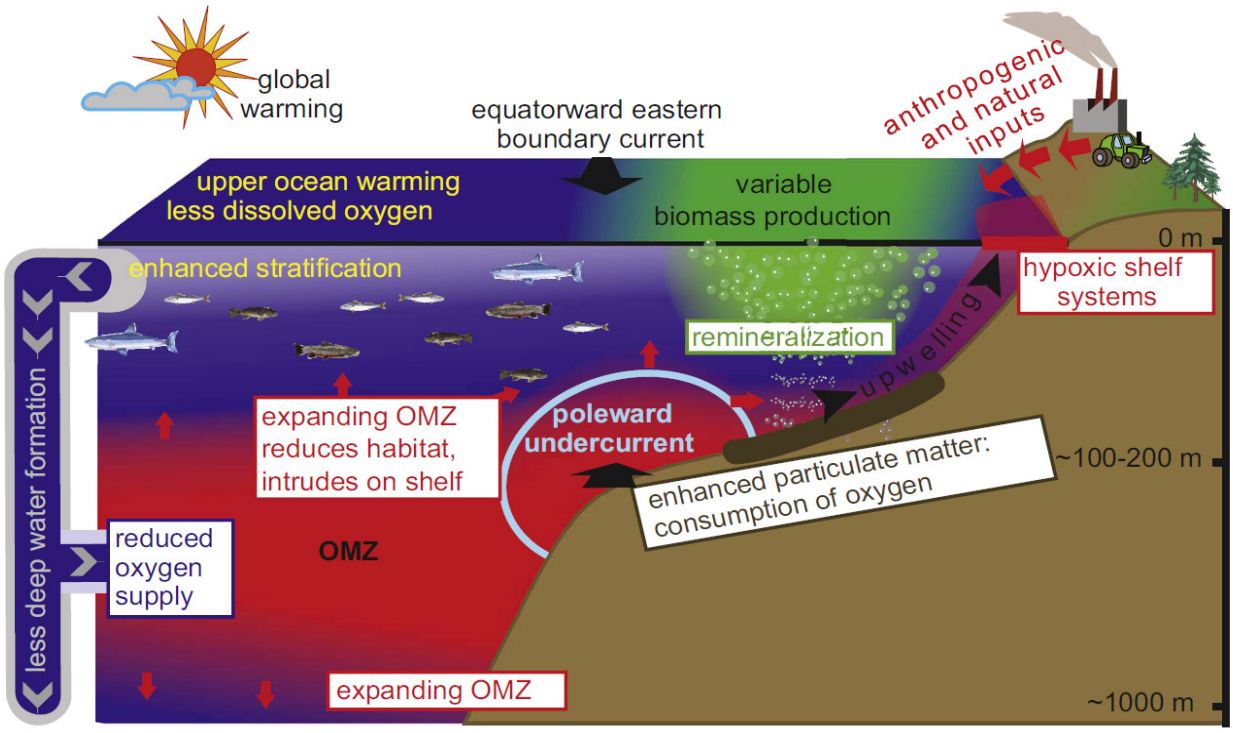

Figure 10. Schematic of interactions of open ocean oxygen minimum zones (OMZ, red) with hypoxic shelf systems and dead zones (Diaz and Rosenberg, 2008) on continental shelves of eastern ocean boundaries. Source: From Stramma et al. (2010b).

1.4 The eastern South Pacific oxygen minimum zone

The eastern South Pacific oxygen minimum zone (ESP OMZ) is located offshore Equator, Peru and Chile, in the shadow zone of the South Pacific subtropical gyre, north of those regions directly ventilated by the South Pacific thermocline (Reid, 1965; Stommel, 1979; Luyten et al., 1983). Consequently, the ESP OMZ is reached by sluggish currents bringing waters that will spend, in average, a long time in this region. Almost all the oxygen provided by physical transport is consumed by an intense biological activity in the oxycline underlying the rich ESP upwelling system (Paulmier et al., 2006). Consequently, the ESP OMZ appears as the result of the combination of poor ventilation by mean ocean currents and high biological oxygen demand due to the large export of organic matter to subsurface lavers from the nutrient-rich surface waters.

(a)

(b)

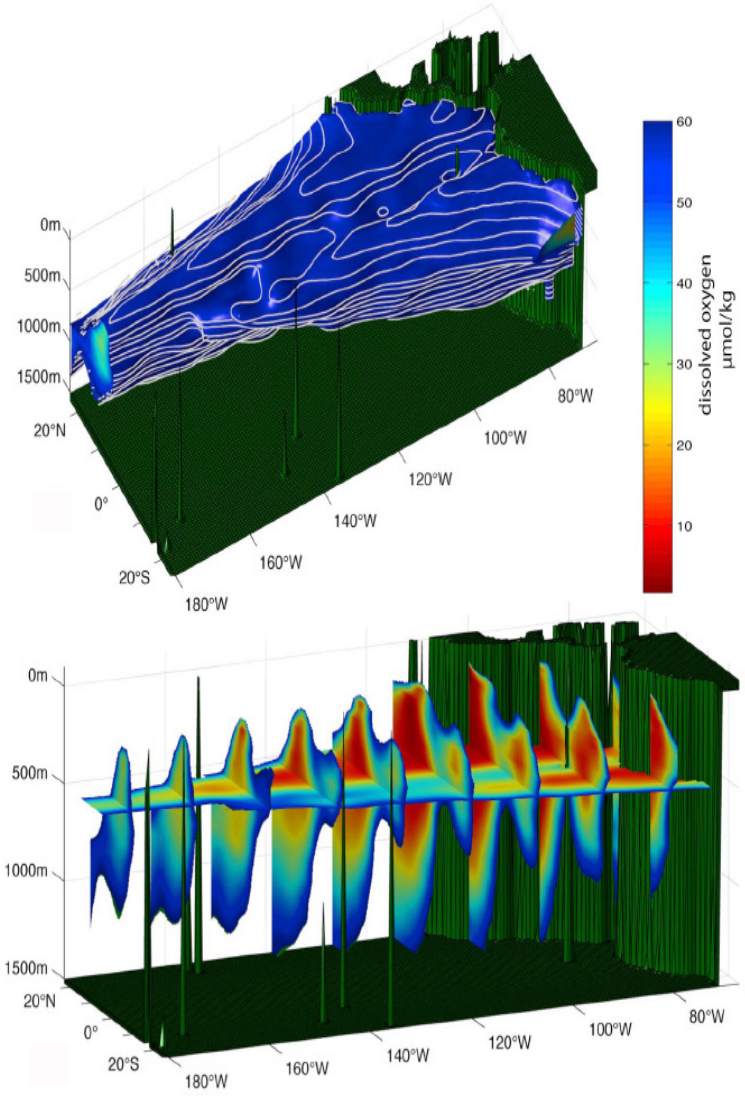

Figure 11. Three-dimensional visualizations of the eastern North and South Pacific oxygen minimum zones displaying a) the 60 µmol kg^{-1} oxygen isosurface with 50 m depth contours as white lines, and b) vertical and horizontal slices with oxygen concentrations <60 µmol kg^{-1} color shaded as indicated in the bottom color bar. Database is the WOA-2005 1° mean climatology. Source: From Stramma et al. (2010a).

The ESP OMZ extends approximately between 100 and 900 m depth (Karstensen et al., 2008) and its intensity, depth range and westward extension decrease poleward from the equator (Figure 11). It covers a total area of ~(5.7 ± 0.6) × 10^6 km^2 and its suboxic core has an average thickness of 190 ± 170 m (Paulmier and Ruiz-Pino, 2009). Inside the core, oxygen concentrations <5 μmol kg^{-1} are found between 5–12°S and centered at the isopycnal σ_θ = 26.8 kg m^{-3} (~350-450 m) (Stramma et al., 2010a). The suboxic conditions found in the core present oxygen concentrations only slightly larger than those found in the strongest OMZ in the world ocean, the eastern North Pacific OMZ (ENP OMZ) (Karstensen et al., 2008). The reason for the difference in oxygen content between the two is the absence of water mass renewal at intermediate and deep layers in the ENP (Reid, 1965).

If the ESP OMZ gets to strengthen in the future, it will reduce the habitat of many marine species and threaten the most productive pelagic fishery of all eastern boundary systems in the world ocean (Strub et al., 1998). Therefore the importance of understanding which water masses reach the ESP OMZ, what are their principal pathways and what is the major pattern of temporal variability.

1.5 Aims and outline of the thesis:

There are two main objectives in this doctoral dissertation:

a) To accomplish a thorough characterization and analysis of the water masses found in the ESP, including both a description of their spatial distribution and their interannual variability associated to the ENSO phenomenon.
b) To provide a global picture of the pathways for oxygen supply into the ESP OMZ, examining the relative roles played by the mean advection and by the mean turbulent diffusion.

The main chapters of this dissertation are structured as scientific papers, which can result in some reiteration but allows reading them as independent pieces of research. The thesis closes with a chapter dedicated to summarize the principal conclusions and briefly discuss some questions arising from our research.

Chapter 2

In this chapter we use inedit hydrographic data gathered during the Humboldt cruise (March 2009) along the continental slope off Chile to provide an in-depth description of the thermohaline and chemical characteristics (water types) of the water masses found in the ESP. To this end, we developed, implemented and applied an intermediate complexity version of the inverse modelling technique known as the Optimum Multiparameter Analysis (OMP). In addition, we discuss the distribution of the water masses and examine what these distributions tells us about their spreading pathways, with a focus on the water masses involved in the ventilation of the ESP OMZ.

Chapter 3

The ESP OMZ is influenced by the interannual (ENSO) and long-term (PDO) modes of variability found in the Pacific Ocean. In this chapter we examine changes in the water mass structure of the tropical ESP in order to assess the impact of two opposite phases of ENSO on both the biogeochemical activity and the ventilation of the ESP OMZ. For this purpose we further developed our OMP scripts in order to account for the biogeochemical cycling (respiration and denitrification) within the water masses. This substantial improvement of the OMP method enables to accomplish a more sound water mass analysis at larger scales. The hydrographic data used in this chapter were obtained from the WOCE P19 cruise (March 1993) and from the inedit (and gently provided) dataset of the German M77 cruise (February 2009). This chapter was born as part of a research stay at the Helmholtz Centre for Ocean Research (GEOMAR), in Kiel, Germany.

Chapter 4

The ESP OMZ is assumed to be only ventilated by the eastward flowing currents of the Equatorial Current System. Previous studies have focused only on the oxygen supply of equatorial origin. However, a global picture of the mean advective pathways of oxygen supply into the ESP OMZ is still missing. In this chapter we provide such a global picture and unveil the relevance of the subtropical oxygen supply to the ESP OMZ. In addition, we examine the role played by mean advection and turbulent diffusion (both epineutral and dianeutral) in the total oxygen supply to the ESP OMZ at different isoneutral layers. We also calculate the biological consumption required to close the annual-mean oxygen budget inside the ESP OMZ and compare it with independent estimates. For the purposes of this study we disregard the weak expansion trend observed (Stramma et al., 2008) and assume that the ESP OMZ is in a steady-state (this assumption is justified by its relative stability in time and space). To this end, we used the Roemmich-Gilson Argo climatology and the dissolved oxygen data from the World Ocean Atlas 2013. The fourth chapter was initiated during an international stage at the Scripps Institution of Oceanography (UCSD), in San Diego, United States.

Chapter 5

This thesis ends with a summary of the main findings, placed together in a wide regional context and recapitulating the questions open to future research endeavours. Further studies using historical data, combined with the modern Argo dataset, are needed to assess the long-term evolution and variability of the water mass structure and distribution. In addition, the analysis of the seasonality in the pathways of oxygen supply will surely help to advance our present understanding on how the ESP OMZ is maintained and how it may evolve in the future under the current scenario of global warming.

CHAPTER

2

Meridional and zonal changes in water properties along the continental slope off central and northern Chile

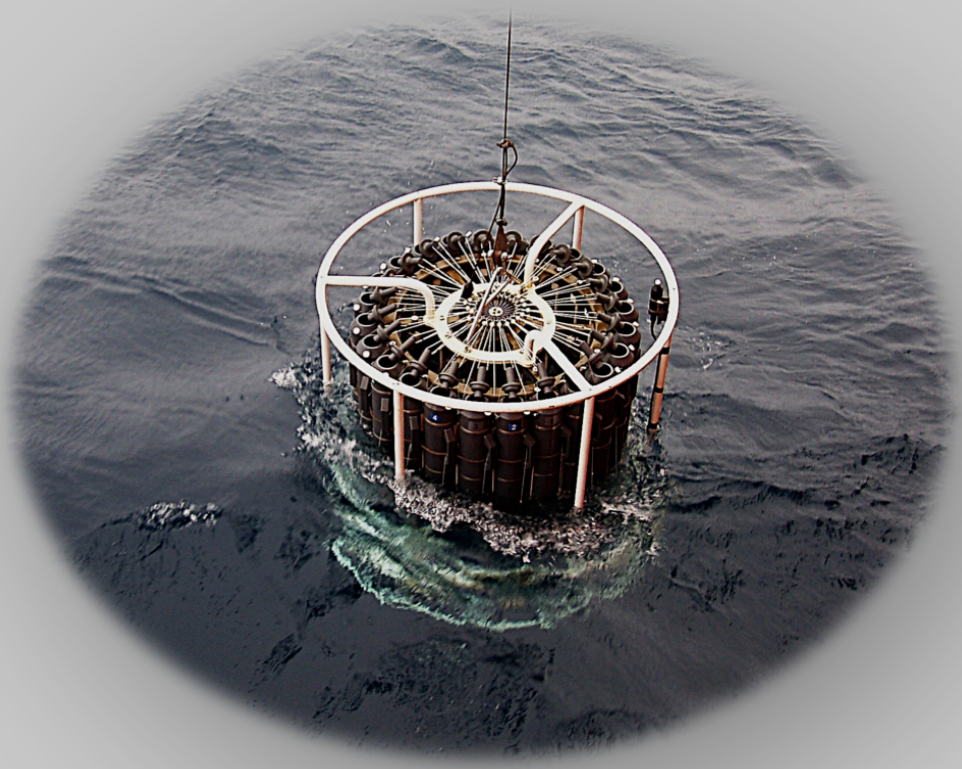

Llanillo, P. J., Pelegrí, J. L., Duarte, C. M., Emelianov, M., Gasser, M., Gourrion, J., and Rodríguez-Santana, A.: Meridional and zonal changes in water properties along the continental slope off central and northern Chile, Ciencias Marinas; Vol. 38, No. 1B: Special issue on Descriptive Oceanography with Tracers in Coastal and Deep Oceans, 307–332, 2012.

"La luna en el mar riela,
en la lona gime el viento,
y alza en blando movimiento
olas de plata y azul."
José de Espronceda

Abstract

The Humboldt-09 cruise covered a narrow meridional band along the Chilean continental slope, from 44 to 23ºS. Here we use physical and biochemical data from a long meridional section (4000 km) and three short zonal sections (100 km) to describe the distribution of the different water masses found in this region. Six water types are identified: Subantarctic Water (SAAW), Summer Subantarctic Water (SSAW), Subtropical Water (STW), Equatorial Subsurface Water (ESSW), Antarctic Intermediate Water (AAIW) and Pacific Deep Water (PDW). For the first time, a novel set of water type properties is introduced for SSAW, and nutrient and dissolved oxygen water types are also proposed for all the water masses. The Optimum Multiparameter Analysis (OMP) is used through an iterative process to obtain a sound definition of the water types that minimizes the residuals of the method. Both the classic OMP and the quasi-extended OMP analyses do rather well in reproducing the data. Finally, the spatial distribution of the different water masses is calculated with the quasi-extended OMP, which is not influenced by the respiration of the organic matter. The distribution of the different water masses is presented over the meridional and zonal transects and in property-property diagrams. A smooth meridional transition from subantarctic to tropical and equatorial water masses is observed in this area. This transition takes place in surface, central and intermediate waters over distances of the order of one thousand kilometres. The meridional transition contrasts with the abrupt zonal changes found in the cross-slope direction, of comparable magnitude but over distances of the order of one hundred kilometres. Both AAIW and SAAW (fresh and well oxygenated) partially mix with the hypoxic ESSW and, therefore, play an important role in the ventilation of the southern part of the oxygen minimum zone (OMZ).

Chapter 2

2.1 Introduction

The current system off central and northern Chile is quite complex, with the alternation of equatorward and poleward currents that bring different water masses over a zonal band of a few hundred kilometres (Figure 1). These currents have high meridional coherence, of thousands of kilometres, but are separated in the cross-shore and vertical directions by only tens of kilometres and meters respectively (Strub et al., 1998). In a sense we may talk of large horizontal cells that connect tropical with temperate regions, and the latter with subpolar regions.

In the offshore tropical and temperate regions we find a dominant equatorward current, the Peru-Chile Current (PCC) (also named the Humboldt Current, HC) (Silva et al., 2009). The PCC feeds from the South Pacific Current (SPC) (Stramma et al., 1995) also known as the West Wind Drift (WWD), a wind-driven high-latitude broad eastward current (roughly between 40 and 50ºS), and runs towards the equator far off the continental slope bringing relatively cold waters as far north as the Peru coast (Silva et al., 2009). The PCC finally feeds into the South Equatorial Current (SEC) and its cold tongue can be appreciated as far as 4ºS (Penven et al., 2005). In these tropical and temperate regions, near the slope, we also encounter a poleward current system. This poleward flow is commonly split into an undercurrent adjacent to the slope, the Poleward Undercurrent (PU), and a further offshore surface current, the Peru-Chile Counter Current (PCCC) (Strub et al., 1998), although it is likely that the latter is simply the surface and offshore manifestation of the former. Near the shelf, we find the equatorward Peru Coastal Current (PcC) which is fed by the Chile Coastal Current (CCC) located further south, both are surface currents associated with the upwelling front (Strub et al., 1998). The PcC and CCC waters remain separated from the PCC by the poleward current system (PU and PCCC), except during summer at high latitudes (between about 35 and 45ºS) where the whole region flows equatorward. In the subpolar region the single dominant poleward current, the Cape Horn Current (CHC), experiences substantial buoyancy gain due to high precipitation while being driven by poleward downwelling winds (Halpin et al., 2004).

The meridional limits of these currents change seasonally according to the high atmospheric pressure in the southern Pacific. It is likely that some of these currents may locally converge, or even feed from each other, hence forming meridional cells. For example, the near-slope poleward current system (PU and PCCC) may feed the coastal PcC, so that the latter begins further south in summer than during winter (Strub et al., 1998). These meridional motions are accompanied by normal-to-shore vertical motions also induced by the southerly winds, in what constitutes an upwelling cell much smaller in size but running over nearly four thousand kilometres (Strub et al., 1998). The vertical and horizontal cells are connected: as the wind intensifies the coastal jet gets stronger but upwelling also strengthens, with diapycnal transfer and offshore transport (from wind-driven Ekman transport and along-shore divergence) likely bypassing the meridional connections. The interplay

of these different processes actually controls the meridional and zonal extension of the main water masses in the region. The relevant issue for our study is that we expect to find substantial changes in water masses as we move over short cross-slope distances, as compared with the long along-slope distances necessary to change from subpolar to temperate and tropical waters.

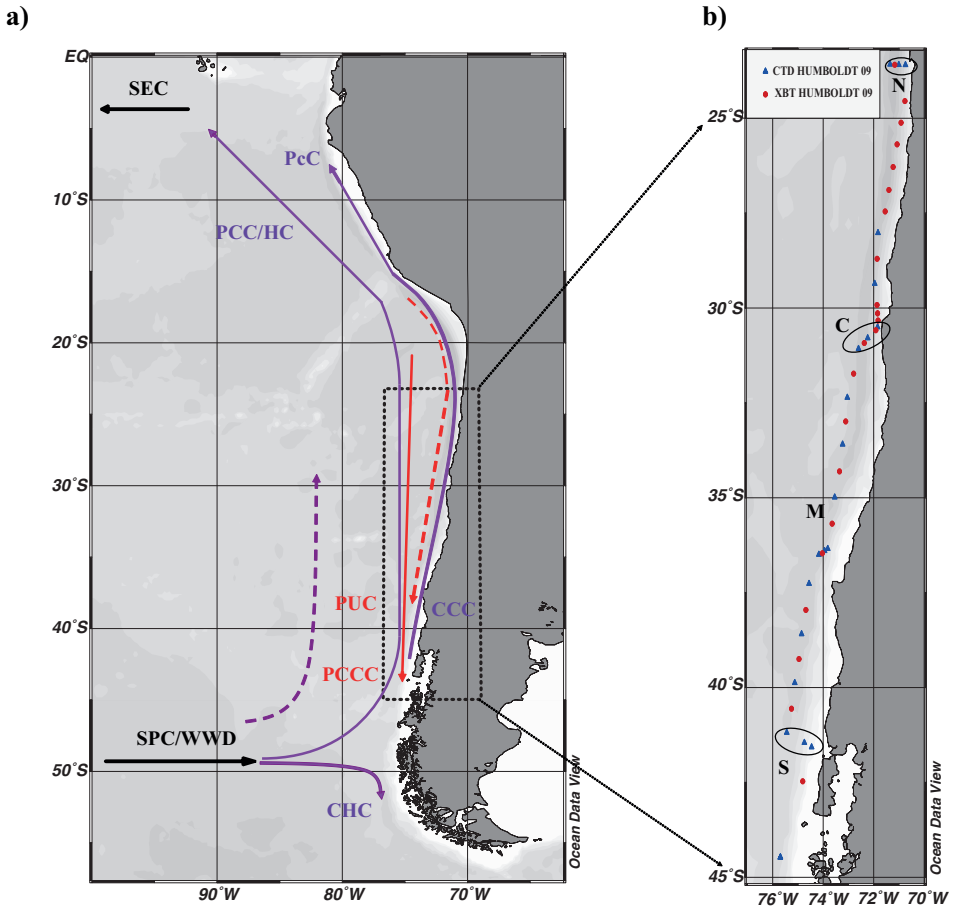

Figure 1. (a) Map of the eastern South Pacific with schematic arrows indicative of the patterns of motion for the dominant water masses. The lines sketch the dominant currents (PCC/HC: Peru-Chile or Humboldt Current, PCCC: Peru-Chile Counter Current, PUC: Poleward Undercurrent, PcC: Peru Coastal Current, CCC: Chile Coastal Current, CHC: Cape Horn Current, SEC: South Equatorial Current and SPC/WWD: South Pacific Current or West Wind Drift) with red/purple lines indicating waters of tropical/subpolar origin. The dashed lines correspond to intermediate waters. The solid and dashed lines are suggestive of the main direction of propagation of the upper and intermediate waters. **(b)** Study area with the hydrographic (blue triangles) and XBT (red circles) stations. The meridional (M) and three zonal sections (northern N, central C and southern S) are shown.

Traditionally five different water types have been identified in our study area (Silva et al., 2009). Three of these are found down to some 500 m, the Subtropical Water (STW), the Subantarctic Water (SAAW), and the Equatorial Subsurface Water (ESSW). Between 500 and down to some 1000 m we find Antarctic Intermediate Water (AAIW) and, further deep, Pacific Deep Water (PDW) is found. We have described for the first time an additional water mass off central and southern Chile which results from SAAW modified by relatively fresh water coming from intensified spring runoff

and summer melting from the fjord region between 40 and 45ºS), here we will name it Summer Subantarctic Water (SSAW).

High-quality hydrographic data of this region are sparse, taken over a few transects. To our knowledge, the major previous cruises in this area are the 1967 Scorpio cruise (Scripps Institution of Oceanography, 1969; Stommel et al., 1973), the 1969 Piquero cruise (Scripps Institution of Oceanography, 1974), the 1974 Krill Leg 4 cruise (Silva and Konow, 1975), the 1995 Sonne 102 cruise (Leth et al., 2004) and the 2000 Cimar 6 and Cook-2 cruises (Schneider et al., 2007),. Under the framework of the recently created "Laboratorio Internacional de Cambio Global" (LINC-Global), the Humboldt-09 cruise was conducted on March 2009 along the eastern South Pacific. One of the targets of this cruise was to contribute to the physical and chemical longitudinal and latitudinal characterization of water type properties in a 100-km nearshore band between 23 and 44ºS (Figure 1). These included not only salinity and potential temperature, whose water type values are reasonably well known for the area, but also inorganic nutrients and dissolved oxygen.

In section 2.2 we introduce the data set obtained along the meridional and zonal transects and carefully revise the classical and quasi-extended Optimum Multiparameter techniques (OMP) used to determine the contributions of the distinct water masses. In section 2.3 we show the distribution of physical and biochemical water properties along these transects and present the data points in several property-property diagrams. In section 2.4 the relative contributions of the different water types are calculated using the OMP analysis and the relative contributions of these water masses are plotted on the vertical transects and the property-property diagrams. We sum up with the major conclusions on the zonal and meridional interleaving of the different water masses (section 2.5).

2.2 Data set and Methodology

2.2.1 Data set

The data set was obtained during the Humboldt-09 cruise on board the Spanish R/V Hespérides. The cruise spanned more than 20º of latitude along the continental slope off Chile, from 44 to 23ºS (Figure 1). The hydrographic measurements consisted of an along-slope meridional transect (M transect), with Conductivity-Temperature-Depth (CTD) stations spaced about 100 nautical miles (nm) and Expendable Bathythermographs (XBTs) deployed at intermediate positions in between the CTD stations. Additionally, it comprised three short zonal transects with a length of some 50 nm, going from the continental platform to the deep ocean, and labelled North (N, at 23ºS), Central (C, at 31ºS) and South (S, at 42ºS). Each of these cross-slope transects had three CTD casts.

A total of 22 CTD stations were taken down to 1500 m. In these stations 12-liter water samples from a 24-bottle rosette were analysed for salinity, dissolved oxygen and inorganic nutrients. Dissolved

oxygen concentrations were calibrated with high-precision Winkler titration using a potentiometric electrode and automated endpoint detection (Mettler Toledo, DL28 titrator). Water samples were also frozen at 20ºC below zero and later analysed with a AA3 Bran-Luebbe Autoanalyzer in order to obtain nutrient concentrations of phosphate, nitrate, nitrite and silicate. In addition, a total of 23 XBTs were deployed along the cruise track. Throughout the cruise, velocity data in the upper few hundred metres of the water column were collected by the vessel's Acoustic Doppler Current Profiler (ADCP) mounted on the hull. The thermosalinograph and fluorometer continually collected data from the ship's underway system. Meteorological variables were monitored using the on board meteorological sampling system.

In this paper we use the XBT data only to get a high resolution view of the temperature fields and then use the potential temperature, salinity, dissolved oxygen and inorganic nutrient data from the CTD stations to characterize the meridional and zonal distributions of the water masses present in the region.

2.2.2 Optimum Multi-Parameter Analysis

The Optimum Multi-Parameter (OMP) method was originally developed by Tomczak (1981) and subsequently improved by Mackas et al. (1987). The OMP is an inverse modelling technique widely used to study the distribution of water masses at scales where its properties are approximately conservative (classic approach) (e.g. Tomczak and Large, 1989; Pérez et al., 2001; Tomczak and Liefrink, 2006; Silva et al, 2009). In this subsection we briefly revise the basics of the OMP technique, while in the following two subsections we have a more detailed discussion of its implementation for our study area.

The OMP method relies heavily on the definition of the water types or source water mass properties. The characteristics of a water type are defined by the region where it was formed, although this region may actually lie quite far away from the study area. Hence, the water type properties used by the OMP method have to compromise between maintaining the most distinctive original source water type characteristics and still being indicative of this water mass after the transformations that it has suffered while reaching the study area. Two different strategies may be used: to set local water types for the subset of variables with the least conservative behaviour or to use non-local water types for all variables. The local approach is the basis of the classic OMP method and assumes that all variables behave conservatively in a small enough region. The second approach, with water types defined in the formation region, takes into account the biogeochemical transformations within the water masses as they travel from their source regions.

There are two techniques to consider the biogeochemical changes of the non-conservative properties. The first one adds a new unknown to the equations for the non-conservative variables.

This unknown accounts for the biogeochemical changes of all non-conservative variables, under the assumption that they change jointly in accordance to the Redfield ratios of degradation of organic matter. This technique is known as the extended OMP analysis (Karstensen and Tomczack, 1998; Poole and Tomczack, 1999). Its main advantage is that allows quantifying biogeochemical changes and the estimation of water-mass pseudo-ages, if the oxygen utilization rate (OUR) is well known. The difficulty lies on the fact that the OUR is not constant throughout the ocean, changing with time and location; therefore, estimates of the OUR are subject to substantial errors unless other data, such as chlorofluorocarbon (CFC) data, is available (Karstensen and Tomczack, 1998). The second technique is a refinement of the classic OMP method where the non-conservative variables are converted into conservative variables (Broecker, 1974; Anderson, 1995; Fraga et al., 1998; Perez et al., 2001). Because of the lack of accurate OUR values in our study area, we will use this second technique and leave the use of the extended OMP analysis to future works. Hereafter, we will refer to this technique as the quasi-extended OMP analysis, its implementation is further discussed in Section 2.2.4.

The OMP method assumes that each parameter sampled in each data point may be expressed as a linear combination of original water types which are still present in the area (Tomczak and Large, 1989). An underlying assumption is that mixing operates equally for all parameters and has no preferential direction, i.e. isotropic turbulent mixing is assumed (Karstensen and Tomczak, 1999). Consequently, a linear system of mixing equations with the contributions of the different water types, or mixing coefficients, can be set up for each single data point. In this system the water-type contributions constitute a set of non-negative mixing coefficients that represent the best linear mixing combination to reproduce the measured value.

The best solution is found using a non-negative least squares method to solve the system of equations (Mackas et al., 1987). In order to solve each system of mixing equations in a physically sensible way there are two principal conditions: (1) the number of water types (n) should not exceed in more than one the number of variables sampled at every single point (n-1), and (2) any data point should be within a region (in any property-property space) encompassed by the water types, i.e. all points are within the spreading path of the source water masses. The mass conservation equation is added to each of these systems, which may sometimes be over-determined.

Once we have defined the water types of each water mass, we normalize and weight the data and the water types (for each variable or parameter). Each variable is weighted according to the accuracy of its measure (Table 1). The normalization process is accomplished by subtracting the mean to the original (measured) value and dividing by its standard deviation. In this manner all variables have maximum variations of the same order so changes of the different variables are directly comparable (Tomczak and Large, 1989). We place the largest weight on the mass conservation equation, because

this condition must be met, followed by the potential temperature and salinity equations as these variables are not affected by biogeochemical processes. Once the data is normalized and weighted, an equation is defined for each variable C:

$$\sum_{i=1}^{n} C_i X_i = C + R_C \qquad (1)$$

where X_i is the relative contribution (mixing coefficient) of the i^{th} water mass (subindex *i*) with water type C_i, so that the combination of all *n* water masses leads to the observed C value. The combination has a residual, *R* (the subindices identify the variable corresponding to each residual), which is to be minimized.

A system of mixing equations is constructed and solved by using the non-negative least squares method for each data point. The number of equations (*n*) is equal to the number of variables plus one, the last necessary equation being mass conservation, i.e. the sum of all mixing coefficients adds up to one. The system of equations may be written in matrix form as

$$\vec{\vec{A}} \cdot \vec{x} = \vec{C} + \vec{R}, \qquad (2)$$

where $\vec{\vec{A}}$ is a $n \times n$ matrix containing the values of the *n-1* variables plus water mass conservation (which takes a value of one) for all *n* water masses, $\vec{x} = (X_1, ...X_n)$ is the vector containing the mixing coefficients for all *n* water masses, $\vec{C} = (C_1, ...C_{n-1}, C_n = 1)$ is the vector containing the observations and $\vec{R} = (R_1, ...R_{n-1}, R_n = R_{mass})$ is the vector of the residuals for each variable (including mass).

Finally, we employ an iterative process in order to minimize the residuals and, consequently, to improve the final solutions. The method is used to recalculate the water types for all variables except potential temperature and salinity, so that we get values that are slightly different from the original ones. With this new set of water types the system of equations is solved once again for each data point and we obtain a new set of mixing coefficients and associated residuals. This iterative process is executed until the associated residuals are minimized or, in other words, when no noticeable improvement is obtained in the next run of the loop. Once this stage is reached we may still further adjust the end-member values of some variables with the objective that, when viewed

in the property-property domains, all data points are approximately encompassed by the water type definitions (condition 2 of the OMP method).

2.2.3 Implementation of the classic OMP analysis

The classic approach assumes that the biogeochemical changes of oxygen and nutrients within a single water-mass are negligible at a regional scale, i.e. all variables used in the analysis are considered to be conservative (Tomczak, 1981). Therefore, a key aspect is to properly identify the thermohaline and biochemical characteristics of the water types (end-members) which may be present in the study area.

Two different water-type definitions are investigated (Table 1). For each of these we have carried out two different runs, without and with nitrate, as described further below. The first definition uses the values obtained from the Gouretski and Koltermann (2004) climatology. However, this option showed poor skill to explain the variance of the data set, particularly for salinity and the biochemical (oxygen, phosphate and nitrate) variables (Table 2). This is true independent on whether we include

Table 1. Water types and their characteristic property concentrations.

Water mass	θ (ºC)	Salinity	Oxygen (mL L^{-1})[a]	Phosphate (µmol kg^{-1})[a]	Silicate (µmol kg^{-1})[a]	Nitrate (µmol kg^{-1})[a]	NO (µmol kg^{-1})[b]	PO (µmol kg^{-1})[b]	Mass conservation
SSAW	15.0	33.0	5.7	0.66	0.0	2.20	272.63	350.94	–
STW	20.0	35.2	4.88	0.28	0.0	0.07	190.62	270.98	–
SAAW	11.5	33.8	5.83	0.84	0.0	14.88	358.40	417.59	–
ESSW	12.5	34.9	0.1	3.02	24.39	17.12	245.98	452.87	–
AAIW	3.0	34.0	4.7	1.95	9.76	36.70	501.54	507.66	–
PDW	1.75	34.68	1.7	2.92	108.21	39.15	517.42	574.90	–
Weights	24	12	2	2	12	2	6	6	100

[a] These water types are obtained from local values as explained in the text.

[b] From these preformed values of NO and PO it is possible to estimate preformed values of nitrate and phosphate assuming saturated values of oxygen in the formation region as explained in Pérez *et al.* (1993).

or not nitrate as an additional variable. Therefore this first option was rejected. The second option, i.e. to use local water types as deduced through the analysis of our own data set, was found to explain much better the data variance (Table 2).

The characteristic values of the variables (potential temperature θ, salinity S, dissolved oxygen O, phosphate P, nitrate N, and silicate Si) for each of the six different water types (STW, SAAW, ESSW, AAIW, PDW and SSAW) were estimated as follows. The potential temperature and salinity water types were taken from Silva et al. (2009). We further defined the SSAW thermohaline values, as a high-latitude surface end-member, based in the surface data values south of 40ºS found in the Humboldt-09 cruise (Table 1). After defining the potential temperature and salinity water types we may obtain the end-members for each of the remaining variables (oxygen, phosphate, nitrate and

silicate; not available in the literature) by calculating its mean value from all data points that are located close enough to the potential temperature and salinity values of the water type, specifically for this calculation we respectively define windows of ± 0.2ºC and ± 0.05 around the potential temperature and salinity values of each water type. These are used as the initial end-members for oxygen, phosphate, nitrate and silicate. The iterative procedure is then carried out, as described in the last section. Finally, the phosphate, silicate and oxygen water types for the AAIW and ESSW are reassessed by plotting the data points in the phosphate-oxygen and silicate-oxygen spaces and

Table 2. Comparison of the performance of the different optimum multiparameter (OMP) models evaluated. For all models, the explained variance (R^2) and the standard deviation of the residuals (σ) are shown for each variable (θ = potential temperature). The explained variance and the standard deviation are related as $R^2 = \sigma_m^2/\sigma^2$ where $\sigma_m^2 = \sum_{j\ data} (\hat{C}_j - \overline{C})^2$ and $\sigma^2 = \sum_{j\ data} (C_j - \overline{C})^2$. The summation is over all

Model		θ	Salinity	Oxygen	Silicate	Phosphate	PO	Nitrate	NO
OMP classic	R^2	0.9944	0.7225	0.8287	0.9949	0.7800	–	0.1681	–
Water types from climatology	σ	0.3257	0.1445	24.2613	0.9549	0.2359	–	8.3754	–
OMP classic	R^2	0.9943	0.7280	0.8108	0.9968	0.9182	–	0.5839	–
Water types from local values (with nitrate)	σ	0.3274	0.1451	21.8543	0.8116	0.1943	–	7.7867	–
OMP classic	R^2	0.9944	0.7282	0.8119	0.9975	0.9166	–	–	–
Water types from local values (no nitrate)	σ	0.3279	0.1452	21.8144	0.8070	0.1945	–	–	–
OMP quasi-extended	R^2	0.9910	0.7283	–	0.9974	–	0.7941	–	0.7465
Water types from local values (with NO + PO)	σ	0.4133	0.1450	–	0.8846	–	32.8008	–	50.0614

determining which slight changes in the water types may ensure that all data points are embraced by the water type values (condition 2 of the OMP method) while the residuals remain equally small or even decrease. The final values are given in Table 1.

Once the end-members are properly characterized, the system of equations (2) may be solved using either five (θ, S, O, P, and Si) or six variables (now including nitrate N, therefore setting an overdetermined system of equations for each point). For those runs without nitrate, for example, we have five variables so we may determine the contributions from up to six water masses, i.e. in the system of equations (2) $\vec{\vec{A}}$ is a 6×6 matrix, $\vec{x} = (X_1, X_2, X_3, X_4, X_5, X_6)$ is the vector containing the mixing coefficients for all six water masses, $\vec{C}$ = (θ, *S, O, P, Si,* 1) is the vector containing the observations, and $\vec{R}$ = (R_θ, R_S, R_O, R_P, R_{Si}, R_{mass}) is the vector of the residuals for each variable (including mass). The water masses to be considered are those discussed in the Introduction: SAW, STW, SAAW, ESSW, AAIW, and PDW (Table 1).

The inclusion of nitrate does not serve to improve the results. With this additional variable the variance explained by the model (R^2) decreases, and the model does very poorly at reproducing the variance of the nitrate data (Table 2). This is probably due to the non-conservative behaviour of

this variable and the importance of the denitrification process which takes place at several depths with hypoxic conditions within our study area (Silva el al., 2009). Therefore, we discarded the use of nitrate in order to optimize the classic OMP analysis.

After this process we finally managed to minimize the residuals markedly, with minimum residuals corresponding to mass conservation (less than 10^{-3}) and maximum residuals for oxygen (~0.3 ml ml l^{-1}) and phosphate (~0.2 μmol kg^{-1}). This fact indicates that these variables do not actually behave conservatively at the scale of our study area as we had assumed. Therefore, their concentrations must be conditioned by the remineralization of organic matter. However, the use of local values for the water types (under the assumption that all variables will behave conservatively in a regional scale), the low weight assigned to the non-conservative parameters and the minimization of the residuals by means of an iterative process, have allowed us to obtain an optimized set of mixing coefficients. The final model explains most of the variance of our data set (99.4% of potential temperature data, 72.8% of salinity data, 81.2% of oxygen data, 99.8% of silicate data and 91.7% of phosphate data) (Table 2). This is quite a remarkable performance, simply based on the assumption that our study area is local enough to lessen the importance of biogeochemical cycles.

2.2.4 Implementation of the quasi-extended OMP analysis

For the quasi-extended approach we define conservative preformed parameters for nitrogen and phosphorous as $NO = 9.33\ NO_3 + O_2$ (Anderson, 1995; Fraga et al., 1998; Perez et al., 2001) and $PO = 135\ PO_4 + O_2$ (Broecker, 1974). The formulation is as in the system of equations (2) but now with the two previously defined additional variables. The procedure includes calculating the *NO* and *PO* values for each data point with the help of the two above equations. The water types for these two near-conservative variables may be determined using a procedure equivalent to that used for the biochemical variables (i.e. calculating the mean of all available data points within a window around the θ and *S* water-type values). This is equivalent to using the calculated mixing coefficients (X_i) in order to solve the equations $NO = \sum_{i=1}^{6} X_i NO_i$ and $PO = \sum_{i=1}^{6} X_i PO_i$ for the (NO_i, PO_i) values corresponding to each water type.

Once we have obtained the water types we can recalculate the mixing coefficients of each data point solving the system of equations set for each data point with the following set of approximately conservative variables: θ, *S*, *NO*, *PO* and *Si* (Table 1). We have assumed *Si* behaves conservatively in our study area because the OMP classic model explained 99.8% of the *Si* variance. From this point on the methodology to follow is the same as in the case of the OMP classic but with the preformed variables replacing nitrate, phosphate and oxygen. Therefore, both the data and the water types are normalized and weighted (Table 1) and the system of equations is solved for each data point by the non-negative least squares method.

The mixing model obtained explains 99.1% of the θ variance, 72.8% for *S*, 99.7% for *Si*, 79.4% for *PO* and 74.6% for *NO*. The standard deviation of *NO* residuals (50.06 μmol kg^{-1}) is half that expected from the combination of the standard deviations of the oxygen and nitrate residuals ($9.33\sigma_N + \sigma_O = 94.5$ μmol kg^{-1}). In addition, the standard deviation of *PO* residuals (32.8 μmol kg^{-1}) is also smaller than the one expected from the combination of the standard deviations of oxygen and phosphate residuals ($135\sigma_P + \sigma_O = 48.1$ μmol kg^{-1}) (Table 2).

The quasi-extended OMP analysis allows to indirectly overcome the problem due to the biogeochemical variability (by using preformed nutrients) and the difficulty to estimate an accurate value for the OUR in the study area. In addition, it allows including the nitrate in the analysis in the form of *NO*. Therefore, this method was selected for this work and the set of mixing coefficients obtained is used in Section 2.4 to depict the participation of the different water types during the Humboldt-09 cruise, in the water column along the transects and in the different property-property domains.

2.3 Results

2.3.1 Vertical distribution of properties

In this section we firstly focus on the distribution of properties on the along-slope (M) and cross-slope (N, C and S) transects. Figures 2 through 4 show potential temperature, salinity, phosphate, dissolved oxygen, nitrate and silicate distributions along these sections. Let us first consider the surface and subsurface layers (top 150 m). In these layers both potential temperature and salinity progressively increase towards tropical latitudes, from 12.5 to 17.5ºC and from 33.5 to 35 respectively (Figure 2), reflecting the transition from subpolar to subtropical and equatorial waters. Subpolar surface waters flow equatorward and enter the southern part of our study area, carrying the influence of the sub-polar low pressure systems. This water mass comes from a region were stormy conditions reduce the amount of solar radiation reaching the sea surface and high rates of precipitation drastically reduce the salinity of the surface layers (Silva et al., 2009). On the other hand, the Subtropical Pacific Anticyclone favours high rates of evaporation and solar radiation over the northern (tropical) part of our study area, therefore, increasing the salinity and potential temperature of the surface layers, giving birth to STW. The warm (~20ºC) and salty (~35.2) subtropical waters contrast with the much fresher (~33.8) and cooler (~11.5ºC) subpolar waters (Figure 2).

The above description is consistent with the dominant advective patterns for the near-surface waters in the central region of Chile: SAAW is brought equatorward by the PCC and encounters STW, which is advected poleward from tropical latitudes by the PCCC (Strub, 1998). SAAW is believed to subduct below STW near 35ºS, originating a shallow salinity minimum (Leth et al., 2004). In the southern end of the study area we also find surface waters with remarkably low values of salinity

(~33) and high oxygen content (~5.7 ml l^{-1}) (Figures 2 and 3). This fresh water mass is SSAW, or subantarctic waters modified through high spring precipitation and high fresh water discharge at the fjords of southern Chile probably due to summer glacier melting.

In the potential temperature-salinity M section (Figure 2) we may also appreciate a subsurface high salinity core in the north part of the section that appears to stretch south with the PU and which is progressively eroded with distance. This high salinity core occupies the top 500 m of the water column along section N. However, this core appears constrained to the near-slope region of section C and is missing at section S (Figure 2). This high salinity core presents extremely low values of dissolved oxygen (< 0.5 ml l^{-1}) and high concentrations of nutrients like phosphate (> 2.5 µmol kg^{-1}) or nitrate (> 40 µmol kg^{-1}) (Figures 3 and 4). It is remarkable how the oxygen minimum zone (OMZ) perfectly fits the core of high salinity. The high nutrient content is due to the remineralization of organic matter, which reduces the oxygen concentration in the water. The water mass characterized

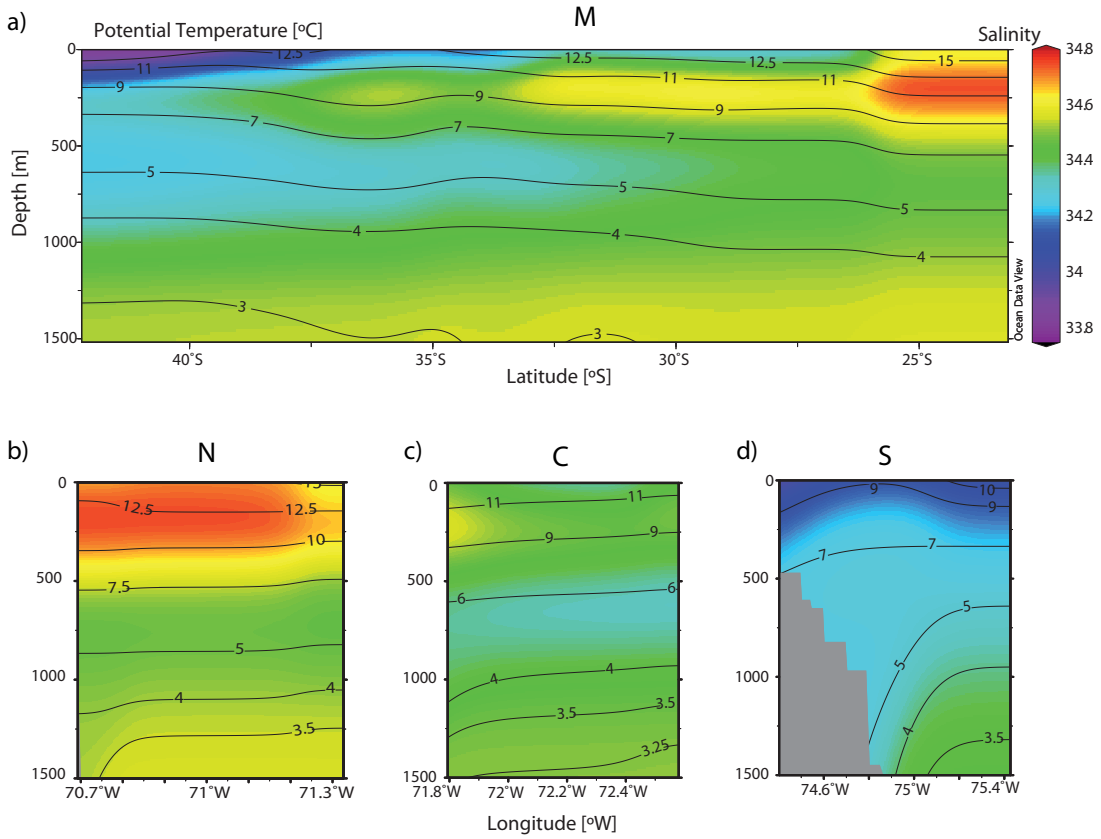

Figure 2. Distributions of potential temperature (black solid contour lines) and salinity (coloured) along the **(a)** meridional (M), **(b)** northern (N) (23.6ºS), **(c)** central (C) (30.8ºS) and **(d)** southern (S) (41.6ºS) sections; in the zonal sections the longitude axis increases in the offshore direction.

by these features is likely to be ESSW, centered at 200-250 m depth and flowing poleward along its density level while progressively mixing and losing its identity. ESSW is no longer recognizable in transect S at 41.6ºS (Figures 2, 3 and 4).

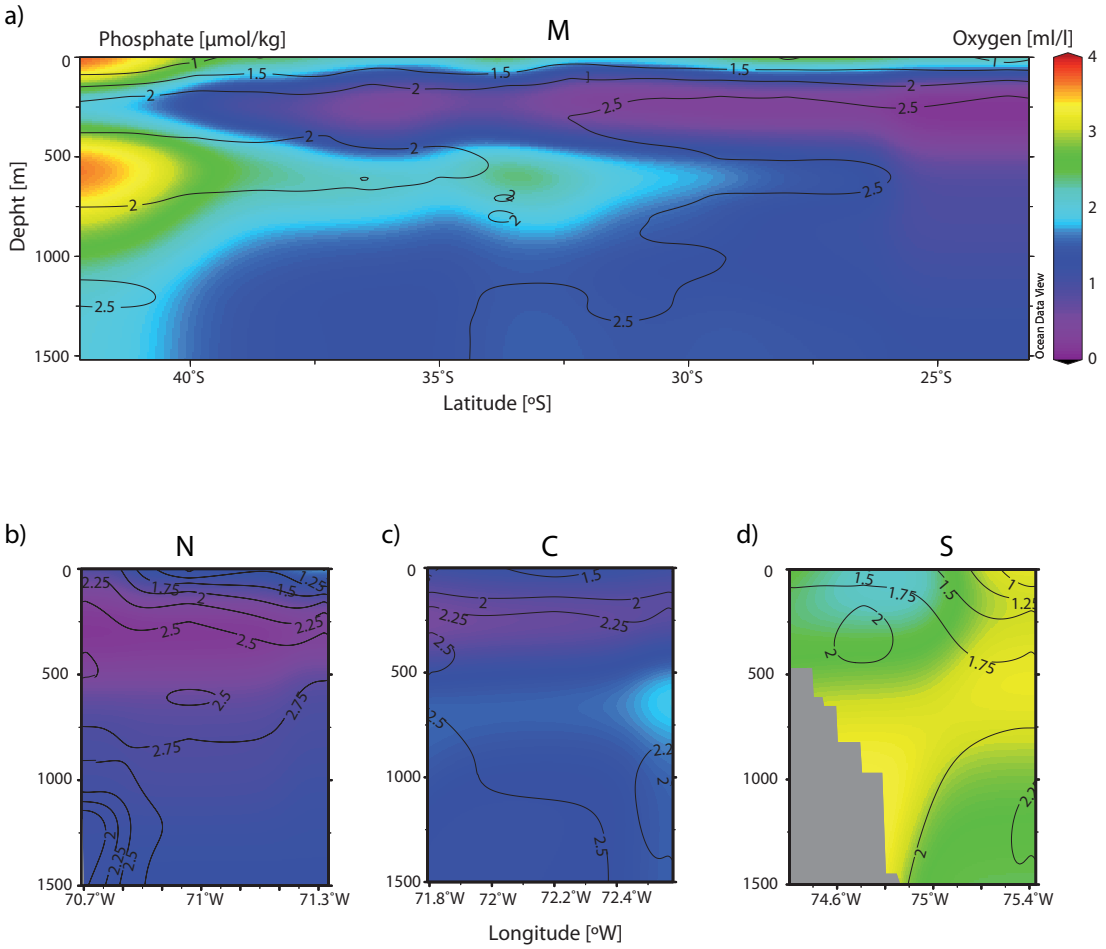

Figure 3. Distribution of phosphate (black solid contour lines) and oxygen (coloured) along the **(a)** meridional (M), **(b)** northern (N) (23.6ºS), **(c)** central (C) (30.8ºS) and **(d)** southern (S) (41.6ºS) sections; in the zonal sections the longitude axis increases in the offshore direction.

At intermediate depths (400-1200 m) and along the M transect we observe a tongue characterized by low salinity (~34.25) and potential temperature (~3ºC) values, that seems to spread northward from 44ºS. This tongue advects AAIW, a quite homogeneous water mass formed by winter convection north of the Polar Front (Hartin et al., 2011), which has been reported to fully cross the equator before completely losing its identity (Strub et al., 1998). AAIW has a relative maximum of dissolved oxygen (3-4.7 ml l^{-1}) and a relative minimum of nutrients ($P < 2$ µmol kg^{-1}, $N < 30$ µmol kg^{-1} and $Si < 50$ µmol kg^{-1}) (Figures 3 and 4).

Below AAIW, at depths larger than 1200 m, we find a more homogeneous water mass, the PDW. We sampled this water mass from 1200 m to 1500 m depth, the maximum cruise sampling depth. PDW is supposed to fill the remaining water column down to the sea bottom (Leth et al., 2004). This water mass is saltier (~34.68) and slightly colder (~1.75-3ºC) than the overlying intermediate waters. It is also characterized by low dissolved oxygen (~1.7 ml l^{-1}) and high nutrient concentration

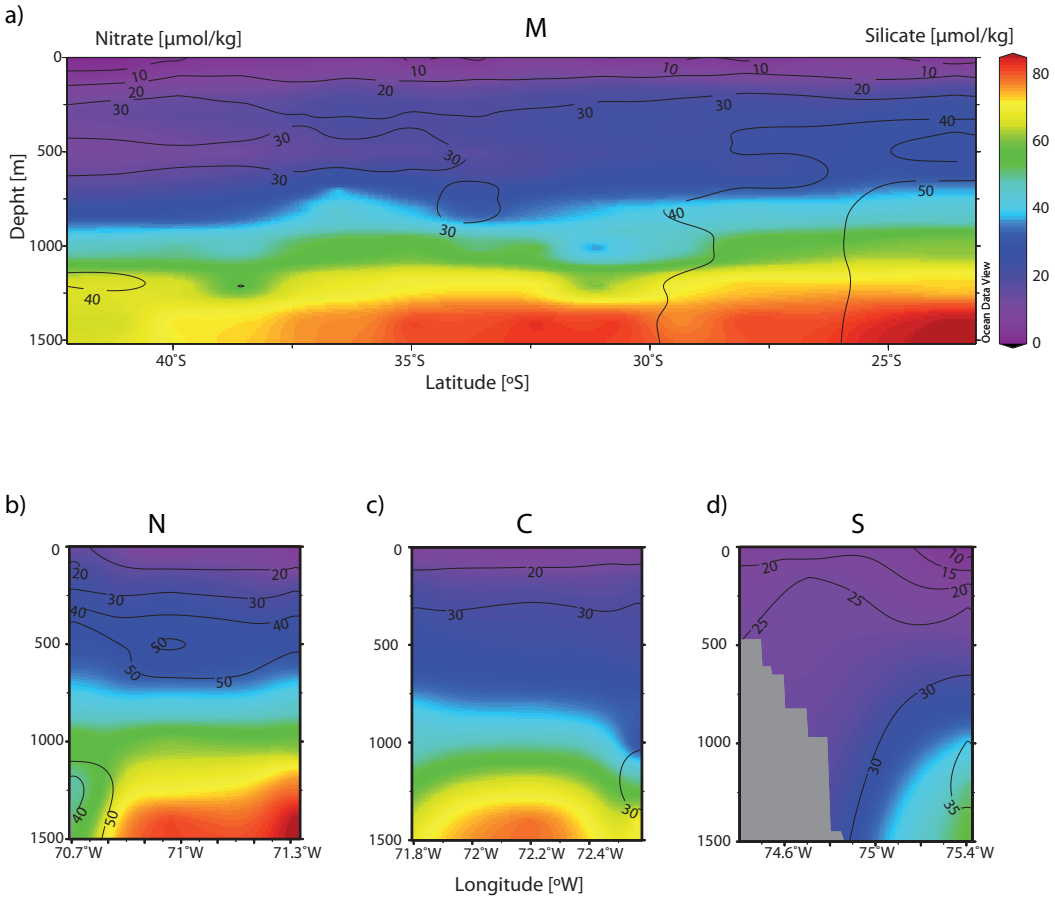

Figure 4. Distribution of nitrate (black solid contour lines) and silicate (coloured) along the **(a)** meridional (M), **(b)** northern (N) (23.6ºS), **(c)** central (C) (30.8ºS) and **(d)** southern (S) (41.6ºS) sections; in the zonal sections the longitude axis increases in the offshore direction.

($P > 2.5$ µmol kg^{-1}, $N > 40$ µmol kg^{-1}), being remarkably abundant in silicate (> 80 µmol kg^{-1}) (Figures 2, 3 and 4). For our region the PDW has been reported to move poleward (Shaffer et al., 2004) at velocities always less than 0.5 m s^{-1} (Leth et al., 2004).

2.3.2 Property-property diagrams

It is useful to examine how all data points are distributed in several property-property diagrams (Figure 5). In the potential temperature-salinity diagram (Figure 5a), we may distinguish the presence of the six water masses at different density levels. Three surface water masses (STW, SSAW and SAAW) appear within layers of potential density (σ_θ) less than 26 kg m^{-3}. The STW presents potential temperature and salinity values higher than SSAW and SAAW and is located in the northern part of our study area. In addition, SSAW is fresher and warmer than SAAW, both water masses are predominant in the southern part of our study area.

At around σ_θ = 26.25 kg m^{-3} we find ESSW, saltier and slightly colder than SSAW, mainly located at the northern part of the area analysed. Further deep (σ_θ= 27.2 kg m^{-3}) and in the southern

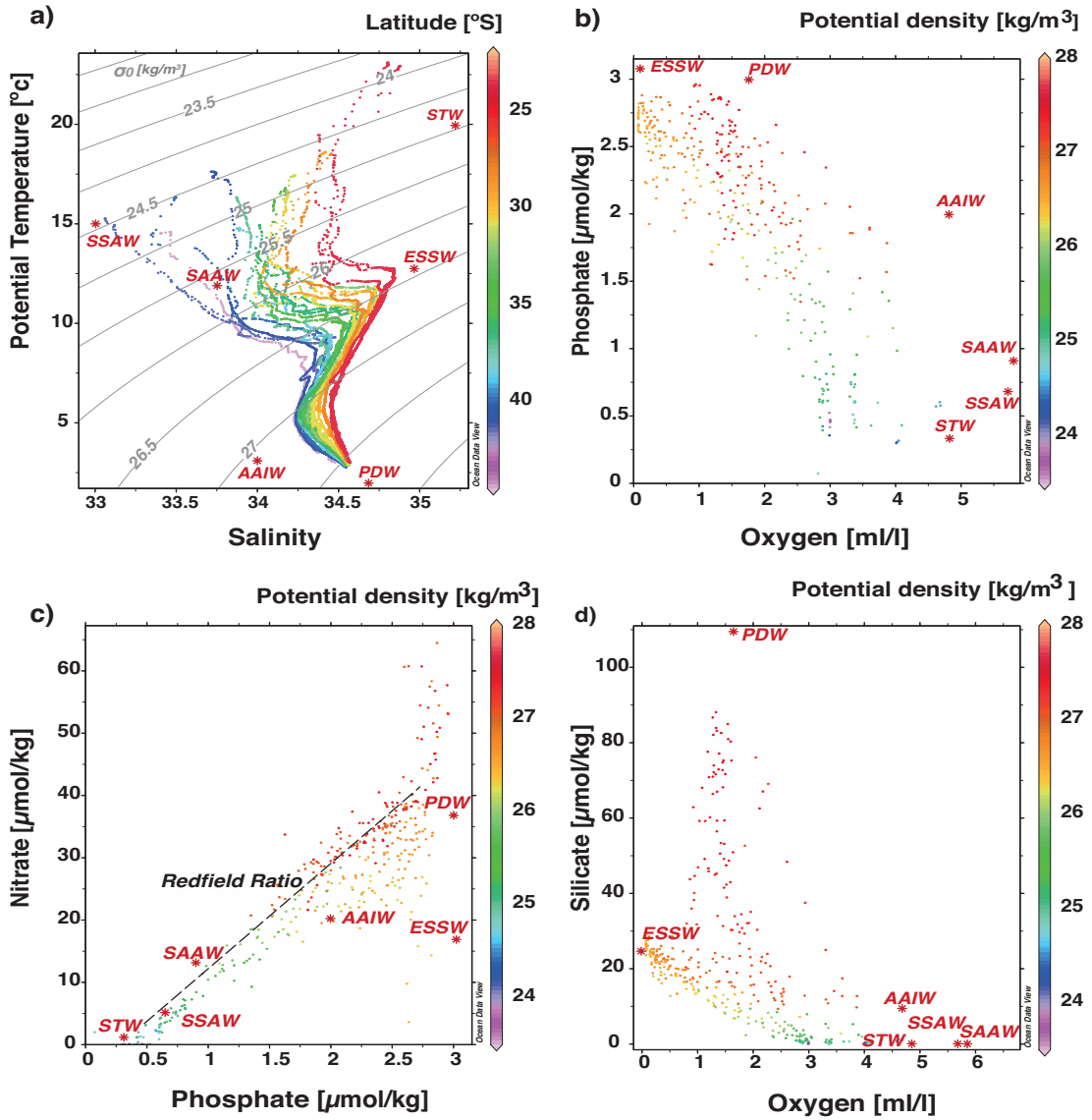

Figure 5. Water types corresponding to each water mass (red stars) from Table 1 are identified in all panels. **(a)** Potential temperature-salinity diagram with isopycnals of potential density (σ_θ) shown as grey contour lines and latitude colour-coded; **(b)** phosphate-oxygen diagram; **(c)** nitrate-phosphate diagram with the Redfield ratio shown by a dashed line; and **(d)** silicate-oxygen diagram. Potential density is colour coded in **(b)**, **(c)** and **(d).**

part of this region we find the AAIW, colder and fresher than ESSW. Finally, at greater depths (σ_θ> 27.4 kg m^{-3}) we find PDW, characterized by the lowest potential temperatures found in our study area and salinity values above those of AAIW (Figure 5a and Table 1).

In Figure 5b we may distinguish some characteristic properties of the six water masses with participation in our study area. The two subantarctic surface water masses present relatively high values of dissolved oxygen, in contrast with the hypoxia found in ESSW. AAIW also has relatively high oxygen concentrations, indicative of the proximity of its formation region north of the Antarctic Polar Front (APF) (Hartin et al., 2011). With regards to the phosphate content, we find that deep waters have higher content than the surface ones, with STW being less rich in phosphate than SSAW and SAAW. The ESSW and PDW present the highest phosphate concentration among the six water

masses found in the area (Figures 5b,c). Finally, we may observe that PDW presents the largest silicate concentrations, with values at least five times greater than within other water masses (Figure 5d).

In Figure 5c we may appreciate the Redfield ratio among nitrate and phosphate (16:1), as shown by the straight line formed by the data points. The outliers are explained by the hypoxic conditions mainly found within the ESSW layers (located below and to the right of the straight line representing the Redfield ratio and with $\sigma_\theta = 26.25$ kg m^{-3}) and in some PDW points ($\sigma_\theta > 27.4$ kg m^{-3}). This is because the Redfield ratio (*N*:*P*) is defined for the degradation of organic matter in oxygenated waters and, consequently, it is not valid in hypoxic environments where denitrification takes place. In quasi-anoxic conditions there is not enough dissolved oxygen in the water to maintain the oxidation of the organic matter. In this situation the degradation of the organic matter is maintained by nitrate, which plays the role of the dissolved oxygen as electron acceptor and is finally reduced to elemental nitrogen in a few steps (Thomas, 1966; Anderson et al., 1982; Codispoti and Christensen, 1985). In the first of these steps nitrate is reduced to nitrite, a situation that generates local nitrate minimum and nitrite maximum values (Wooster et al., 1965; Zuta and Guillen, 1970; Diaz, 1984; Codispoti and Christensen, 1985). This nitrate deficit disrupts the molar ratio *N*:*P* presenting a high deviation from the 16:1 ratio's slope found when the organic matter is remineralized in aerobic conditions (Silva et al., 2009).

2.4 Discussion

2. 4. 1 Property-property diagrams per water type

The OMP classic method, with water types for oxygen and nutrients estimated using the cruise data (discarding nitrate for the analysis) and the quasi-extended OMP method, again with the water types for the non-conservative variables determined from our own data set, performed equally well at explaining the data variance and presented similar standard deviations (Table 2). It is fair to recognize that both methods showed less skill at reproducing the salinity data (73% in both cases). The quasi-extended version can only reproduce 75 and 70% of the *PO* and *NO* variables, apparently because of the denitrification process taking place in the study area. Nevertheless, the plots obtained with these methods are very similar. Therefore, and because the quasi-extended method has the advantage of avoiding the problem due to the respiration of the organic matter, we have used it to calculate the participation of the different water masses to each of the data points gathered during the Humboldt-09 cruise.

Through the OMP analysis we have defined the water types of the six water masses that are present in the study area. Their characteristic water types may be appreciated in Figures 6, 7 and 8 where we have plotted our data set in several property-property spaces. In the potential temperature

versus salinity diagrams (Figure 6) we may appreciate the gradation of characteristics as a function of water depth, with STW, SAAW and SSAW occupying the near surface layers, ESSW and AAIW the intermediate layers and PDW the deep layers. However, there is also a remarkable gradation in latitude, with STW (ESSW) being very salty and warm as compared with SSAW/SAAW (AAIW). In the phosphate versus oxygen diagram (Figure 7) the most striking difference appears at subsurface

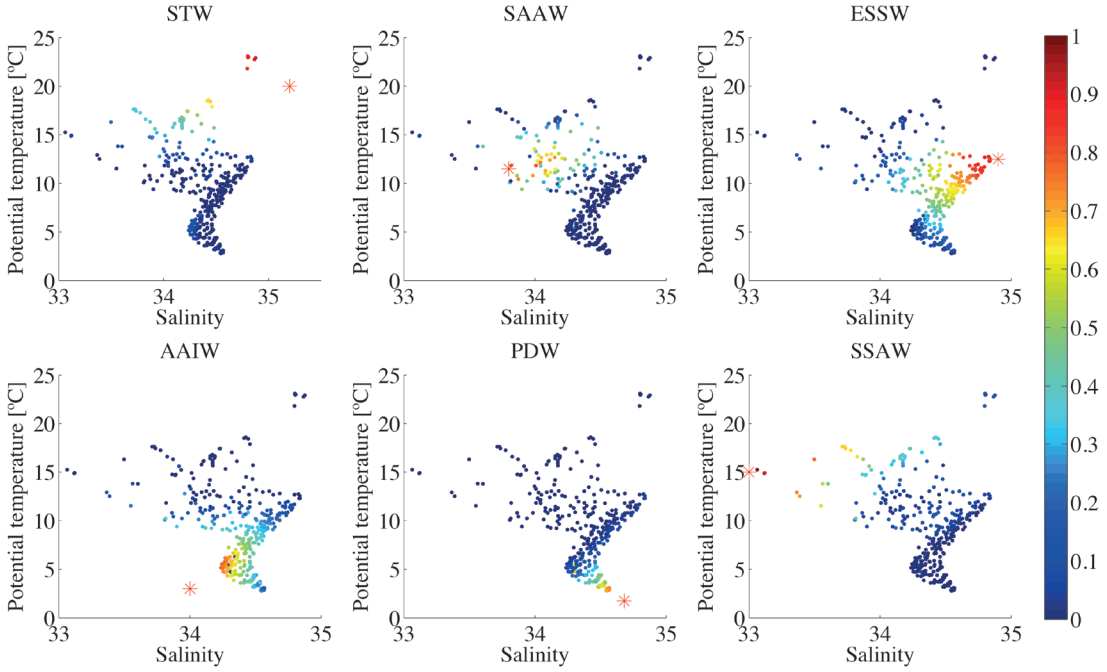

Figure 6. Potential temperature-salinity diagrams showing the relative contribution of each water mass (colour-coded). Top panels: Subtropical Water (STW), Subantarctic Water (SAAW) and Equatorial Subsurface Water (ESSW); bottom panels: Antarctic Intermediate Water (AAIW), Pacific Deep Water (PDW) and Summer Subantarctic Water (SSAW). The water types corresponding to each water mass are shown as a red star.

layers, with ESSW having much less oxygen and much more phosphate than the AAIW. In the silicate versus oxygen diagram (Figure 8) all waters appear very poor in silicate except for the PDW and, to a lesser degree, the ESSW.

The results confirm that the points located near a red asterisk (representing a water mass defined by its characteristic water types) have a substantially high participation of the corresponding water mass. This gives confidence on the high skill of the OMP technique to properly identify the contributions of the different water masses to any data point.

2.4.2 Vertical distributions per water type

The OMP quasi-extended analysis provides the contributions of the different water masses to each data point. Given this information we may plot the contributions of each water mass along the meridional and zonal Humboldt-09 transects. Figures 9 and 10 provide useful information about what is the spreading path of the water masses and how much mixing they undergo during their

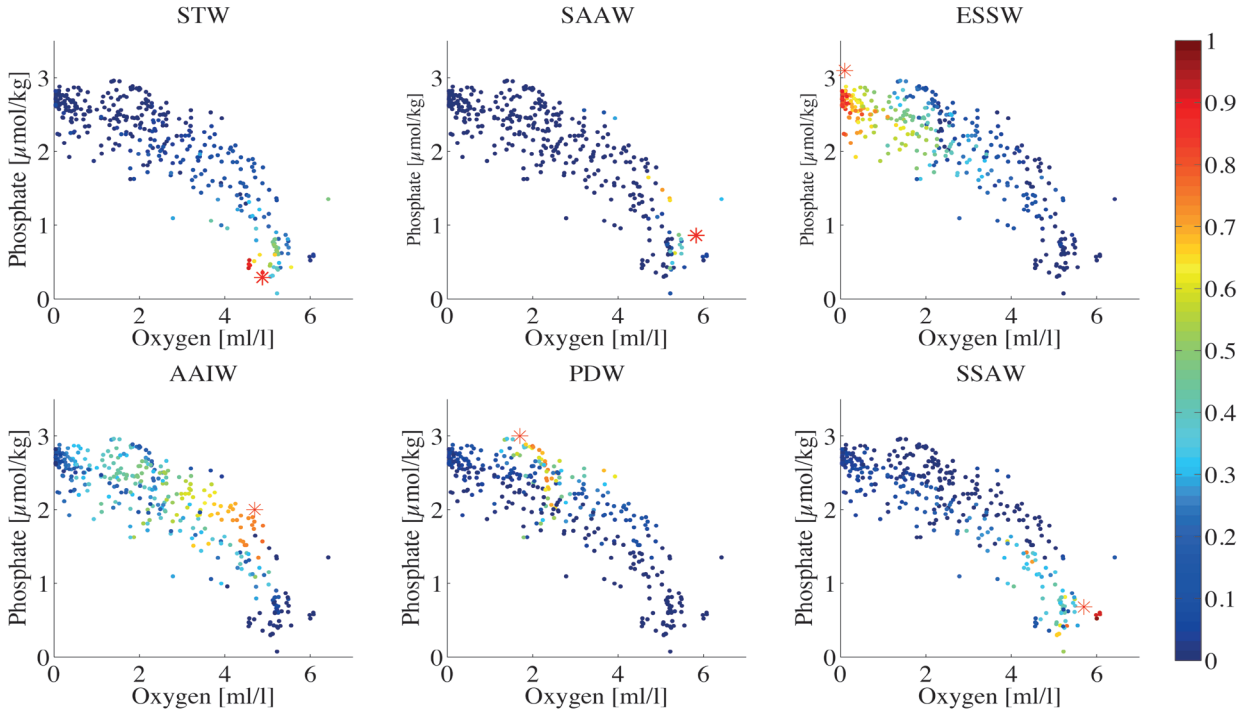

Figure 7. Phosphate-oxygen diagrams showing the relative contribution of each water mass (colour-coded). Top panels: Subtropical Water (STW), Subantarctic Water (SAAW) and Equatorial Subsurface Water (ESSW); bottom panels: Antarctic Intermediate Water (AAIW), Pacific Deep Water (PDW) and Summer Subantarctic Water (SSAW). The water types corresponding to each water mass are shown as a red star.

propagation.

In Figure 9 we show the distribution of the contributions of all water masses for transect M. The upper plot zooms at the surface layers, spanning from the sea surface down to 180 m, and the lower one looks from 180 down to 1400 m. In the surface layers we find SSAW, its core located between 43 and 36ºS and stretching along the whole section S (Figure 10), which is eroded during its equatorward path as it mixes with SAAW and STW. We identify SAAW below SSAW, at depths spanning from 40 to 120 m in the nearshore region of section S and reaching even deeper (180 m) further offshore in section S (Figure 10).This water mass is advected northward by the PCC (Strub et al., 1998), mixing along its path with SSAW and STW, and subducting under STW at the Subtropical Convergence, beyond 35ºS (Silva et al., 2009). On its way it rises over the ESSW, occupying a thinner strata, from 20 m down to 70 m in section C and thinning to a width of about 20 m in section N. SAAW shoals in the nearshore region, displacing STW to the west in sections C and N (Figure 10).

STW is found in the surface and spans a layer up to 45 m thick between 23 and 26ºS (Figure 9). STW is advected poleward from tropical latitudes by the PCCC (Silva et al., 2009). During its path it encounters a wedge of mixed SSAW and SAAW which separates STW from the Chilean coast,

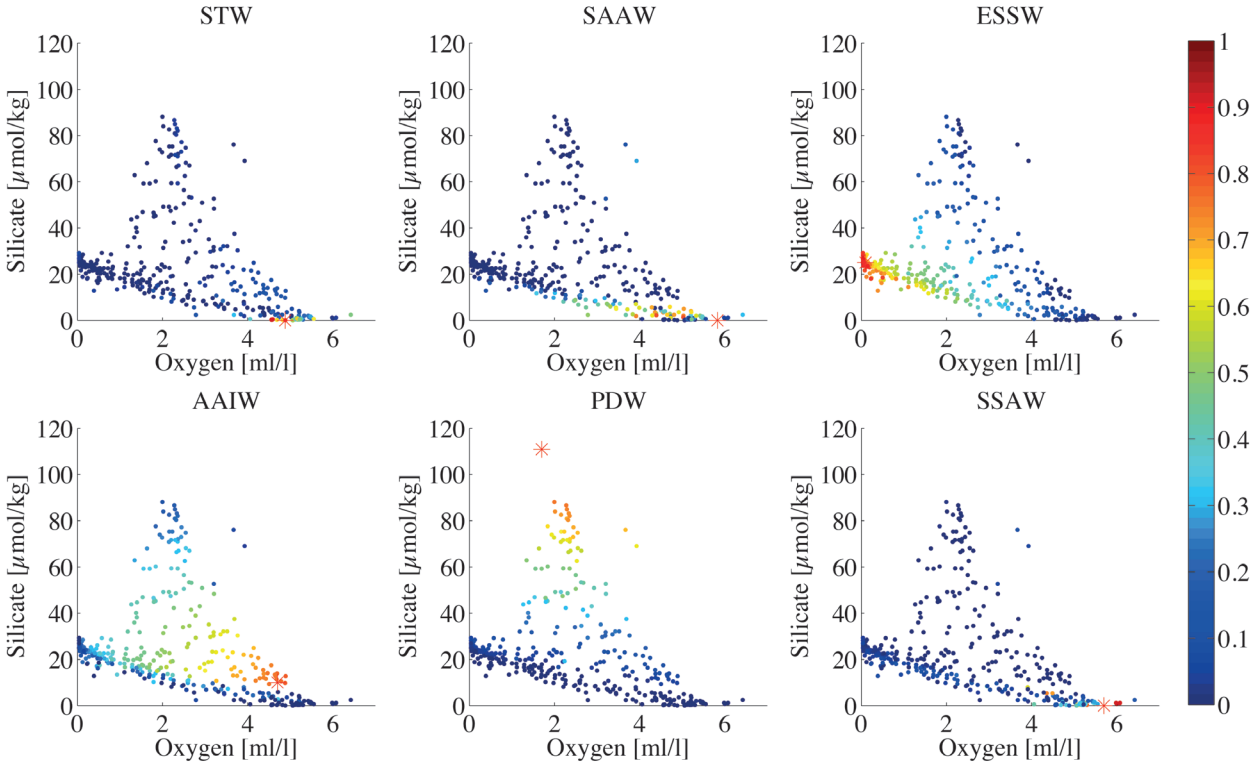

Figure 8. Silicate-oxygen diagrams showing the relative contribution of each water mass (colour-coded). Top panels: Subtropical Water (STW), Subantarctic Water (SAAW) and Equatorial Subsurface Water (ESSW); bottom panels: Antarctic Intermediate Water (AAIW), Pacific Deep Water (PDW) and Summer Subantarctic Water (SSAW). The water types corresponding to each water mass are shown as a red star.

diverting STW further west (Figure 10). Remnants of STW are still found at 75.3ºW in the C zonal transect but it completely disappears in zonal transect S. Below STW we find ESSW, at 23ºS (Figure 9) this water mass occupies about 500 m of the water column, with a relatively shallow core at 140 m depth. The ESSW moves south as a wedge advected by the PU (Leth et al., 2004). On its poleward path, its upper part sinks under SAAW from 70 m in section C to 140 m nearshore in section S (Figure 10). ESSW progressively loses its identity by mixing with SAAW on its upper-side and with AAIW on its bottom-side (Figures 9 and 10).

At intermediate depths we identify AAIW (from 400 down to 1000 m) (Figures 9 and 10), originated north of the APF (Hartin et al., 2011). AAIW is advected equatorward and is progressively eroded as it mixes with quite salty ESSW in its upper-side and with PDW in its bottom-side. AAIW is found along the whole meridional transect and in the three zonal transects, although its participation in the water column at tropical latitudes is relatively small. Its core is located at 600 m depth and spreads northward like a tongue of relatively fresh water with salinity values between 34.1 and 34.3. In addition, AAIW presents a local maximum of dissolved oxygen (3-4.7 ml l^{-1}) and a relative minimum of nutrients (P < 2 µmol kg^{-1}, N < 30 µmol kg^{-1}) (Figures 3 and 4).

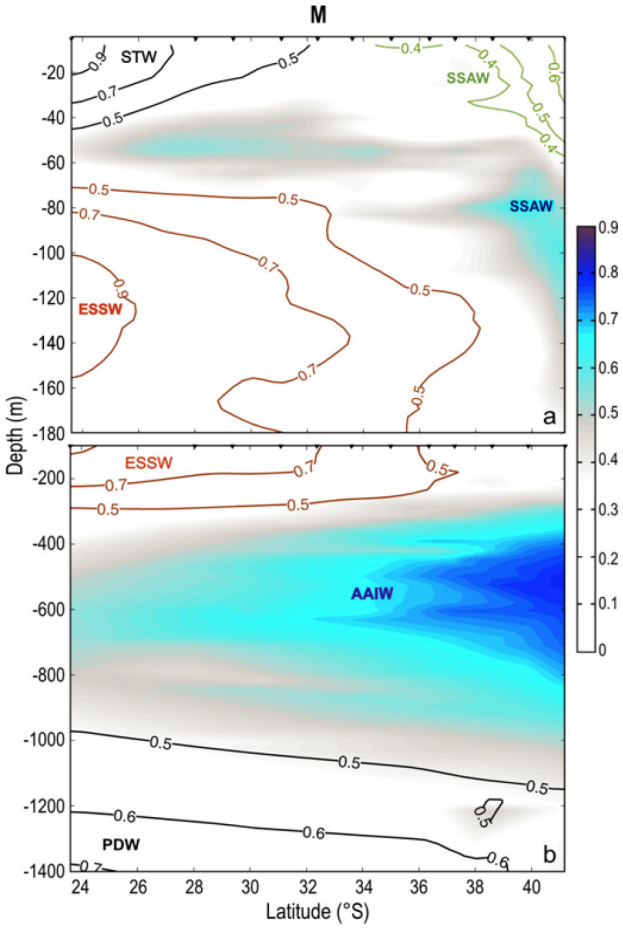

Figure 9. Vertical distributions of the different water masses along the meridional section (M). Upper panel: zoomed down to 180 m depth; bottom panel: down to 1400 m depth. We show the contributions of Summer Subantarctic Water (SSAW) in green solid contour lines, Subtropical Water (STW) in black solid contour lines, SubAntarctic Water (SAAW) colour-coded, Equatorial Subsurface Water (ESSW) in brown solid contour lines, Antarctic Intermediate Water (AAIW) colour-coded and Pacific Deep Water (PDW) in black solid contour lines.

Below AAIW, at depths greater than 1200 m, we find PDW. Here we may only appreciate the upper tip of this water mass, as it extends down to about 3000 m (Silva et al., 2009). This water mass slowly flows south while it mixes with AAIW in its upper-side (Figures 9 and 10). PDW presents values of nutrients/oxygen higher/lower than AAIW (Table 1).

2.5 Conclusions

The analysis of the potential temperature, salinity, inorganic nutrients and dissolved oxygen data from the Humboldt-09 cruise indicates the presence of different surface, intermediate and deep water masses which progressively mix and erode along their particular spreading paths. The distribution of the physico-chemical properties along meridional and zonal transects clearly shows quite stratified water masses that are approximately distributed in four different water strata: near surface (down to ~60 m), central (60 to about 200-400 m), intermediate (200-400 to some 1200 m)

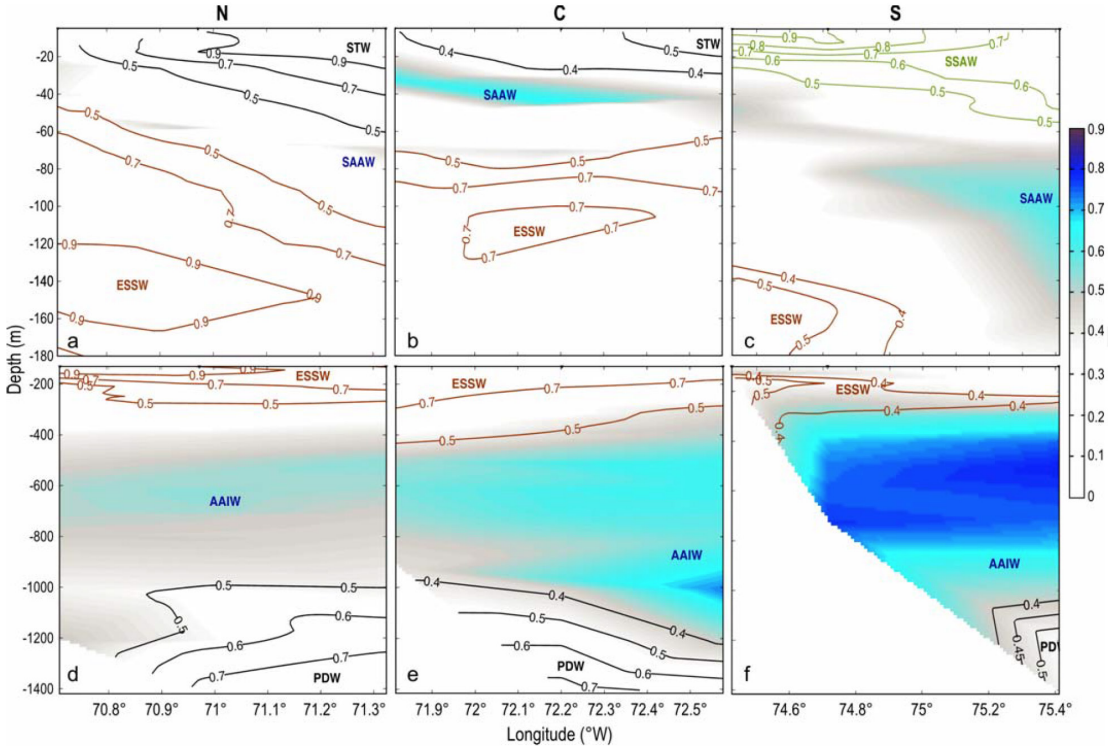

Figure 10. Vertical distributions of the different water masses along the three zonal transects. From left to right we present the (a) northern (N), (b) central (C) and (c) southern (S) transects. Upper panels: zoomed down to 180 m depth; bottom panels: down to 1400 m depth. We show the contributions of Summer Subantarctic Water (SSAW) in green solid contour lines, Subtropical Water (STW) in black solid contour lines, SubAntarctic Water (SAAW) colour-coded, Equatorial Subsurface Water (ESSW) in brown solid contour lines, Antarctic Intermediate Water (AAIW) colour-coded and Pacific Deep Water (PDW) in black solid contour lines.

and deep waters (below 1200 m). One main feature is that surface and central waters, formed within the very large South Pacific subtropical gyre, occupy a relatively thin water stratum as compared with intermediate and deep waters of extratropical origin. This contrasts with other east boundary systems, such as the Canary, Oregon and Benguela Current systems, where central waters reach much deeper (Tomczak and Godfrey, 2003).

Our first task has been to properly identify the potential temperature, salinity, dissolved oxygen and inorganic nutrient values (water types) that characterize the six water masses in the region: SAAW, SSAW, STW, ESSW, AAIW and PDW. To our knowledge there are no inorganic nutrient and dissolved oxygen values in the literature that characterize these water masses, neither potential temperature nor salinity values for SSAW. With the objective of defining these values we have examined the available data and have used the OMP classic and quasi-extended methods to optimize the definition of the water types through an iterative procedure that leads to minimum residuals. The variables that characterize the different water types comprise all the data points (in all different property-property domains, including the classical salinity-potential temperature diagram), and the OMP analysis is able to properly resolve what are the different contributions of the six water masses

to all data points. Table 1 summarizes the characteristic water types we have eventually calculated for the six water masses present in our study area.

The area of interest exhibits a transition from waters of subantarctic origin to those of equatorial and tropical origin. After calculating the contribution of each water mass to all data points we have examined how these relative contributions are depicted in the meridional and zonal sections. The main outcome has been to appreciate that along-slope (meridional) water masses transition is relatively smooth, in contrast with much faster changes in the cross-slope (zonal) direction. This is true at all depths except for deep waters where PDW is the single dominant water mass.

As we move north the contributions from the different water masses change progressively. Near-surface (top 60 m) there is a progressive transition from SSAW and SAAW into STW. Just below, within the upper central waters (60 to 200 m), the southern and northern ends have very little SSAW and STW, respectively, which are replaced by SAAW and ESSW. Further deep, in the northern locations we find that AAIW encounters, subducts and partially mixes with ESSW in the lower central strata (200 to 400 m) while in the southern locations AAIW is the single dominant intermediate water mass (400 to 1000 m). Between 1000 and 1100 m we still find AAIW at the southern locations but further north this depth range is occupied by PDW.

In contrast with the smooth changes in water properties found along latitude, water masses change much more abruptly in the cross-shore direction. Near the sea surface (top 60 m) SSAW dominates in section S, SAAW and STW (further offshore) alternate in section C, and STW is the dominant water mass in section N. Just below (60 to 200 m) we find greater variability, with ESSW and SAAW present in all sections, ESSW dominating at low latitudes and higher depths and SAAW at high latitudes. The SAAW is found deeper as we move offshore in section N but at shallower depths in section C. Further deep we find substantially less cross-shore variability, with ESSW as the single dominating water mass between 200 and 400 m except in section S where some SAAW is present offshore. Below ESSW, AAIW is the predominant water mass down to 1100 m. Further deep PDW is the prevailing water mass.

A remarkable feature in our data is the contrast of low salinity, low nutrient and high oxygen AAIW and relatively high salinity, high nutrients, and very low oxygen ESSW. These are the two dominant water masses between about 250 and 650 m throughout the whole meridional transect. Approximately 40% of AAIW is found between 250 and 1100 m at 44ºS and between 550 and 650 m at 23ºS (it deepens equatorward), while there is more than 40% ESSW between 550 and 650 m at 44ºS and between 50 and 550 m at 23ºS. The ESSW is associated to very low dissolved oxygen and high nutrient values, i.e. with the OMZ. This tongue stretches south illustrating the penetration of this water centered at 250 m. The low oxygen content of ESSW may influence the underlying AAIW and

even PDW at low latitudes, as suggested by Silva et al. (2009). The southern part of the OMZ in the Eastern South tropical Pacific is ventilated by mixing on its upper part with SAAW and with AAIW on its lower part. Changes in the contribution of these water masses in the water column may reflect changes in the climatic conditions of their source regions. These changes could eventually disrupt the ventilation of the southern part of the OMZ, conditioning its future evolution. Since a long-term trend of expanding OMZ has been reported for the tropical oceans (Stramma et al. 2008), future works might find the OMP method useful to explain how changes in the OMZ extension respond to changes in the water mass contributions to the water column in that region.

The differences observed in meridional and zonal gradients are undoubtedly the outcome of the regional circulation patterns with rather narrow meridional jets that stretch over our whole domain (Silva et al., 2009). These jets become paths for substantial meridional transport over long distances, hence bringing tropical water into subantarctic regions and vice versa, but also act to enhance cross-slope zonal gradients. Our results can only give some hints about the regional offshore variability, being limited by the relatively low number of zonal sections and their small offshore extension, but yet point at the high variability of the water masses in this important climatic region and the necessity of carrying out further physico-chemical characterizations of this region in the future.

Acknolwledgements

PL is supported by a JAE-predoc assistantship from the Consejo Superior de Investigaciones Científicas and the European Social Fund. The Humboldt-09 cruise was supported through project "Campaña Oceanográfica Humboldt-2009, Tránsito de Retorno del BIO Hesperides Primavera 2009" (CTM2008-02497-E/MAR), financed by the Spanish Ministerio de Ciencia e Innovación. The authors would like to thank the crew and technical staff at the R/V Hesperides during cruise Humboldt-09, particularly Joaquim Llinàs, Javier Vallo and Marcos Pastor for their help with the measurements. We are very grateful to Fiz Fernández and Jesús Peña for useful comments regarding the OMP analysis and to Maravillas Abad for the inorganic nutrient analysis.

CHAPTER

3

Physical and biogeochemical forcing of oxygen and nitrate changes during El Niño/El Viejo and La Niña/La Vieja upper-ocean phases in the tropical eastern South Pacific along 86° W

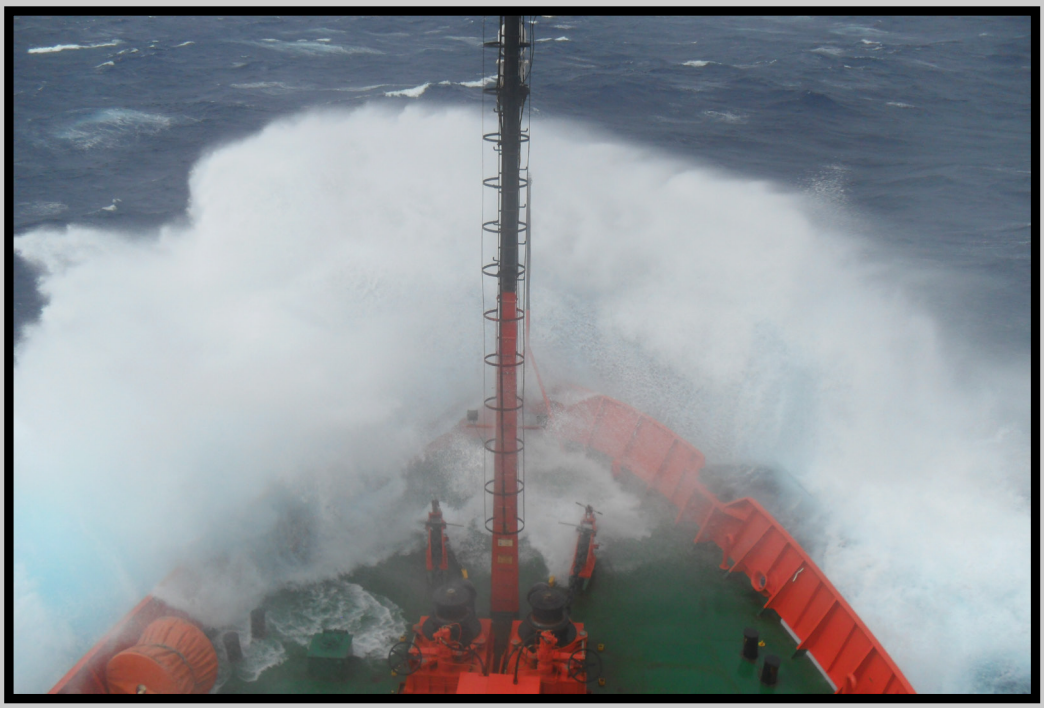

Llanillo, P. J., Karstensen, J., Pelegrí, J. L., and Stramma, L.: Physical and biogeochemical forcing of oxygen and nitrate changes during El Niño/El Viejo and La Niña/La Vieja upper-ocean phases in the tropical eastern South Pacific along 86° W, Biogeosciences, 10, 6339-6355

"The sea complains upon a thousand shores."
Alexander Smith

Abstract

Temporal changes of the water mass distribution and biogeochemical signals in the tropical eastern South Pacific are investigated with the help of the extended Optimum Multi-Parameter (OMP) analysis, a technique for inverse modelling of mixing and biogeochemical processes through a multidimensional least-square fit. Two ship occupations of a meridional section along 85°50'W from 14ºS to 1ºN are analysed during relatively warm (El Niño/El Viejo, March 1993) and cold (La Niña/La Vieja, February 2009) upper-ocean phases. The largest El Niño - Southern Oscillation (ENSO) impact was found in the water properties and water mass distribution in the upper 200 m north of 10ºS. ENSO promotes the vertical motion of the Oxygen Minimum Zone (OMZ) associated to the hypoxic Equatorial Subsurface Water (ESSW). During a cold phase the core of the ESSW is found at shallower layers, replacing the shallow (top 200 m) Subtropical Surface Water (STW). The heave of isopycnals due to ENSO partially explains the intrusion of oxygen-rich and nutrient-poor Antarctic Intermediate Water (AAIW) in the depth range of 150 to 500 m. The other cause of the AAIW increase at shallower depths is that this water mass flows along shallower isopycnals in 2009. The shift in the vertical location of AAIW reaching the OMZ induces changes in the amount of oxygen advected and respired inside the OMZ, the largest the oxygen supply the greatest the respiration and the lowest the nitrate loss by denitrification. Variations in the intensity of the zonal currents in the Equatorial Current System, which ventilates the OMZ from the west, are used to explain the patchy latitudinal changes of seawater properties observed along the repeated section. Significant changes reach down to 800 m, suggesting that decadal variability (Pacific Decadal Oscillation) is also a potential driver for the observed variability.

Chapter 3

3.1 Introduction

Oxygen minimum zones (OMZs) exist with different intensity in the upper thermocline of the eastern subtropical gyres of the Pacific and Atlantic Oceans as well as in the northern Indian Ocean (Karstensen et al., 2008; Paulmier and Ruiz-Pino, 2009). When dissolved oxygen falls below a certain critical level, widespread mortality or avoidance of affected areas will result (Vaquer-Sunyer and Duarte, 2008). Expansion of the OMZs will narrow down the habitable depth range of fishes and, along with overfishing, may threaten the sustainability of pelagic fisheries and marine ecosystems (e.g. Stramma et al., 2012a). Decreasing oxygen concentrations and OMZs expansion have been found for all tropical oceans (Stramma et al., 2008; Stramma et al., 2010b) perhaps as part of a long term decadal type variability (Deutsch et al., 2011). However, increasing oxygen content has been reported to occur between 200 and 700 m south of 15ºS in the Pacific (Stramma et al., 2010b). The characteristics and variability of the OMZs are driven by physical and biological processes. Because of the upwelling of nutrient rich waters in the eastern boundary regions, the waters overlying the eastern South Pacific OMZ belong to the most productive areas in the world ocean (Strub et al., 1998). In this paper we will use two occupations of a section along 85º50'W, carried out in 1993 and 2009, to examine the temporal evolution of the OMZ in the tropical eastern South Pacific Ocean. The area of investigation goes from the northeastern rim of the South Pacific subtropical gyre to the southern part of the Panama Basin (from 14ºS to 1ºN) (Figure 1A). It is a region poorly ventilated by the eastern part of the Equatorial Current System and by the northern part of the Peru-Chile Current system with relatively long residence times (Kessler, 2006). A schematic of the currents is shown in Figure 1B.

This region is influenced by El Niño/La Niña - Southern Oscillation (ENSO), one of the strongest modes of interannual variability in the global ocean/atmosphere system (e.g. Philander, 1983). El Niño and La Niña respectively refer to the warm and cold ocean phases of the near-surface waters in the central and eastern Pacific Ocean. During an El Niño event the upwelling of nutrient-rich waters off the Peruvian coast is suppressed with dramatic consequences for fisheries (Barber and Chavez, 1983).

The two occupations of the 85°50'W transect represent contrasting ENSO phases. The 1993 cruise was completed during a weak warm event (the Oceanic Niño Index, ONI, was 0.5 for the February to March period) which was not catalogued as an El Niño because it lasted only four rather than the required five consecutive seasons. The 2009 cruise was accomplished during a weak to moderate cold period (ONI was -0.9 for December to February) which was neither catalogued as La Niña for the same reason (it lasted only four consecutive seasons). However, for the purpose of this study, we will consider the 1993 warm event as an El Niño event and the 2009 cold event as a La

Niña event because the magnitude and the sign of the ONI index during both events qualify for this consideration, despite not lasting long enough to meet the duration criteria.

Superimposed onto the ENSO variability, the region is influenced by the Pacific decadal oscillation (PDO) which operates on time scales of several decades (Mantua et al., 1997; Chavez

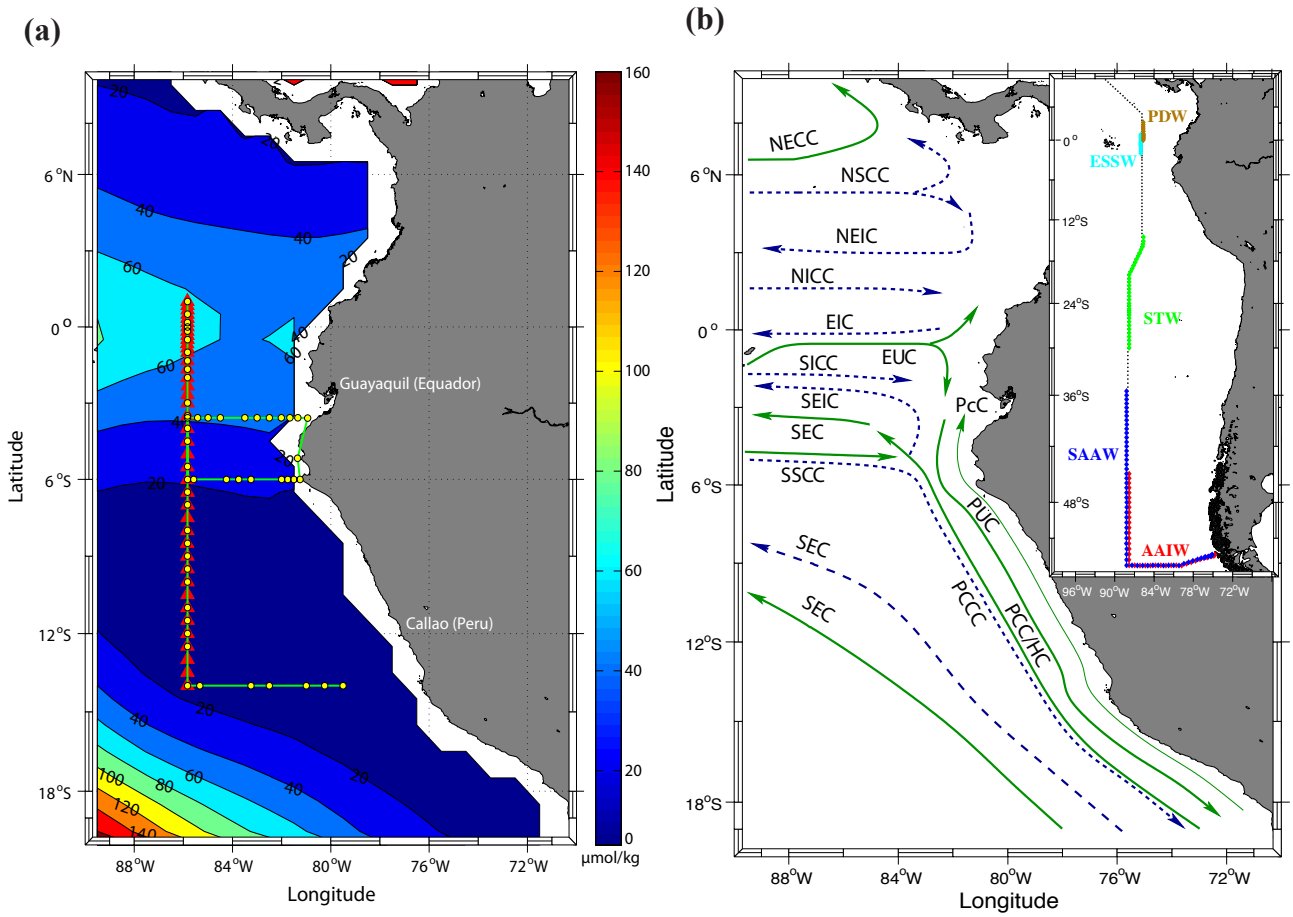

Figure 1. (a) Map of the study area with the track (green line) of the Meteor cruise M77 (February 2009) and stations between 14°S and 1°N (red triangles) of the WOCE P19 cruise (March 1993). The yellow dots indicate the rosette stations of the M77 cruise selected for the extended OMP analysis. The background shows the climatological mean of dissolved oxygen (μmol/kg) at 200 dbar from the World Ocean Atlas 2009 (data available at http://www.nodc.noaa.gov/OC5/WOA09/pr_woa09.html), **(b)** Circulation scheme for currents in the upper 200 m (green lines) and 200 to 600 m (blue dashed lines) layers based on descriptions provided by Kessler (2006), Czeschel et al. (2011) and Grasse et al. (2012); notice that some current bands may be covering both depth layers. The current shown are: NECC – North Equatorial Counter Current, NSCC – Northern Subsurface Counter Current, NEIC – North Equatorial Intermediate Current, NICC – North Intermediate Counter Current, EIC – Equatorial Intermediate Current, EUC – Equatorial Undercurrent, SICC – South Intermediate Counter Current, SEIC – South Equatorial Intermediate Current, SSCC – Southern Subsurface Counter Current, SEC – South Equatorial Current, PCCC – Peru Chile Counter Current, PCC/HC – Peru Chile or Humboldt Current, PcC – Peru coastal Current and PUC – Poleward Undercurrent. The inset shows the source regions (coloured) along the P19 cruise track, where the source water masses (Table 1) were defined.

et al., 2003). The PDO also oscillates between warm (El Viejo) and cold (La Vieja) phases that go along with changes in sea surface height, sea surface temperature (SST), thermocline depth and ocean currents. Given their different time scales, ENSO has more impact on upper water masses while the PDO can induce more substantial changes over the whole permanent thermocline and intermediate layers, e.g. influencing the dissolved oxygen content down to 700 m in the water column (Stramma et al., 2010a; Czeschel et al., 2011). A recent model study (Deutsch et al., 2011) showed that the PDO can modify the thermocline depth and thus trigger an upward migration of the OMZ during La Vieja phases. In the middle to late 1990s there was a shift to the cold phase (Chavez et al., 2008; Chavez et al., 2003), therefore the 1993 cruise was accomplished by the end of an El Viejo whereas the 2009 cruise took place under La Vieja conditions.

The eastern tropical Pacific OMZ is an important sink for oceanic-fixed nitrogen in the world oceans (e.g. Morales et al., 1999; Codispoti et al., 2001). The oceanic nitrogen can be removed in two ways. First, via denitrification, i.e. the heterotrophic reduction of nitrate (NO_3) through several steps with the gaseous dinitrogen (N_2) as the final product. This process has been observed typically for waters with dissolved oxygen concentrations less than 5 µmol/kg, although recent studies indicate it remains active until higher concentrations (Codispoti et al., 2001; Kalvelage et al., 2011). Second, via the anammox process, i.e. the anaerobic oxidation of ammonium (NH_4^+) with nitrite (NO_2^-), that produces N_2 and water as the final products (Kuypers et al., 2005; Lam et al., 2009; Kalvelage et al., 2011). In the Peruvian OMZ, the nitrite produced during denitrification represents two thirds of the nitrite used for anammox (Lam et al., 2009). Recent studies point to anammox as the most important pathway for nitrogen removal within the OMZ (Kuypers et al., 2005; Thamdrup et al., 2006; Hamersley et al., 2007; Kalvelage et al., 2011).

Tsuchiya and Talley (1998) presented a comprehensive discussion about the structure of water masses along 85°50'W. Basically, five different water masses were identified to contribute to the Southeast Pacific Ocean. The top 200 m are occupied by Subtropical Water (STW) and Subantarctic Water (SAAW). Immediately below, and down to about 600 m, the Equatorial Subsurface Water (ESSW) is the predominant water mass. Coexisting with ESSW and reaching further deep, between about 500 and 1000 m, there is a significant contribution of Antarctic Intermediate Water (AAIW). The deep layers, at depths greater than about 1100 m, are dominated by the Pacific Deep Water (PDW). In this study we will thoroughly characterise the properties of these water masses and use the extended Optimum Multi-Parameter (OMP) analysis to quantify the changes in water mass contributions and biogeochemical processes between the 1993 and 2009 occupations. In addition, we will analyse three zonal sections (along 3°35'S, 6°S and 14°S) carried out in 2009, running between the continental shelf region and 85°50'W (Figure 1A).

The OMP analysis (Tomczak and Large, 1989) has been used in the past to examine the distribution of water masses in the eastern South Pacific: off Chile (Silva et al., 2009), along the Chilean continental slope (Llanillo et al., 2012) and south of 10°S (De Pol-Holz et al., 2007). Here we will use the extended OMP analysis (Karstensen and Tomczak, 1998; Hupe and Karstensen, 2000), which decomposes the observed parameter distribution into contributions that originate from water mass mixing and those that stem from remineralization/respiration as well as denitrification processes. In this way, it is possible to investigate the relative roles of both ocean transport (linked to the advection and mixing of water masses) and biogeochemical processes on the changes arising between the two cruises.

Table 1. Source water types used for the extended OMP analysis. The source water masses are Subtropical Water (STW), Subantarctic Water (SAAW), Equatorial Subsurface Water (ESSW), Antarctic Intermediate Water (AAIW) and Pacific Deep Water (PDW). The weights used for each parameter are included at the bottom row. The oxygen saturation concentrations based on the source water type temperature and salinity are given in the last column (based on Garcia and Gordon, 1992).

Water mass	Pot. Temp. (°C)	Salinity	Oxygen (μmol kg^{-1})	Phosphate (μmol kg^{-1})	Silicate (μmol kg^{-1})	Nitrate (μmol kg^{-1})	Oxygen saturation
STW	20.8	35.52	240.65	0.46	2.23	0.74	221.55
SAAW	11	34.00	268.2	1.07	2.17	13.7	270.74
ESSW	10	34.80	13.6	2.43	29.81	32.7	275.00
AAIW	3.0	34	238.2	1.97	24.6	28.5	324.97
PDW	1.82	34.67	105.2	2.76	157.3	38.42	332.94
Weight	24	24	7	7	3.5	7	Mass cons. 24

3.2 Data Set and Methodology

3.2.1 Observational data

Our study is based on two data sets taken in 1993 and 2009 respectively, which include both conductivity-temperature-pressure (CTD) and oxygen/nutrient (bottle) data. The P19 data set was acquired during the World Ocean Circulation Experiment (WOCE) aboard R/V Knorr, with full-depth stations from Southern Chile to Guatemala. The section runs along 88°W in the South Pacific but shifts to 85°50'W in the equatorial Pacific (Tsuchiya and Talley, 1998). The stations between 14°S and 1°N were carried out from 23 to 31 March 1993. About 16 years later, from 27 January to 19 February 2009, the R/V Meteor cruise M77/4 (hereafter M77) reoccupied the WOCE P19 stations between 14°S and 1°N, with stations separated (on average) by about 60 km, although with improved resolution near the equator (Figure 1A). M77 focused on the OMZ waters and therefore most of the stations reached down to only 1200 dbar. The two cruises covered the tropical region during approximately the same season (about 1.5 months difference) so the seasonal differences are

expected to be small as compared to the interannual and interdecadal changes. The sampling accuracy of the data from M77(P19) cruise was respectively: <0.001(0.002) for salinity, 0.72(1.34-1.78) µmol/l for oxygen, 0.278(0.3-0.4) µmol/l for nitrate, 0.009(0.02-0.03) µmol/l for phosphate and 0.18(1-2) µmol/l for silicate.

The bottle data from both cruises and the results obtained with the OMP analysis (applied at each data point) have been objectively interpolated onto a regular grid with 25 m spacing in depth and 60 km horizontal spacing, from just below the average mixed layer depth (55 m) down to 1200 m. An influence radius of 100 km in the horizontal and an increasing influence radius from 15 m at 55 meters to 250 m at 1200 meters in the vertical were applied. A comparison (not shown) of temperature, salinity and oxygen data, available at both low (bottle) and high (CTD) vertical resolution, reveals that the interpolated bottle data reproduces well the CTD data distribution. Therefore, for this study we have used interpolated bottle data for all parameters.

3.2.2 Extended Optimum Multi-Parameter (OMP) analysis

The extended OMP analysis (Hupe and Karstensen, 2000; Karstensen and Tomczak 1998) evolved from the inverse modelling techniques described by Mackas et al. (1987) and Tomczak and Large (1989). The OMP analysis finds solutions, in the form of water mass fractions, to a set of linear mixing equations. In contrast to the classical mixing-triangle approach, which is based on temperature and salinity only, the OMP analysis utilizes more parameters (such as oxygen and inorganic nutrients) to determine the water mass fractions which are required to be non-negative. The extended analysis is based on a multidimensional least-square fit that allows resolving the mixing of more than three water masses as well as the biogeochemical cycling (respiration, remineralization and denitrification signals).

The application of the OMP analysis requires a correct definition of the source water masses expected to contribute to the observed parameter field. To control the influence of a certain parameter on the solution, a weighting is applied (Table 1, last row). This weighting considers the environmental variability within the region of water mass formation and the overall span of the parameter space in the source water matrix (Tomczak and Large 1989). Further details on the technique, such as the data normalization scheme and the parameter weighting criteria, can be found in Tomczak and Large (1989).

The standard OMP analysis assumes that all parameters are conservative quantities, that is, they are only modified by mixing. This is difficult to justify when biogeochemical processes, such as the remineralization of organic matter and denitrification are likely to contribute to the observed parameter distribution. The extended OMP analysis (Hupe and Karstensen 2000; Karstensen and

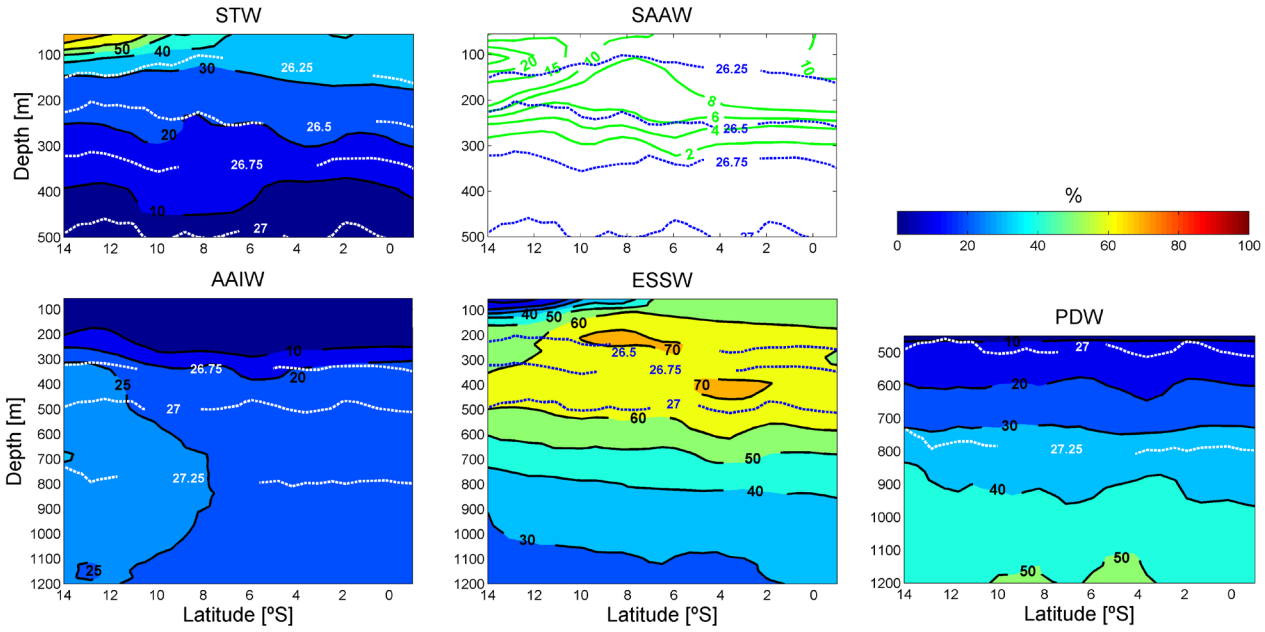

Figure 2A. Water mass distribution (%) along the 85°50'W section between 14°S and 1°N for the M77 cruise (February 2009) for Subtropical Water (STW), Subantarctic Water (SAAW), Antarctic Intermediate Water (AAIW), Equatorial Subsurface Water (ESSW) and Pacific Deep Water (PDW) as defined in Table 1. Selected isopycnals are shown as dotted white/blue lines.

Tomczak 1998, Poole and Tomczak 1999) solves this issue (the non-conservative behaviour of parameters) by adding stoichiometry-scaled remineralization/respiration (influencing oxygen, nitrate, phosphate and silicate) and denitrification (influencing nitrate and phosphate) processes to the set of linear equations. The solution technique follows that for the standard OMP, the system must be over-determined in order to ensure an unambiguous solution and to provide for error estimates. Given the available parameters in the M77/P19 data sets (potential temperature θ, salinity S, dissolved oxygen O_2, nitrate NO_3, phosphate PO_4, and silicate SiO_4) and assuming mass conservation (sum of water mass fractions is one), the contribution of up to four source water masses and the transformations due to remineralization/respiration and denitrification can be resolved.

The extended OMP analysis is also based on the assumption that the source waters are time-invariant. Hence, changes in the water mass fractions and the biogeochemical signals are interpreted to respond solely to the redistribution of water masses and to a different biogeochemical cycling (remineralization, denitrification). To quantify the influence of temporal and natural variability on the results, we have run a series of sensitivity tests by simultaneously perturbing all water types with Gaussian noise in a series of Monte Carlo experiments (see supplementary material). From these tests we conclude that the influence of temporal and natural variability is low and the results obtained are robust.

The extended OMP analysis has been applied to the data of each transect but excluding those data points located within the mixed layer, as they are influenced by air/sea interaction processes which are not considered in the set of equations and may introduce sources and/or sinks to the thermodynamic parameters (Holte et al., 2012).

3.2.3 Source water masses

To apply the OMP analysis to the P19 and M77 data we first identify all possibly contributing source water masses mainly based on the discussions by Tsuchiya and Talley (1998) and Fiedler and Talley (2006). Characterized by a subsurface salinity maximum (~35.5) (Wyrtki, 1967), the STW is formed to the southwest of the 85º50'W transect by shallow subduction in a region where evaporation exceeds precipitation (Stramma et al., 1995). The Shallow Salinity Minimum Water (Reid, 1973; Tsuchiya and Talley, 1998; Karstensen et al., 2004) originates through the subduction of SAAW under STW, in the region between the Subantarctic and the Subtropical Fronts all along the southern rim of the South Pacific subtropical gyre. Not to be confused with the deeper (600-1100m) salinity minimum of AAIW (~34), the SAAW is characterized by a salinity minimum at about 11°C and salinities around 34.0, located between 100 and 200 m. The SAAW is advected north with the Peru-Chile (PCC) or Humboldt Current (HC) (Wyrtki, 1967) and partially ventilates the upper part of the OMZ (Figure 1B).

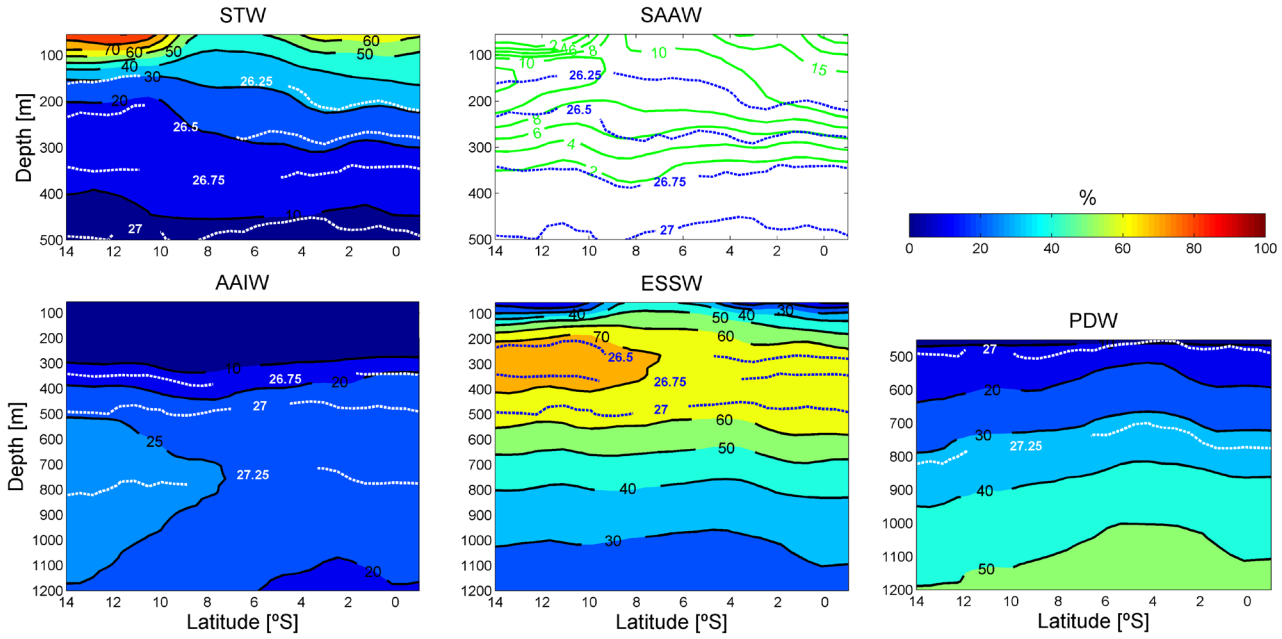

Figure 2B. Water mass distribution (%) along the 85°50'W section between 14°S and 1°N for the P19 cruise (March 1993) for Subtropical Water (STW), Subantarctic Water (SAAW), Antarctic Intermediate Water (AAIW), Equatorial Subsurface Water (ESSW) and Pacific Deep Water (PDW) as defined in Table 1. Selected isopycnals are shown as dotted white/blue lines.

Being a product of multiple and complex mixing in the equatorial region (Wyrtki, 1967), the ESSW is advected with relatively high oxygen content (~69.7 μmol/kg), into the OMZ region by the eastward Equatorial current system, mainly by the Equatorial Undercurrent (EUC) (Stramma et al., 2010a). ESSW spreads southwards very slowly, almost stagnant, into the OMZ region where its oxygen content decreases even further (~13.6 μmol/kg, in the P19 stations used as source region for ESSW, Figure 1B). ESSW is slightly less salty (~34.8) and colder (~10ºC) than the overlaying STW (~20.8ºC) and presents higher nutrient and lower oxygen concentrations than the STW. Part of the nutrient-rich ESSW contributes to the waters that upwell along the Peruvian coast (Brink et al., 1983).

The prominent salinity minimum that characterizes the AAIW is already eroded (~34.54) at this latitude range. This salinity minimum is located under both ESSW and SAAW, centred at depths between 600 and 1100 m. Formed by subduction between the Subpolar and Polar Fronts (Hartin et al., 2011), the AAIW source water has high oxygen and low nutrient concentrations. Below the AAIW and centred at depths between 2500 and 3000 m, the PDW is characterized by a broad silicate maximum (~157.3 μmol/kg). PDW comes to this region following an intricate path through the North Pacific and it is believed to be the return flow of modified bottom waters originated at the South Pacific in the Antarctic Circumpolar Current (ACC) (Reid 1973; Tsuchiya and Talley 1998). As we concentrate our analysis in the upper 1200 m of the water column, other deep waters such as the Circumpolar Deep Water or the Antarctic Bottom Water are not considered here.

The initial step for defining the source water characteristics (summarized in Table 1) is to set the temperature/salinity source water values (water types) using information available in the literature (Tsuchiya and Talley, 1998; De Pol-Holz et al., 2007; Silva et al., 2009; Llanillo et al., 2012). Next, the data points within a range of temperature and salinity values, centred on the temperature/salinity water type definition for each water mass, are selected. Then, we impose geographical and depth constraints to pick only those data points that actually lay within the defined water mass formation areas. Finally, the selected data points are used to calculate the associated nutrient (NO_3, PO_4 and SiO_4) and oxygen source water types by averaging their respective values (Table 1).

The location where the formation areas are defined determines the initial water types, influencing also the OMP-derived mixing fractions and biogeochemical signals (the bulk biogeochemical processes are derived in reference to the characteristics of the source water masses). As the purpose of our study (and accordingly our interpretation) is on the regional changes in water-mass structure and remineralization/respiration/denitrification processes, we have defined all source water formation areas within the P19 cruise line track (Figure 1B). We do not attempt to over-interpret the data, thus we avoid making statements on the full along-path transformation and biogeochemical cycling of all water masses. For this purpose we would need to define all source water masses in their original formation region at the surface.

To assess if these initial source water types are properly defined, we have investigated the stability of the OMP results through a series of Monte Carlo simulations, where random Gaussian noise is added to the parameters with the largest weights on the solution (temperature and salinity). This technique allows us to optimize the source water types as those that have the lowest residuals. The final water types are presented in Table 1.

The remineralization of organic matter and the associated respiration are included in the analysis via a set of Redfield ratios (Redfield et al., 1963), as they connect the changes in inorganic nutrients and oxygen. We use the Redfield ratios -170:16:1 corresponding to ΔO_2:ΔNO_3:ΔPO_4 (Anderson and Sarmiento, 1994). The ratio ΔSiO_4:ΔPO_4 is affected by the dissolution of opaline silica (Hupe and Karstensen, 2000) and shows regional variations depending on the plankton composition (Poole and Tomczak, 1999). Therefore, we used all available data to compute the best linear fit between silicate and phosphate for each cruise. The obtained values are 14.5:1 for the M77 dataset and 18.4:1 for the P19 dataset (see the supplementary material). However, we acknowledge that silicate shows different behaviour with depth, being remineralized deeper than the other parameters bound in the organic matter. Therefore silicate will show a non-constant ratio with phosphate and nitrate during remineralization/dissolution. Taking this into account we assigned silicate the lowest weight (Table 1), so this parameter has only a weak influence on the solution.

Furthermore the amount of PO_4 remineralized during denitrification is assumed to follow a ratio of -1:0.01 for ΔNO_3:ΔPO_4 (Gruber and Sarmiento, 1997). The extended OMP analysis only accounts for the first step of the denitrification process (the anaerobic reduction of NO_3 to NO_2). Whether this NO_2 is then used in the anammox process or follows the denitrification route, ending both in the loss of oceanic nitrate, cannot be elucidated with the current extended OMP analysis.

The OMP analysis is divided in two depth ranges (upper and lower) in order to limit the number of source water masses and to ensure an over-determined system of equations. We decided to break the OMP analysis at the 450 m depth horizon because in this way the residuals are minimized in the upper part of the analysis (close to this cutting depth). Additionally, this cutting depth prevents the relatively higher residuals, characteristic of the upper part (0 - 4%), from appearing in the lower part, which is characterized by much lower residuals. Finally, this partition leads to a smooth transition in the mixing fractions of ESSW and AAIW between the upper and lower part of the analysis. We run the upper analysis with STW, SAAW, ESSW and AAIW and the lower analysis with ESSW, AAIW and PDW. To account for possible outliers in the data set, only those results from the OMP analysis which have mass conservation errors less than ~ 4% are considered; following this condition, we discarded 0.5% of the data points in M77 section and 0.7% of the data points in P19 section.

3.3 Results

In this section we present the results derived from applying the extended OMP analysis to both the P19 and M77 cruise data, specifically the contribution of the different water masses and the biogeochemical signals (respiration, denitrification) along the oceanographic sections. These quantities are useful descriptors of the regional physical and biogeochemical processes. In addition, the differences between the results obtained for both occupations (Section 3.3.3) will provide information on the changes in time.

3.3.1 Water mass distribution

The water mass distribution for the recent M77 data, as obtained with the extended OMP analysis, illustrates the coexistence and mixing of water masses of equatorial, subtropical, subantarctic and antarctic origin along the 85°50'W section, between 14ºS and 1ºN (Figure 2A). The distribution obtained for the P19 data (Figure 2B) along the same latitude range shows similar patterns to those found in M77 data and complements an earlier distribution obtained by applying the classic OMP analysis (De Pol-Holz et al., 2007) to the southern part of the P19 section (50-10ºS). The general patterns along the whole P19 section are already visible from individual parameter distributions (e.g. presented in Tsuchiya and Talley, 1998). In brief, the shallow layers are composed by subtropical (STW), subantarctic (SAAW) and equatorial (ESSW) water masses, while at intermediate depths there is predominance of equatorial waters (ESSW) that overlay the antarctic waters (AAIW). For levels deeper than about 1100 m the predominant water mass is PDW.

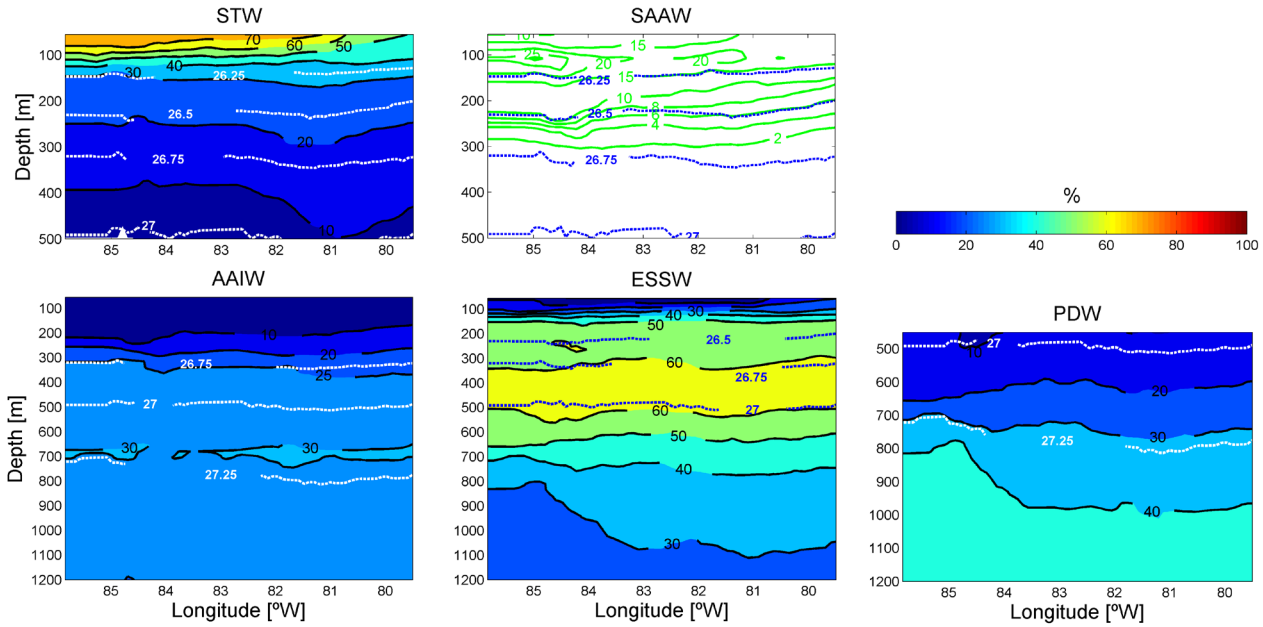

Figure 3. Water mass distribution (%) along the 14ºS section between 85°50'W and the continental shelf for the M77 cruise (February 2009) for Subtropical Water (STW), Subantarctic Water (SAAW), Antarctic Intermediate Water (AAIW), Equatorial Subsurface Water (ESSW) and Pacific Deep Water (PDW) as defined in Table 1. Selected isopycnals are shown as dotted white/blue lines.

STW is best represented (>50-60%) in the top 100 m, between 14 and 10ºS, closer to its source region. SAAW is also well distinguished south of 10ºS, reaching up to 20% in the uppermost layer and below the STW, but is not significant (<4%) below 250-300 m. The ESSW core, with a mixing fraction of about 70%, is located between 200 and 400 m. AAIW contributes more than 25% at the southern boundary of the region, with its core located at 700 m. AAIW is slowly diluted to the north and replaced mainly by ESSW (Figure 2A).

In the equatorial region (4ºS-1ºN) there are remnants of low-salinity waters of equatorial origin down to 200 m. These waters most likely originated north of the equator, in the Panama Bight, where enhanced precipitation under the Intertropical Convergence Zone (ITCZ) creates low salinity surface waters that are subsequently advected to the south, eventually crossing the equator (Tsuchiya and Talley, 1998). However, this water mass was not considered in the OMP analysis because the system of equations would no longer be overdetermined. Furthermore, its inclusion would not add additional information as the selected OMP configuration is already capable of recognizing the fresh fingerprint of these equatorial waters, associating them to the also relatively fresh SAAW, which is almost totally eroded north of 10ºS. Therefore, the observed presence of SAAW north of 4ºS is to be instead associated to the presence of these equatorial fresh waters.

The distribution of water masses between 85º50'W and the continental shelf was also deduced along three zonal sections carried out during the M77 cruise (2009) at 14ºS, 6ºS and 3°35'S, (Figures 3-5). SAAW has the highest percentage (>20%) in the western part of the 14°S transect (Figure 3) but is generally under 8% at 6ºS (Figure 4) and increases again in the surface layers to about 10% at 3º35'S (Figure 5). This increase is very likely an artifact caused by the presence of low-salinity equatorial surface waters as discussed above, and as also proposed by Tsuchiya and Talley (1998). The AAIW participation reaches 30% centred at 700 m along the whole transect at 14°S (Figure 3) and decreases towards the equator with maximal contributions of 20% at 3°35'S (Figure 5). The observed decrease in the mixing fractions of both AAIW and SAAW north of 14ºS agrees well with their northward path along the subtropical gyre.

The contribution of STW decreases rapidly as we move from the southern to the central and northern sections. This confirms the progressive recirculation of this water mass towards the ocean interior, south of the Equatorial Front, and back poleward along the boundary, as a result of advection by the Peru-Chile Counter Current (PCCC) (Strub et al., 1998). This can be appreciated at the offshore end of section 14ºS (Figure 3).

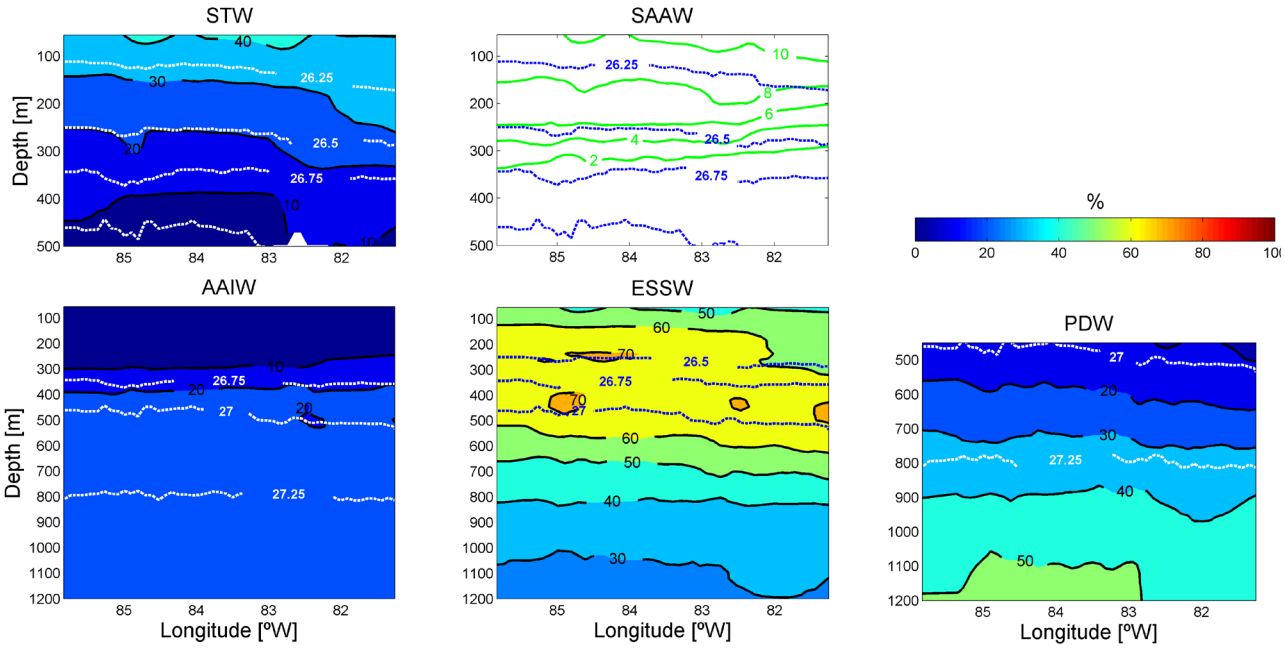

Figure 4. Water mass distribution (%) along the 6°S section between 85°50'W and the continental shelf for the M77 cruise (February 2009) for Subtropical Water (STW), Subantarctic Water (SAAW), Antarctic Intermediate Water (AAIW), Equatorial Subsurface Water (ESSW) and Pacific Deep Water (PDW) as defined in Table 1. Selected isopycnals are shown as dotted white/blue lines.

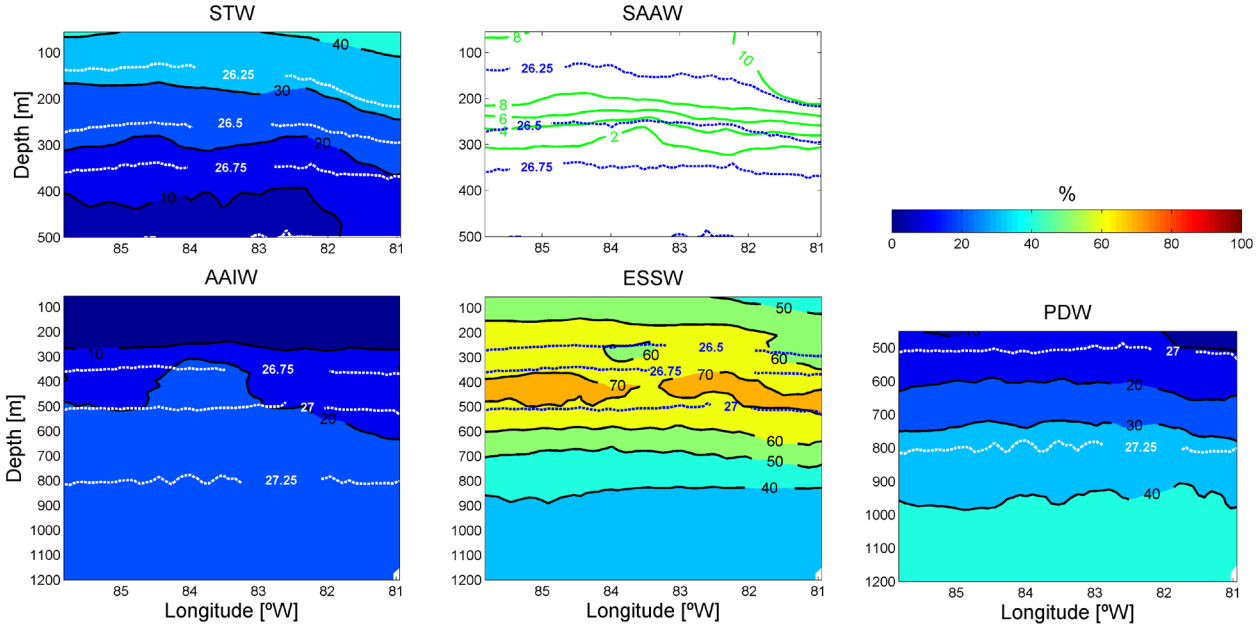

Figure 5. Water mass distribution (%) along the 3°35'S section between 85°50'W and the continental shelf for the M77 cruise (February 2009) for Subtropical Water (STW), Subantarctic Water (SAAW), Antarctic Intermediate Water (AAIW), Equatorial Subsurface Water (ESSW) and Pacific Deep Water (PDW) as defined in Table 1. Selected isopycnals are shown as dotted white/blue lines.

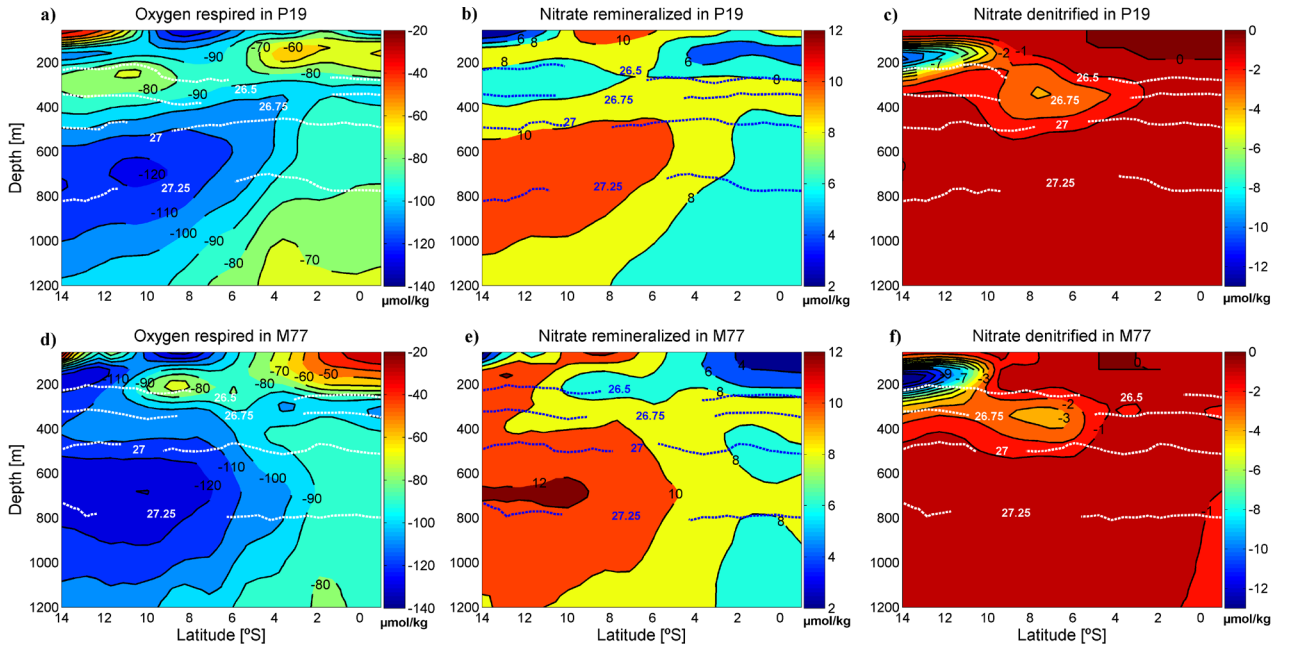

Figure 6A. OMP-derived biogeochemical activity within the water column for the P19 (March 1993) and M77 (February 2009) cruises: **(a)** oxygen respired (µmol/kg) in P19**, (b)** nitrate remineralized (µmol/kg) in P19, **(c)** nitrate denitrified (µmol/kg) in P19, **(d)** oxygen respired (µmol/kg) in M77, **(e)** nitrate remineralized (µmol/kg) in M77, **(f)** nitrate denitrified (µmol/kg) in M77. Selected isopycnals are shown as dotted white/blue lines.

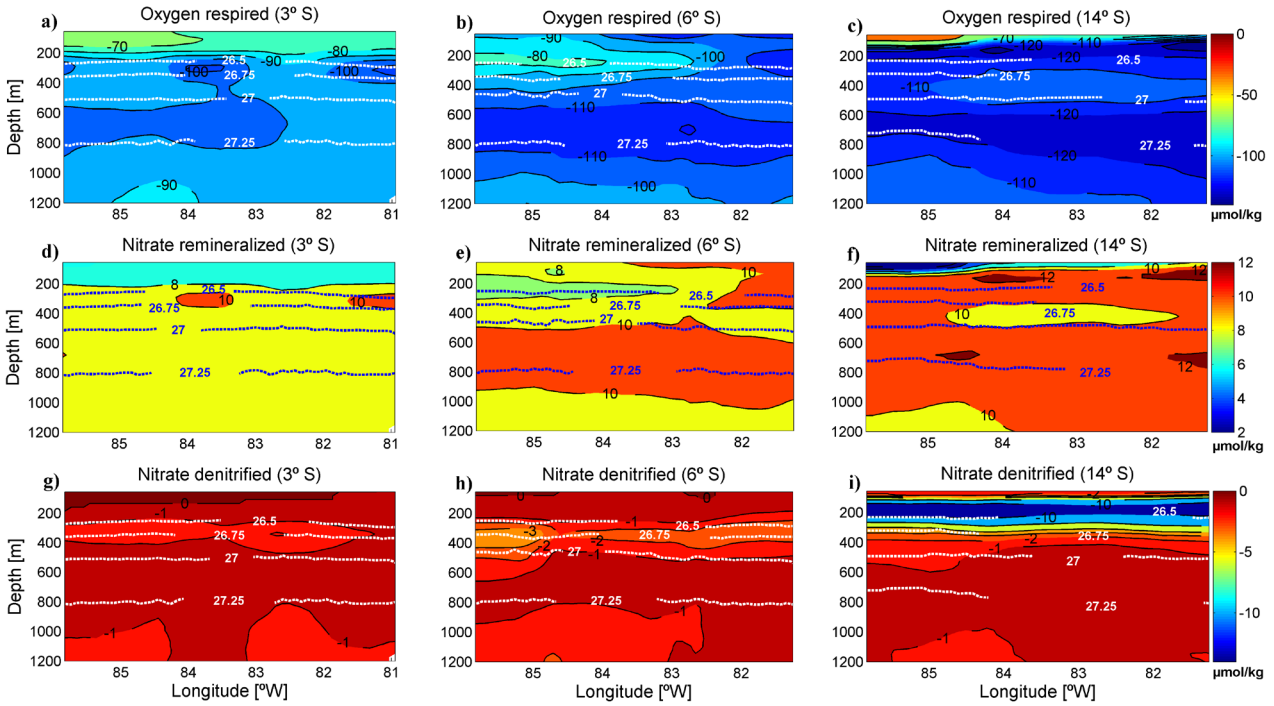

Figure 6B. OMP-derived biogeochemical activity within the water column for the 3 zonal sections (3ºS, 6ºS and 14ºS) completed during the M77 cruise (February 2009): **(a)** oxygen respired (µmol/kg) at 3ºS, **(b)** oxygen respired (µmol/kg) at 6ºS, **(c)** oxygen respired (µmol/kg) at 14ºS, **(d)** nitrate remineralized (µmol/kg) at 3ºS, **(e)** nitrate remineralized (µmol/kg) at 6ºS, **(f)** nitrate remineralized (µmol/kg) at 14ºS, **(g)** nitrate denitrified (µmol/kg) at 3ºS, **(h)** nitrate denitrified (µmol/kg) at 6ºS, **(i)** nitrate denitrified (µmol/kg) at 14ºS. Selected isopycnals are shown as dotted white/blue lines.

ESSW is the predominant water mass in the 150 to 500 m depth range (50-60%) for all zonal transects, with its core (70%) located near 400 m; this core is most developed at 3ºS (Figure 3), where it spans the whole longitudinal transect. The PDW becomes dominant (50%) only in the deepest levels (³1100 m) in the section at 6ºS.

3.3.2 Respiration and Denitrification

The extended OMP analysis provides a bulk estimate of nutrient enrichment, through the remineralization of organic matter, and oxygen depletion, through the accompanying respiration, assuming a Redfield stoichiometry. As some of the water masses used in the analysis are created by complex mixing processes rather than by air/sea interaction processes, the respective source water types do not always reflect surface ocean concentrations. This is most obvious in the oxygen concentrations of the source water types that are, except for STW and SAAW, far from saturation (Table 1, last column). As such, the amount of respired oxygen (Figures 6A, 6B) is to be seen relative to the source water type definitions. This is most prominent in the core of the OMZ were one would expect to find the amount of respired oxygen to be larger than 200 µmol/kg (if all contributing water masses were defined at the surface) but the method determines only 30 to 50 µmol/kg. However this is not a problem as the purpose of our study (and accordingly our interpretation) was on the regional remineralization /respiration/ denitrification and thus we do not attempt to over-interpret the data. Nevertheless, it makes clear that the OMZ is ventilated by water that is already rather low in oxygen concentrations so that even a moderate respiration can maintain the existence of the OMZ (Karstensen et al., 2008).

The patterns of remineralized nitrate and phosphate (phosphate not shown) closely follow the respired oxygen, with an inverse relation given by the Redfield ratios. Major deviations arise from the nitrate removal (and proportional phosphate enrichment, not shown) due to denitrification, also considered in the extended OMP analysis (Figures 6A, 6B). The denitrified nitrate estimated from the OMP analysis is different from the directly observed nitrite. The extended OMP analysis is able to detect the signature of denitrification that took place outside the studied region and was advected into this area. In general our method has similarities with the quasi-conservative tracer approach (*N**) developed by Gruber and Sarmiento (1997) but also considers the mixing of water masses when estimating the denitrification. For both cruises the largest signal for nitrate removal via denitrification is found between 10 and 14°S, at about 200 m depth (σ_θ<26.5) (Figure 6A), in agreement with previous studies (Lipschultz et al., 1990). However this core of denitrification is probably linked with the advection of waters from the Peruvian shelf, where we assume this nitrate deficit was originated (Figure 6B). This advection of shelf waters seems to have increased during 2009 (M77 cruise, Figure 6A), in good agreement with the expected reinforced Ekman transport due to stronger trade-winds during La Niña conditions. This near-surface denitrification core represents

an important source of nitrite for the anammox process, as confirmed by previous studies which found the highest rates of anammox in the upper part of the OMZ off Peru/Chile (Hamersley et al., 2007; Thamdrup et al., 2006). A second core with denitrification signal is found for both cruises between 2-4°S and 10°S in the depth range from 350 to 500 m (about $26.5 < \sigma_\theta < 27$) and in agreement with earlier interpretations (Tsuchiya and Talley, 1998).

3.3.3 Changes along 85º50' W between 1993 and 2009

Temporal changes in the spatial distribution of relevant biogeochemical parameters such as oxygen or nitrate may be caused by shifts in the water mass distribution (this includes changes in the advection, diffusion and isopycnal heave) and/or by changes in the biogeochemical activity (respiration and denitrification). Isopycnal heave may take place at very different temporal scales, from minutes (internal waves) and days/weeks (mesoscale phenomena) to interannual or interdecadal processes such as ENSO and PDO. In addition, there may be changes related to variations in the advection and mixing of the different water masses (e.g. Roemmich et al., 2007), the swifter the arrival of some specific water mass the greater its contribution and its influence on the local properties. Changes related to the variability of source water types, due to changes in air/sea interaction in the water mass formation at the source region (Bindoff and McDougall, 1994), cannot be directly considered by the OMP analysis although they may be reflected by changes in the water mass distribution.

Our aim here is to discern between the physical and biogeochemical components of the observed changes in oxygen and nitrate. The M77 versus P19 changes, either in the measured biogeochemical parameters or in OMP-derived water mass distribution and biogeochemical activity, are calculated by subtracting the 1993 value from the 2009 value at each gridpoint (M77-P19).

3.3.3.1 Measured changes in oxygen and nitrate content

The meridional sections of measured nitrate and dissolved oxygen during P19 and M77 cruises are shown in Figure 7 and their changes in time are depicted in Figure 8. In the top few hundred meters (Figure 8) there are a few locations possibly influenced by the surface and near-surface zonal currents. First, there is a decrease in dissolved oxygen (between -10 and -20 μmol/kg) and an increase in nitrate (between 1 and 4 μmol/kg) in the 55-250 m depth range at the equator (Figure 8). This corresponds to the location of the relatively oxygen-rich and nutrient-poor eastward flowing EUC. The weakening of the EUC (Czeschel et al., 2012) may explain the decrease in oxygen (and the increase in nitrate) found at this location, although it is not possible to discern how much of this weakening is caused by the seasonal variability (Johnson et al., 2002) and how much is due to La Niña conditions found in 2009. Second, there are two cores with oxygen increase at 8ºS, a shallow one centred at 50 m, with an increase between 10 and 25 μmol/kg, and a deep one centred at 225 m, with an increase of 10

µmol/kg (Figure 8a). These cores may possibly be associated with the oxygen-rich eastward flowing Southern Subsurface Counter Current (SSCC) (Czeschel et al., 2011); however, both cores must have different origin, as the shallow core displays a reduction in the nitrate content whereas the nitrate concentration of the deep core has increased (Figure 8b). Third, between 11 and 9.5ºS and in the 50-150 m depth range, we observe a core that has undergone an increase in nitrate (between 4 and 10 µmol/kg) and a decrease in oxygen (between -20 and -50 µmol/kg) (Figure 8). The same behaviour is found in another core located in the upper 250 m at 4ºS. We identify the former core with the westward flowing South Equatorial Current (SEC) and the core at 4ºS with the southern equatorial branch of the SEC (Czeschel et al., 2011). It is possible that wind-driven changes in the SEC (with stronger south-easterlies during the 2009 La Niña) may have caused the variations observed in oxygen and nitrate by strengthening these currents.

At 1ºN and between 400 and 600 m, there is a core with nitrate reduction (-1 µmol/kg) and slight oxygen increase (5 µmol/kg) (Figure 8), possibly associated to an increase in the transport of the eastward flowing North Intermediate CounterCurrent (NICC) (Czeschel et al., 2011). Between 3 and 5ºS and in the depth range from 500 to 1000 m, we find oxygen depletion (between -5 and -10 µmol/kg) and nitrate increase (between 1 and 2 µmol/kg, down to 1200 m) (Figure 8). These changes may be related to a decrease in the westward flowing South Equatorial Intermediate Current (SEIC) (Czeschel et al., 2012), therefore enhancing the presence of ESSW at this location (Figure 9).

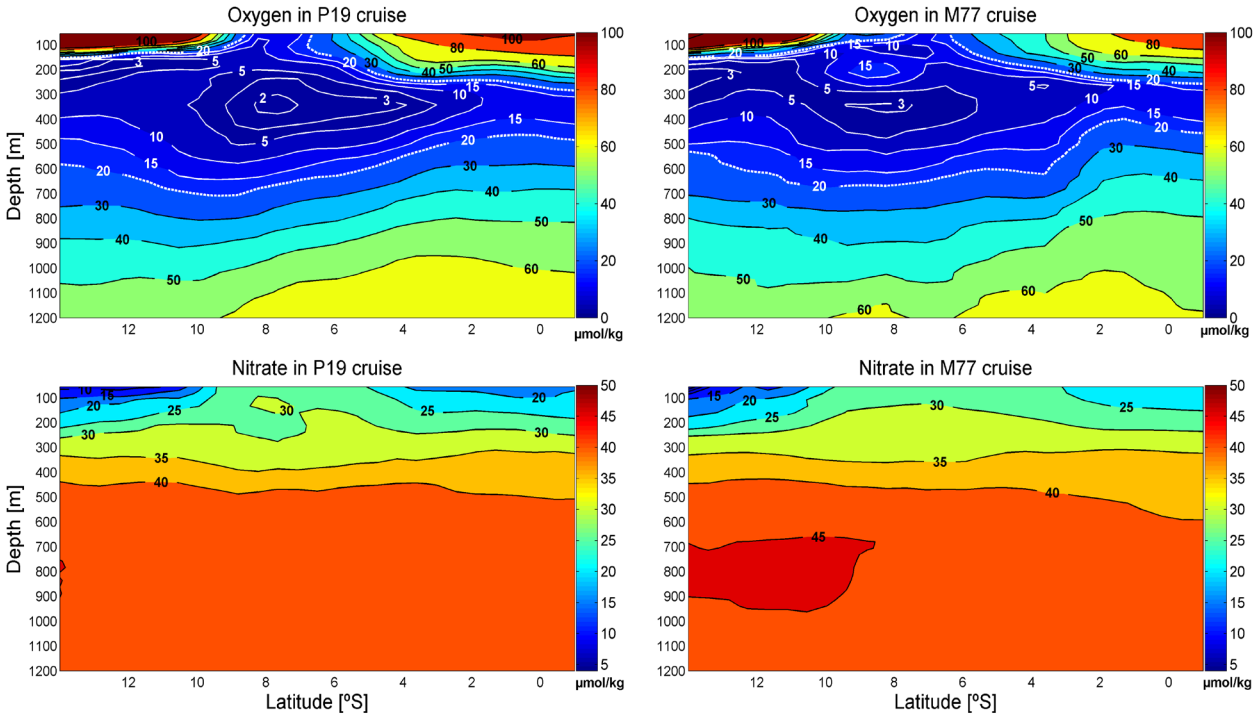

Figure 7. Meridional section with measured oxygen (µmol/kg) and nitrate (µmol/kg) for the P19 (March 1993) and the M77 (February 2009) cruises.

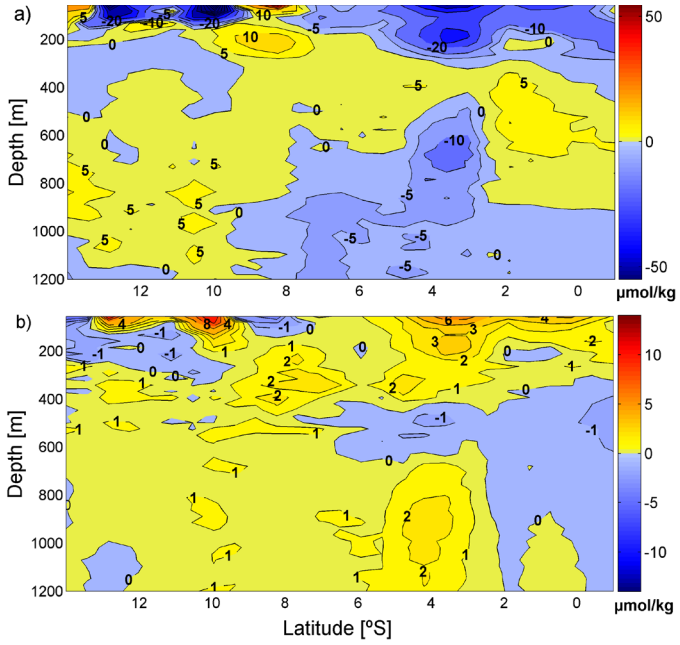

Figure 8. Measured **(a)** oxygen (µmol/kg) and **(b)** nitrate (µmol/kg) changes between March 1993 and February 2009 (M77-P19).

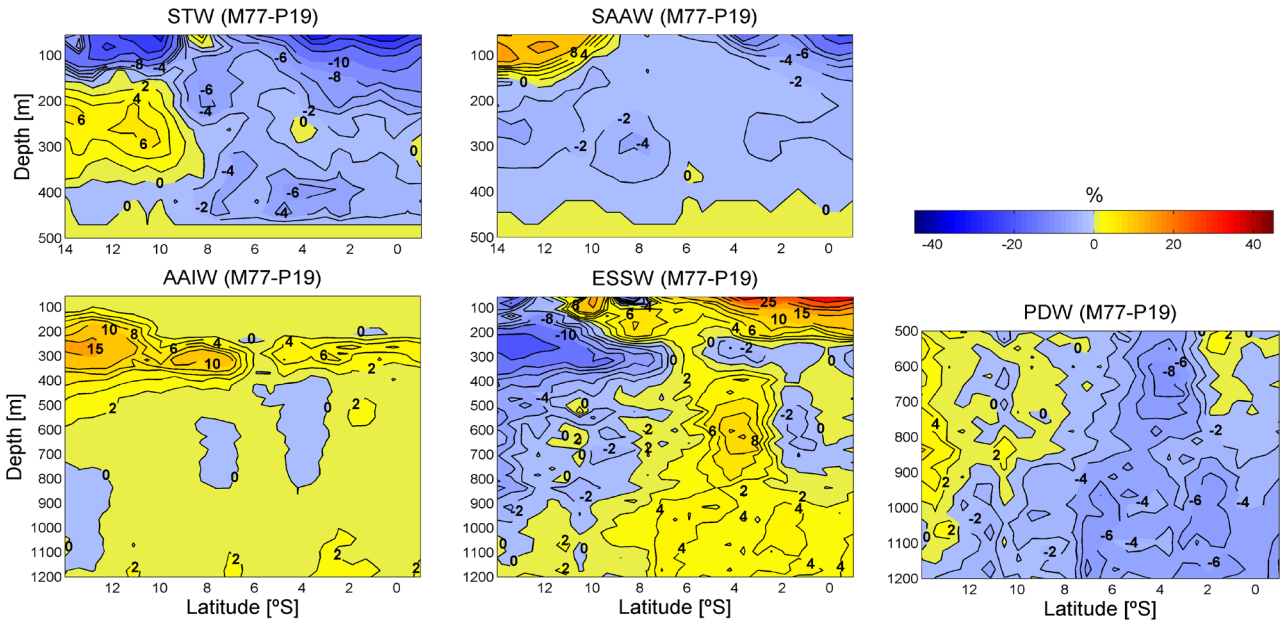

Figure 9A. Water mass changes (%) between March 1993 and February 2009 (M77-P19) for Subtropical Water (STW), Subantarctic Water (SAAW), Antarctic Intermediate Water (AAIW), Equatorial Subsurface Water (ESSW) and Pacific Deep Water (PDW).

3.3.3.2 Changes in water mass distribution

In the near surface layers (between 55 and 200m) south of 10ºS, there is a substantial increase in SAAW at the expense of STW (Figure 9A). The apparent decrease of SAAW in the northern end of this section actually represents a decrease in the equatorial surface waters found south of the Equator during the 2009 La Niña conditions (see Section 3.3.1). The increase in precipitation in the

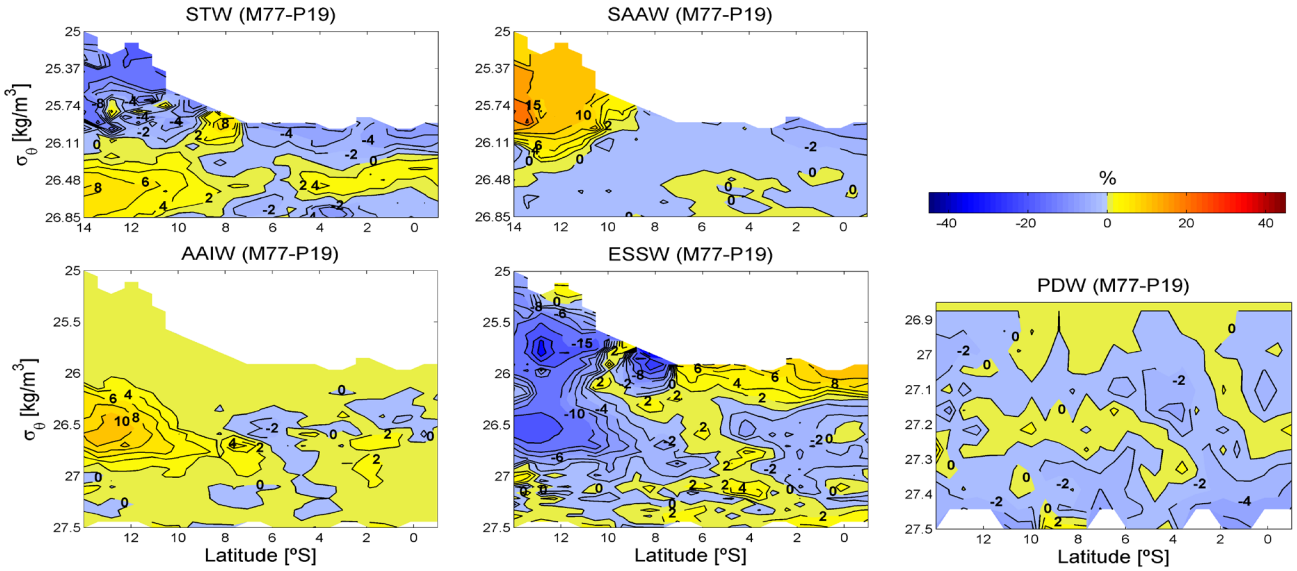

Figure 9B. Water mass changes (%) in density space between March 1993 and February 2009 (M77-P19) for Subtropical Water (STW), Subantarctic Water (SAAW), Antarctic Intermediate Water (AAIW), Equatorial Subsurface Water (ESSW) and Pacific Deep Water (PDW).

eastern equatorial Pacific during El Niño conditions could explain the larger content in equatorial surface water found in the 1993 data.

In the upper thermocline and upper intermediate waters the dominant spatial trend is caused by two different phenomena: First, the upwelling/downwelling of ESSW associated to La Niña/El Niño conditions respectively. Second, during 2009 the core of AAIW appears to flow along shallower isopycnals (Figures 9B, 2A and 2B).

The ESSW decreases in the water column (south of 8ºS) between 150 and 600 m, partially replaced by STW which increases between 200 and 300 m (from 8ºS to 2ºS) and largely replaced by the upper part of AAIW (Figure 9A). The upward expansion of AAIW also reaches down to its core (25% contribution), centred around 700 m (Figures 2A, 2B).

In order to discern which changes are due to the isopycnal heave associated to ENSO and which ones might be due to other causes, we have repeated the analysis on density space. In Figure 9B we can still appreciate the tongue of increasing AAIW (Figure 9A) flowing along shallower isopycnals, which is in good agreement with the trends of warming and density reductions of the core of AAIW found by Schmidtko and Johnson (2012) in the eastern south Pacific. This tongue of shallower AAIW replaces ESSW and then advects more oxygenated waters into a different OMZ depth range (between 150-500 m) as it flows northward.

In the lower intermediate waters (450 to 800 m) there is an alternation in the predominance of ESSW and PDW, with greater presence of PDW/ESSW at latitudes south/north of

8ºS during the M77 cruise in 2009. The increase of ESSW appears centred between 5ºS and 3ºS, at the location of the westward flowing SEIC (Czeschel et al., 2012). The enhanced presence of PDW south of 8ºS (Figure 9A) does not appear to be directly linked to the ENSO phenomenon; rather it may possibly reflect the decadal shift of phase in the PDO, from the 1993 warm El Viejo to the 2009 relatively cold La Vieja. However, the mixing fraction of PDW does not increase along the whole section (800-1200 m depth range) as expected during La Vieja phase, perhaps related to a weakening of the SEIC. Nevertheless, the sensitivity tests grant us confidence on the robustness of this result (see supplementary material), further discussion remains beyond the scope of this paper.

3.3.3.3 Physical and biogeochemical contributions to oxygen and nitrate changes

By means of the extended OMP analysis, we may assess how much of the observed changes are related to variations in the water mass distribution (physical component which includes advection, diffusion and isopycnal heave) and how much is caused by changes in the respiration and denitrification signals (biogeochemical component). These biogeochemical changes should not be interpreted as variations in the biogeochemical rates, as calculating a rate requires knowing not only the characteristics of water masses at origin but also an estimate of their age as they reach the studied area. Hereafter, we will refer to the physical component of change as 'physical transport'.

As each parameter (oxygen, nitrate) is bound to a residual (difference between the measured data and the OMP modelled data), the exact contribution of each component of change remains unknown but yet we may find out the significance of the physical and biogeochemical components.

The physical and biogeochemical contributions to the oxygen and nitrate changes between both cruises are shown in Figure 10. The same analysis was done in density space with similar results (see the supplementary material). The white-shaded areas represent the points where the total error, or difference between the measured parameter change and the OMP-modelled parameter change (physical plus biogeochemical), is larger than either modelled component of change, i.e. outside the white-shaded areas the signal is larger than the noise so the information provided is significant. Notice that this is the most restrictive scenario as we are assuming that all the error in the OMP fit is associated to only one component of the modelled change.

Within the OMZ waters, an increase/decrease of oxygen due to larger physical transport will naturally lead to more/less oxygen availability and increased/decreased respiration and nutrient remineralization. South of 6ºS, a significant increase in the physical transport of oxygen is observed between 150 and 400 m (Figure 10a), in good agreement with the previously proposed upward shift in the OMZ depth range ventilated by AAIW. This gain in oxygen is partially compensated by an increase in the respiration signal as more oxygen becomes available in this depth range of the

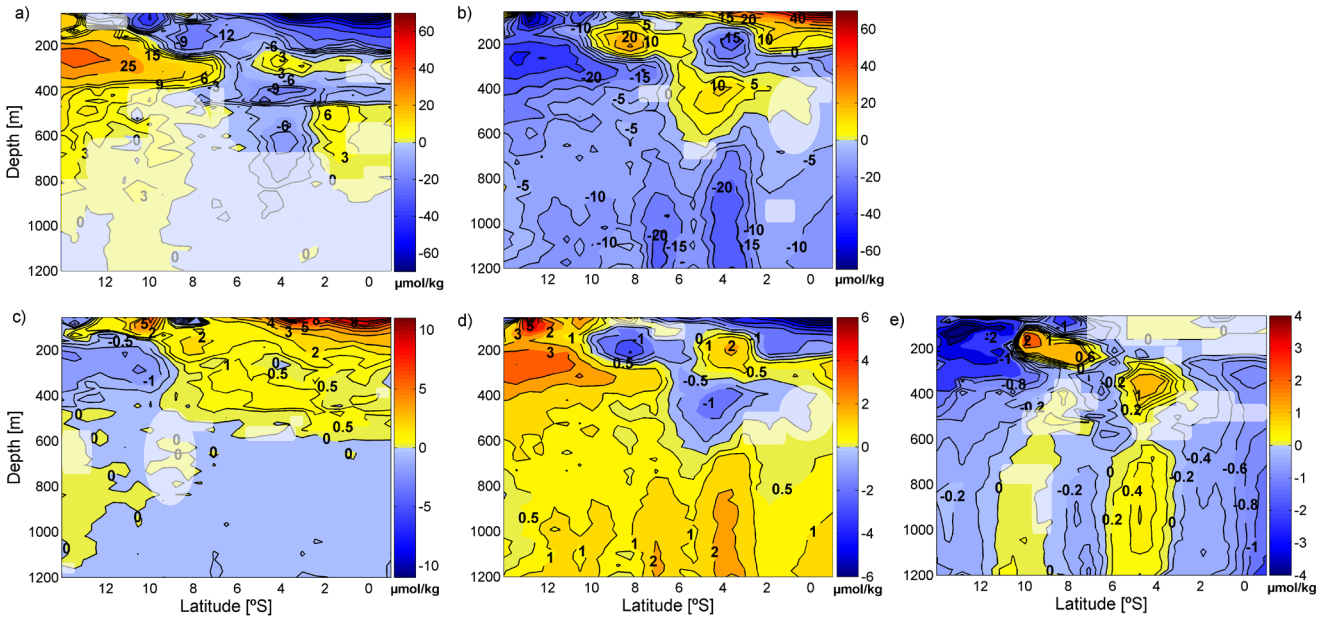

Figure 10. OMP derived changes in: (a) physical transport of oxygen (µmol/kg), (b) oxygen respired (µmol/kg), (c) physical transport of nitrate (µmol/kg), (d) remineralized nitrate (µmol/kg), (e) denitrified nitrate (µmol/kg). White shading represent areas where the difference between the measured change and the OMP modelled change is larger than each component of the change (physical or biogeochemical).

OMZ (reflected as an apparent oxygen loss in Figure 10b). The outcome is a net change in oxygen of smaller amplitude (Figure 8a). In the upper 150-200 m (north of 8ºS) this situation is reversed, as there is a general decrease in the physical transport of oxygen (Figure 10a) and an increase in the physical transport of nitrate (Figure 10c) which is accompanied by a reduction in the oxygen available for respiration (reflected as an apparent oxygen gain in Figure 10b) and, consequently, a reduction in the nitrate remineralized in the same locations (Figure 10d). These results agree with a previous interpretation that pointed to an "oxygen-driven" remineralization intensity within the Chilean OMZ (Paulmier et al., 2006). These changes may be explained by the shift from the 1993 El Niño to the 2009 La Niña conditions, which promoted an upward displacement of the oxygen-poor and nutrient-rich ESSW.

The amount of nitrate loss due to denitrification is directly influenced by changes in oxygen availability, which ultimately depends on the interplay between oxygen supply and respiration rate. As also shown by our data, an increase in dissolved oxygen in the upper part of the water column takes place during El Niño conditions (Guillén et al., 1988), accompanied by a deepening of the upper part of the OMZ which dampens denitrification in the upper layers (Morales et al., 1999). During La Niña events the situation reverses, the reinforced upwelling promotes the rise in depth of the upper part of the OMZ, enhancing denitrification in the upper part of the water column (Morales et al., 1999). Therefore, the change of ENSO phase between both cruises may explain the increased nitrate loss observed between 1993 and 2009 in the upper 200 m south of 10ºS (Figures 6A, 6B and 10e).

This increased signal of denitrification is most likely the result of increased advection of waters from the Peruvian shelf, where denitrification occurred during La Niña conditions (Figure 6B).

Further deep, between 250 and 500 m, the decrease of the volume delimited by the 1 µmol/kg nitrate-loss isoline in 2009 (Figure 6A) represents a decrease in the denitrification signal and is corresponded by a core with apparent nitrate gain located between 11º and 7ºS in the 100-300 m depth range (Figure 10e). However, inside the core of this volume we find a more intense denitrification signal (~3 µmol/kg) in 2009 (Figure 6A), associated to a slightly larger nitrate loss between 300 and 400 m from 8 to 6ºS (Figure 10e).

A decrease in the denitrification signal (and consequently an apparent nitrate gain) is also observed roughly between 11-8ºS and 6-4ºS, from 600 to 1200 m (Figure 10e). In contrast, below 600 m and away from these latitudinal bands, there is slightly more nitrate loss in 2009, located mainly north of 3ºS and south of 11ºS (Figure 10e).

Changes in the intensity of the zonal currents of the Equatorial Current System, already discussed in the Section 3.3.3.1, may also be appreciated at their specific locations when discerning between physical and biogeochemical forcings. In general, an increase in the intensity of an eastward flowing current (or a weakening in a westward current) will be shown by a gain of physically supplied oxygen, a larger respiration and a decrease in the nitrate loss by denitrification (or decrease in the denitrification signal). The situation is the opposite with a weakening of an eastward (or strengthening of a westward) current.

3.4 Conclusions

In this paper we have examined the changes in the water mass structure and biogeochemical signals between two opposite phases of ENSO in the eastern tropical South Pacific. The observed changes in the upper 200 m north of 10ºS are clearly influenced by the ENSO phenomenon. During the 1993 El Niño event, there was increased advection of relatively well oxygenated STW from the west of the equatorial Pacific Basin which replaced the low-oxygen ESSW in the top 250 m of the water column. This input deepened the upper part of the OMZ, dampening denitrification in the upper layers. In addition, the northward advance of the Shallow Salinity Minimum originated by subducted SAAW was reduced. In contrast, during the 2009 La Niña conditions, the reinforced trade winds drove enhanced upwelling, raising the upper part of the OMZ. The nutrient-rich and oxygen-poor ESSW replaced STW in the upper layers north of 10ºS, inducing a reduction in the amount of oxygen available for respiration and increasing the nitrate loss by denitrification.

The heaving of isopycnals associated to ENSO partially explains the remarkable shoaling and upward expansion of the upper part of AAIW observed in the southern part of the section, with

AAIW replacing ESSW between 150 and 500 m. This fact brought a large increase in advected oxygen to this depth range of the OMZ during 2009, which led to a larger consumption of oxygen through an increased respiration and to a larger production of remineralized nitrate. Therefore, at an interannual time scale, the upward movement of isopycnals associated to La Niña conditions favours the ventilation of the OMZ by AAIW.

We have shown that the shoaling of AAIW is also partially explained by the fact that AAIW flows along shallower isopycnals in 2009. This is in good agreement with the long-term trend of shoaling and density reductions of the core of AAIW as found by Schmidtko and Johnson (2012) south of 15ºS in the eastern South Pacific. At an interdecadal time scale, such changes in the pattern of advection of AAIW may mitigate the long term trend of expanding OMZs found in the world oceans (Stramma et al., 2008), possibly explaining why an increase in oxygen content has been reported for some areas of the subtropical gyres, e.g. off Chile between 200 and 700 m (see Figure 2d of Stramma et al., 2010b). However, the temporal resolution of our data set prevents us to test this hypothesis.

Besides the general changes described above, we observe a few cores along the latitudinal section in which oxygen and nitrate change in a distinct way. These cores are related with changes in the intensity of the zonal currents of the Equatorial Current System. The eastward flowing currents ventilate the OMZ as they supply waters with relatively higher content in oxygen whereas the westward flowing currents transport waters almost depleted of oxygen from the OMZ. Therefore, a weakening in an eastward (or the strengthening of a westward) current enhances the presence of ESSW and brings about a decrease/increase in advected oxygen/nitrate; this leads to a decrease in the respired oxygen and in the nitrate remineralized and may induce further nitrate loss by denitrification. The situation reverses with a strengthening of the eastward or weakening of the westward currents.

Acknowledgements

We are very grateful to the anonymous reviewers who provided constructive and useful comments which certainly helped to improve this manuscript. P.J.L. was supported through a JAE grant from Consejo Superior de Investigaciones Científicas and the European Social Fund. Financial support was received through Laboratorio Internacional de Cambio Global CSIC/PUC (P.J.L. and J.L.P.), project TIC-MOC (CTM2011-28867) funded by the Spanish Ministerio de Ciencia e Innovación (P.J.L and J.L.P.), GEOMAR Helmholtz Centre for Ocean Research Kiel (J.K. and L.S.) and the DFG-supported project SFB 754 (www.sfb754.de) (J.K. and L.S.).

3.5 Supplementary material

1) Residuals in mass conservation and robustness of the results.

After running the extended OMP analysis, we only select for our study those points with mass residuals below 4%. It's worthy to remark that the vast majority of the data points present mass residuals considerably below this 4% limit; therefore, the water mass changes described are reliable. In Figure S1 we show the residuals associated to mass conservation in those points selected for our analysis, along both latitude and depth.

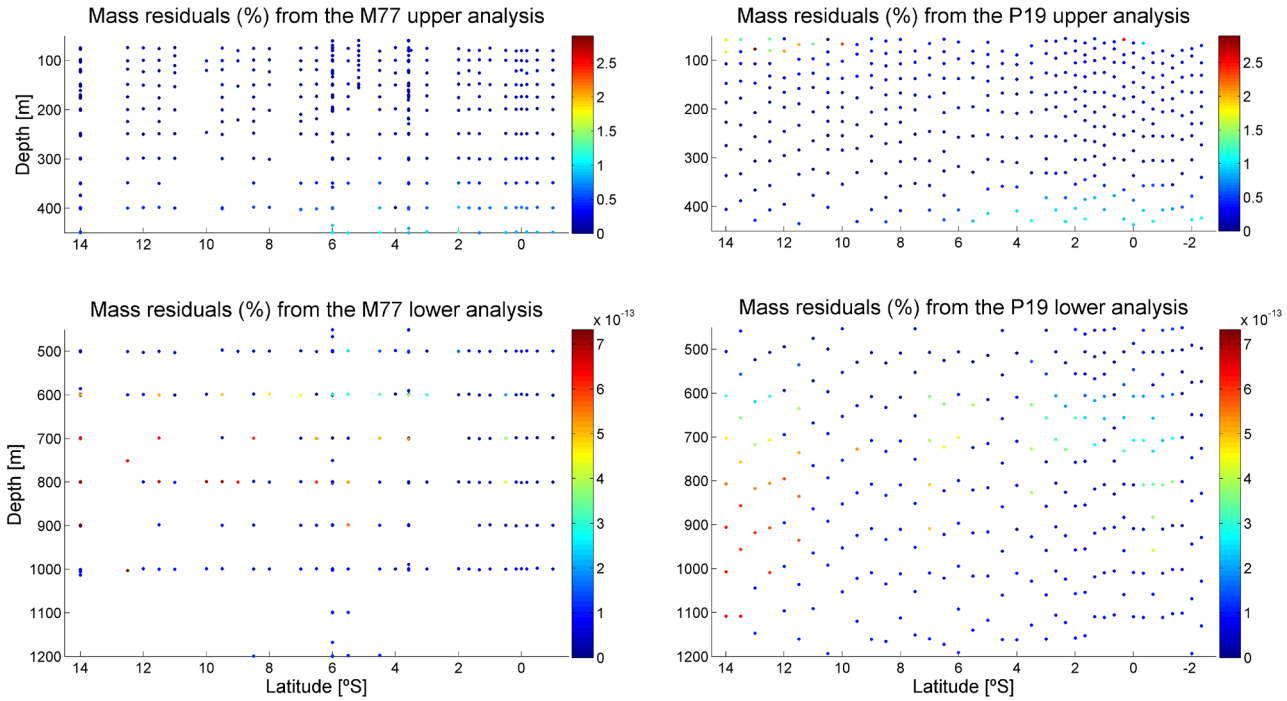

Figure S1. Distribution of the mass conservation residuals (%) for each extended OMP analysis.

2) Assessment of the uncertainty in the water mass mixing fractions as obtained after considering (a) spatial variations in end member properties (natural variability) and (b) temporal variations in end member properties (temporal variability).

We have run a series of sensitivity tests by perturbing simultaneously all water types (end-members) in the source water-mass matrix with a Gaussian noise through a series of Monte Carlo experiments. We have examined what is the influence on the resulting water-mixing fractions.

For the first series of sensitivity tests, we consider the influence of natural variability of each parameter in the source regions where the water types were defined. For this purpose we have calculated the standard error associated to each parameter by averaging the standard errors obtained for such parameter

in each source region. These standard errors are then multiplied by the Gaussian noise and the result is added to the corresponding original water type in the source water-mass matrix and then the OMP is solved.

The influence of possible temporal changes of seawater properties in the source regions is considered in a second series of sensitivity tests. We have used the (largest) temporal trends of potential temperature (0.02 ºC/year) and salinity (-0.0005 psu/year) found in the AAIW formation region, in the eastern South Pacific (Schmidtko and Johnson, 2012), to estimate a standard error for the temporal variability of these parameters from 1993 to 2009. We could not find in the literature temporal trends in potential temperature or salinity in the source regions of the remaining water masses so we decided to use the AAIW salinity and potential temperature standard errors for all water masses. We are aware that the AAIW standard errors will probably represent overestimates for the remaining water masses (mainly for ESSW and PDW as they are defined below the sea surface). Therefore, all the results from these sensitivity tests (except for AAIW) must be understood as a 'worst case' scenario, mainly for ESSW and PDW. For all other parameters (nutrients and oxygen) we have used the same standard errors as calculated from the natural variability analysis.

All the above sensitivity tests are run for the upper and lower portions of the P19 and M77 datasets separately. The mixing fractions, obtained for all data points after each perturbed run, are used to obtain average standard errors. Finally, a global-weighted mean standard error is obtained for each water mass mixing fraction (Table S1); the weighting applied takes into consideration the number of data points in each subsection analysed with the OMP method.

The global mean standard errors are quite low for AAIW (<3%) under conditions of both natural and temporal variability. This low variability gives us confidence in the results obtained and discussed in this paper. The worst results correspond to ESSW (9%) and PDW (5%). In the case of natural variability this is probably due to the fact that we use the averaged standard error (from all source

Table S1. Mean standard errors in the water-mass mixing fractions as obtained with the extended OMP analysis after running the sensitivity tests through a series of Monte Carlo simulations.

Mean standard error (%)	AAIW	ESSW	STW	SAAW	PDW
Natural variability	2.95	9.11	5.32	4.21	7.89
Temporal variability	2.42	7.64	5.08	5.25	4.45

regions) to characterize the natural variability of each parameter, despite the standard errors in potential temperature and salinity for ESSW and PDW are one or two orders of magnitude smaller than those of the remaining water masses (which were defined at the sea surface). In the case of temporal variability, these relatively large values are related to the fact that we use standard errors that overestimate the temporal change of potential temperature and salinity for these water masses (as explained above).

3) Computation of the best fit between silicate and phosphate (ΔSiO_4:ΔPO_4 ratio).

The ratio ΔSiO_4:ΔPO_4 is affected by the dissolution of opaline silica (Hupe and Karstensen, 2000) and shows regional variations depending on the plankton composition (Poole and Tomczak, 1999). In order to tackle this issue we calculated, for each dataset separately and for both datasets together, the best linear fit (SiO_4 = ratio x PO_4) for the P19 and 774 datasets by means of a linear regression analysis. We then compared the mass residuals produced by the OMP for the different ΔSiO_4:ΔPO_4 ratios.

In Table S2 we compare the goodness of the fit (R^2) and the quality of the OMP solution (mean mass residual in %) for the 40:1 silicate to phosphate ratio (used previously in Llanillo et al., 2012), and for the optimal ΔSiO_4:ΔPO_4 ratios derived from each individual dataset and for both datasets together. We may clearly see that the 40:1 silicate to phosphate ratio produces the worst fit.

According to the info summarized in Table S2, we have selected the ratios (ΔSiO_4:ΔPO_4) obtained for the P19 and M77 datasets (18.37 and 14.45 respectively) because they produce the smallest mean mass conservation residuals while explaining the largest data variability (R^2).

Table S2. Comparison of the goodness of the fit (R2) for different linear models between silicate and phosphate, as obtained for different subsets of data points (P19, M77 or both datasets together). The quality of the OMP solution (mean and standard deviation mass residuals in %) is also shown.

Ratio		**R^2**	**Mean mass residual (%)**		**Std mass residual (%)**	
Both	40:1	-	**P19**	0.4993	**P19**	0.2977
			M77	0.6273	**M77**	0.5862
Both	16.61:1	0.4218	**P19**	0.1397	**P19**	0.2977
			M77	0.1184	**M77**	0.1920
M177	14.45:1	0.5741	0.0992		0.1947	
P19	18.37:1	0.5707	0.1233		0.3060	

4) Analysis in density space.

We have done an analysis on density space in order to discern the influence of isopycnal heave on the changes described in the paper. Water mass changes in density space are shown in the revised manuscript. Here we show the OMP derived changed in physical transport of oxygen,

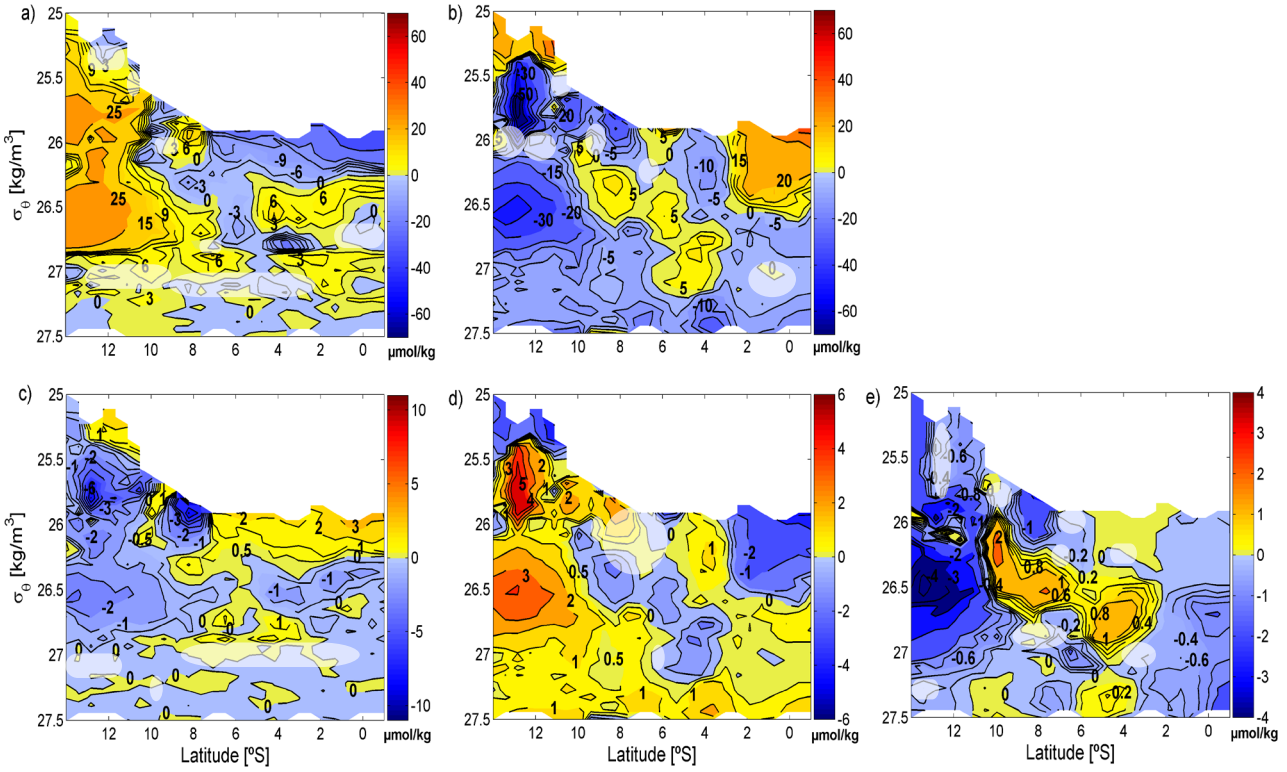

Fig. S2. OMP derived changes in density space between March 1993 and February 2009 (M77-P19): **(a)** physical transport of oxygen (µmol/kg), **(b)** respired oxygen (µmol/kg), **(c)** physical transport of nitrate (µmol/kg), **(d)** remineralized nitrate (µmol/kg) and **(e)** denitrified nitrate (µmol/kg).

CHAPTER

4

Oxygen supply pathways and closed oxygen budget for the Eastern South Pacific Oxygen Minimum Zone

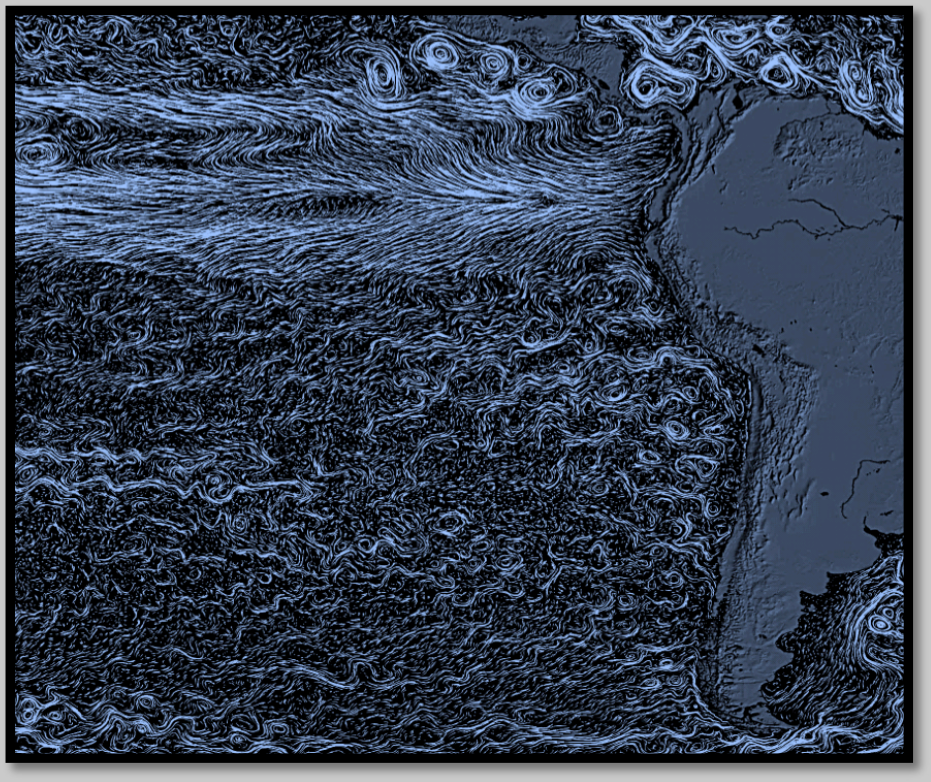

Llanillo, P.J., Pelegrí, J.L, Talley, L.D., and Peña-Izquierdo, J.: Oxygen supply pathways and closed oxygen budget for the Eastern South Pacific Oxygen Minimum Zone. In preparation.

"Aristotle taught me to fix my judgement on that which is grounded upon reason, and not on the bare authority of the master"
Galileo Galilei

Abstract

The global picture of oxygen supply into the eastern South Pacific (ESP) oxygen minimum zone (OMZ) is investigated with the help of climatological Argo and dissolved oxygen data. Annual mean oxygen fluxes due to epineutral advection, epineutral diffusion and dianeutral diffusion are computed for the whole ESP and their relevance for the oxygen supply into the ESP OMZ is assessed. Two main routes are found for the advective supply of oxygen, the traditional equatorial pathway and the inedit subtropical pathway. The subtropical pathway has not been examined before although it represents ~45% of the advective oxygen supply at the core of the ESP OMZ (γ_n = 26.81 kg m^{-3}) and provides more net oxygen gain (~8.8 kmol s^{-1}) than the equatorial pathway (~3.6 kmol s^{-1}) at this neutral surface layer. This finding challenges the common assumption that the ESP OMZ is only ventilated by the eastward flowing currents of the Equatorial Current System. A new zonal current flowing eastward all the way into the ESP OMZ between 12-15ºS with its core at γ_n = 27.1 kg m^{-3} has been described and its oxygen supply has been quantified as the 18% of the (advective) equatorial oxygen supply between γ_n = 27 kg m^{-3} and γ_n = 27.4 kg m^{-3}. By integrating the computed oxygen fluxes into the whole volume of the ESP OMZ, the annual mean oxygen budget is revealed. Epineutral turbulent diffusion provides a net oxygen supply of 417.4 ± 43.0 kmol s^{-1} (~2.15 µmol kg^{-1}), advection supplies 292.7 ± 25.2 kmol s^{-1} (~1.49 µmol kg^{-1}) and dianeutral turbulent diffusion provides 85.8 ± 17.6 kmol s^{-1} (~0.43 µmol kg^{-1}). The mean biological consumption of oxygen required to close the budget is 795.9 ± 195.0 kmol s^{-1} (4.07 µmol kg^{-1}).

Chapter 4

4.1 Introduction

The eastern South Pacific (ESP) oxygen minimum zone (OMZ) is a large oceanic volume characterized by low dissolved oxygen levels (Figure 1a). The ESP OMZ extends approximately between 100 and 900 m depth (Karstensen et al., 2008), covering about 19% of the total area occupied by permanent OMZs (Paulmier and Ruiz-Pino, 2009). Its westward extension and depth range decrease poleward from the equator (Stramma et al., 2010a).

The ESP OMZ is located off-shore Equator, Peru and Chile and equatorward of the South Pacific subtropical gyre, in an oceanic region with sluggish circulation known as the 'shadow zone' (Reid, 1965). The shadow zone is situated away from the main streamlines of the wind-driven subtropical gyre, responsible for most of the ventilation of the thermocline (Luyten et al., 1983). This low ventilation rate combines with the large subsurface biological consumption of oxygen, typical of eastern boundary upwelling systems (Helly and Levin, 2004; Paulmier et al., 2006), to explain the existence of the ESP OMZ.

Currently, there is no consensus upon what is the oxygen concentration isoline delimiting the boundary of an OMZ (Paulmier and Ruiz-Pino, 2009). In this study we will set an oxygen concentration threshold of 60 μmol kg^{-1} as the ESP OMZ boundary. We select this OMZ boundary because many fish species are disturbed or die with oxygen concentrations going below the range 60-120 μmol kg^{-1} (Stramma et al., 2010a). Furthermore, following Paulmier and Ruiz-Pino (2009), we define the core of the ESP OMZ as the volume where oxygen levels fall below the suboxic upper threshold of 20 μM (~19.5 μmol kg^{-1}). Below this threshold, nitrate (NO_3) starts to be used instead of oxygen for the respiration of the organic matter (Smethie, 1987; Oguz et al., 2000). The core of the ESP OMZ is located at ~ 350 m (γ_n= 26.81 kg m^{-3}) at 7.5ºS, with a maximum thickness of ~400 m east of 90ºW (Figure 1b).

The ESP OMZ plays an important role in the carbon and nitrogen cycles (Bange et al., 2005). Within its suboxic core the oceanic-fixed nitrogen is reduced and released to the atmosphere in the form of nitrous oxide (N_2O), a powerful greenhouse gas (GHG) and gaseous dinitrogen (N_2) (Morales et al., 1999; Codispoti et al., 2001; Kalvelage et al., 2011). Due to this loss to the atmosphere, nitrogen becomes a limiting nutrient for primary production once these waters upwell to the photic zone, weakening the biological carbon pump (Kalvelage et al., 2011).

Observations suggest that oxygen concentrations are decreasing in the tropical oceans (Stramma et al., 2008; Stramma et al., 2010b), probably as a result of both man-made global warming and natural decadal variability (Deutsch et al., 2011). According to modeling studies, OMZs are expected to expand under global warming conditions (Matear and Hirst, 2003; Schmittner et al., 2008). This may reduce the habitat and threaten the sustainability of the important pelagic fishery

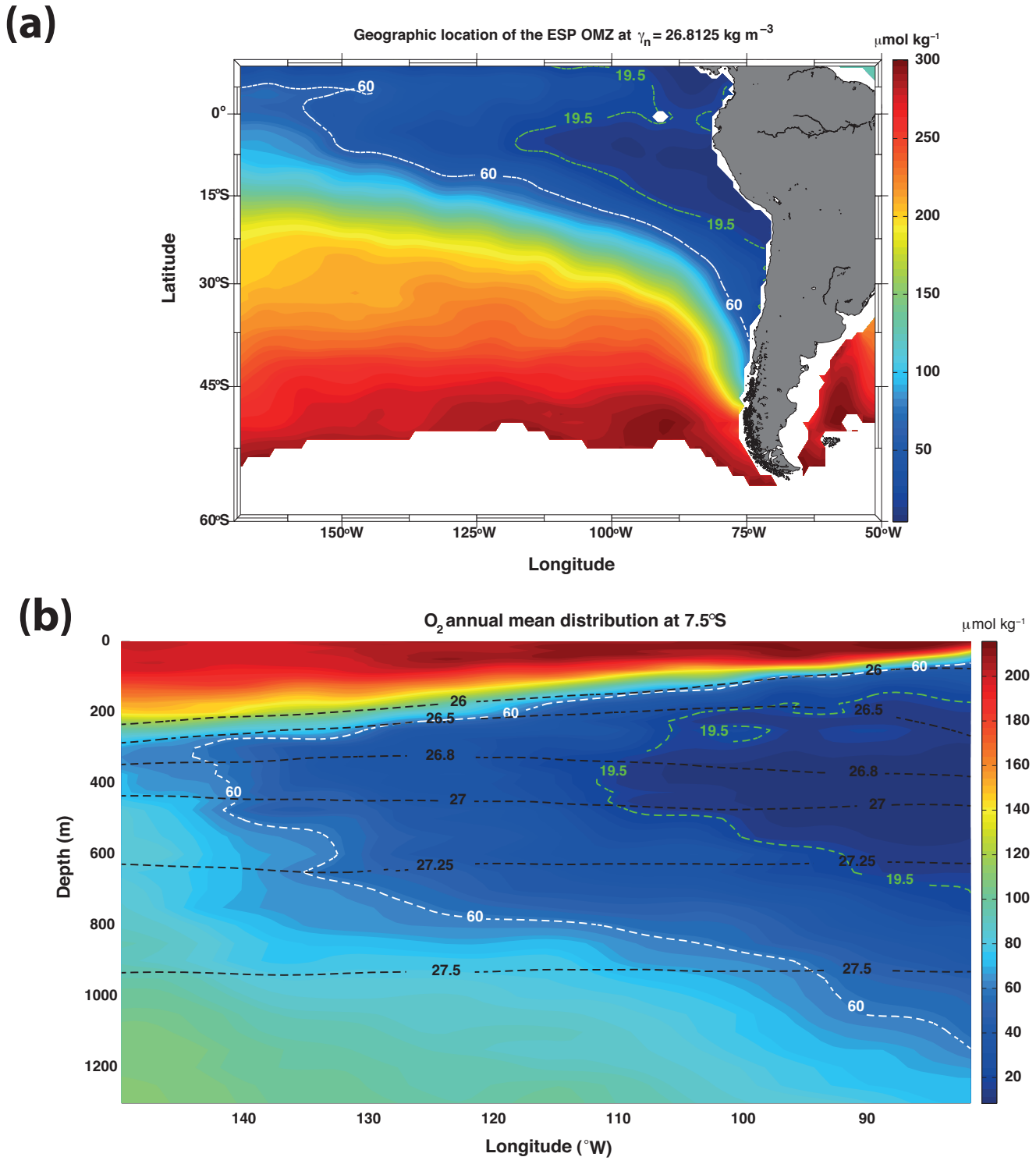

Fig.1 a) Map of the study area with the ESP OMZ delimited by the contour of 60 µmol kg^{-1} (white dashed line) and its core delimited by the contour of 19.5 µmol kg^{-1} (green dashed line). The background shows the climatological mean of dissolved oxygen (µmol kg^{-1}) at the neutral surface of the ESP OMZ core (γ_n = 26.81 kg m^{-3}, ~350 m). **b)** Vertical section of the climatological mean of dissolved oxygen (µmol kg^{-1}) at 7.5ºS with the ESP OMZ delimited by the contour of 60 µmol kg^{-1} (white dashed line) and its core delimited by the contour of 19.5 µmol kg^{-1} (green dashed line). Neutral density contours are included for reference (black dashed line).

maintained by the high biological productivity overlying the ESP OMZ (Strub et al., 1998), and may also promote a larger loss of oceanic-fixed nitrogen (Kalvelage et al., 2013).

In order to better understand and predict the future evolution of the ESP OMZ, it is necessary an in-depth analysis of the pathways and terms involved in its oxygen supply. Ventilation in the ocean interior is achieved by advection (i.e. mean ocean currents) of surface waters subducted below the mixed layer (Luyten et al., 1983) and by turbulent diffusion (both epineutral and dianeutral) at many different scales, from mesoscale eddies (tens to hundreds of kilometres) to the local breaking of internal waves or double diffusion processes (scale of meters) (Fischer et al., 2013). Advective and turbulent mixing in the ocean occur mainly along neutral surfaces (Jacket and MacDougall, 1997). Consequently, the oxygen gradients are in general much smaller along the neutral surfaces than across them (e.g. Talley et al., 2011).

In this study we use climatological Argo and oxygen data to compute the annual mean oxygen fluxes due to epineutral advection, epineutral diffusion and dianeutral diffusion for the whole ESP. We examine the role played by each term in the oxygen supply at several isoneutral layers, and compute the rate of respiration necessary to close the annual mean oxygen budget for the whole volume of the ESP OMZ. Previous studies on the ventilation of the ESP OMZ have focused mostly on the equatorial advective oxygen supply (Stramma et al. 2010a), through the eastward flowing currents of the Equatorial Current System (Reid, 1965). We provide here a global picture of the advective pathways of oxygen supply into the ESP OMZ and assess, for the first time, the relevance of the subtropical oxygen supply.

The results obtained here will probably be disrupted by the strong interannual variability mode known as El Niño-Southern-Oscillation (ENSO), which is known to greatly alter the oceanographic conditions in the upper layers of the ESP (e.g. Philander, 1983; Barber and Chavez, 1983). Furthermore, it is possible that there are significant seasonal changes, particularly as a result of changes in the location of the South Pacific high pressure system. Nevertheless, they represent a fundamental step to improve our understanding of the main long-term patterns of oxygen supply.

4.2 Data Set and Methodology

The World Ocean Atlas 2013 (WOA-13) provides climatological mean fields of dissolved oxygen at standard depth levels for the global ocean with a 1° resolution on a Mercator grid (http://www.nodc.noaa.gov/OC5/woa13/) (García et al., 2014).

The Argo Program, as a part of the Global Ocean Observing System, has currently achieved more than 3,000 profiling floats drifting in the global ocean. Each float regularly performs conductivity,

temperature, and depth (CTD) profiles (typically, every ten days from 2,000 m up to the sea surface) and the data gathered is submitted via satellite. The data are quality checked and made freely available by the International Argo program and the national programs that contribute to it (http://www.argo.ucsd.edu, http://argo.jcommops.org). This dataset has been recently combined to create Argo-derived climatological fields of salinity and temperature (http://sio-argo.ucsd.edu/RG_Climatology.html). The analysis method used to create this Argo climatology is described in Roemmich and Gilson (2009); here we use the latest version available (1°, Mercator grid) including data from 1 January 2004 to 31 December 2012.

We use the annual mean CTD and dissolved oxygen fields in order to compute the advective and turbulent diffusive oxygen fluxes into the ESP OMZ following the methodology explained below. For the purpose of this study, the oxygen fluxes due to the annual mean advection (purely geostrophic) and to the annual mean turbulent diffusion (both epineutral and dianeutral) are computed within a 3D grid at 1º resolution (Mercator grid) for most of the ESP.

4.2.1 Annual mean advective field

We have converted the annual mean fields of salinity, in-situ temperature and pressure from the Argo climatology into fields of absolute salinity (SA) and conservative temperature (CT) with TEOS-10 (the new standard for the calculation of the thermodynamic properties of seawater, http://www.TEOS-10.org). We favour the use of these variables because they are more thermodynamically consistent according to the report by IOC et al. (2010).

Transport of mass and tracers in the ocean occurs preferentially along neutral surfaces. Therefore, we use our data set to calculate neutral surfaces (i.e. neutral density anomaly surfaces = neutral density - 1000 kg m^{-3}) according to Jackett and Mcdougall (1997). All hydrographic data (Argo and WOA-13) is subsequently interpolated onto this set of reference neutral surfaces.

The next step is to calculate the approximate isopycnal geostrophic streamfunction as defined in McDougall-Klocker (2010) (see Eqn. (3.30.1) of IOC et al. (2010)). This is the geostrophic streamfunction for the difference between the horizontal velocity at the pressure examined and the horizontal velocity at the reference pressure. It is designed to be used as the geostrophic streamfunction in an approximately neutral surface. The geostrophic streamfunction obtained represents a geopotential anomaly ($m^{-2}\,s^{-2}$) field, with its horizontal gradient representing the horizontal pressure gradient force and its contours representing the streamlines of the geostrophic flow (e.g. Talley et al 2011).

In order to choose the best reference pressure (to eventually compute the absolute geostrophic velocity field) two methods have been assessed. In the first method we use the sea surface as the reference pressure. For this purpose the delayed-time maps of absolute dynamic topography (DT-MADT) at

1/3º (Mercator grid) produced by the AVISO program (Archiving, Validation and Interpretation of Satellite Oceanographic data, http://www.aviso.oceanobs.com/duacs/) were interpolated into our 1º(Mercator grid) and averaged over the period covered by the Roemmich-Gilson Argo climatology (2004-2012). The MADT field obtained is then converted into a sea surface geopotential anomaly field which is used as the reference for the geostrophic velocity computation.

In the second approach we assume there is a single level of no motion for the entire region and use it as the reference pressure. The conservation of mass (or volume, assuming incompressibility) within the ESP OMZ volume is imposed in order to select the best reference level. We exclude the Ekman layer from the analysis as the ESP OMZ is mostly located in the ocean interior and thus it is mainly influenced by the geostrophic velocity field.

We find that referencing to the sea surface (MADT) does much worse at conserving mass than the choice of a level of no motion; this is because errors in the sea surface MADT may lead to velocity errors which are relatively small as compared with the absolute surface velocity but may lead to substantial mass conservation errors when integrated over the entire water column. The best conservation of mass is found when referencing to 1950 dbar (Figure 2). Using this reference pressure, the field of absolute geostrophic velocity is calculated using this reference level; in order to avoid the problems related to the vanishing of the Coriolis parameter very close to the equator, we set a low-latitude limit of 4ºS.

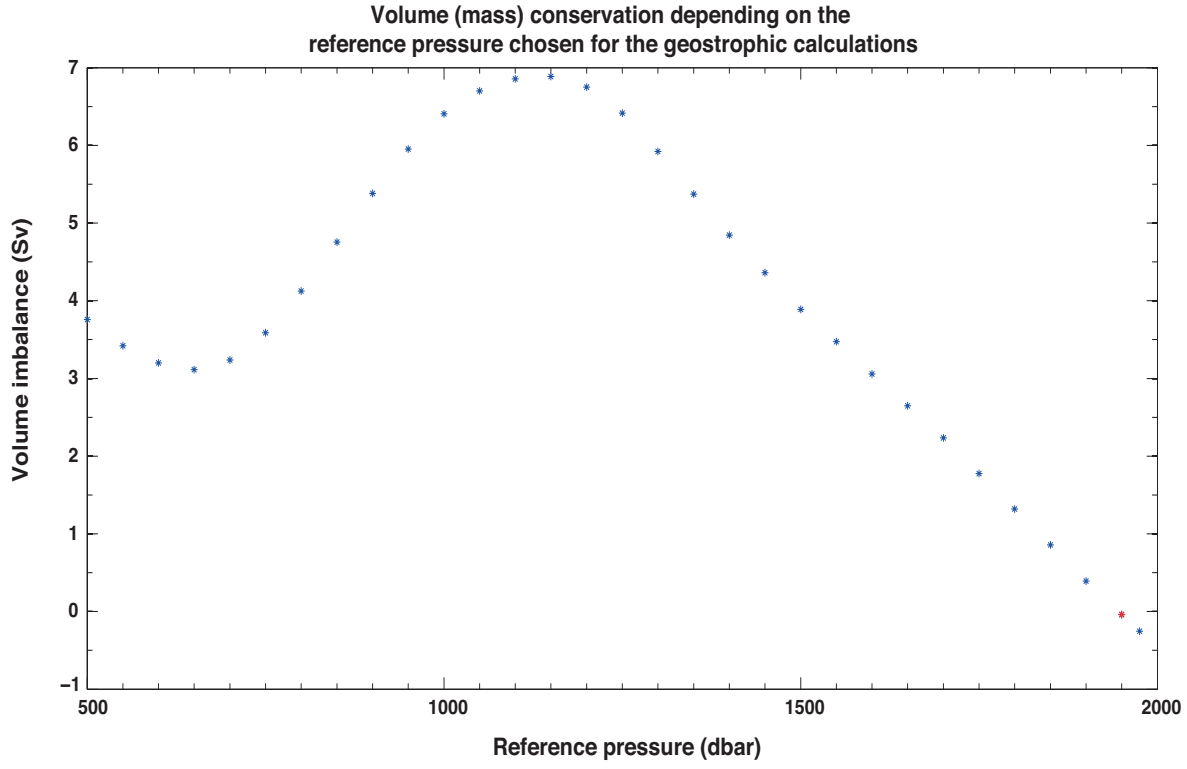

Fig.2 Dependence of the net volume (mass) transport into the ESP OMZ (Sv) on the reference pressure level chosen for the geostrophic calculations. The reference pressure chosen for this study is 1950 dbar (red star).

The final step is to compute the mean (epineutral) advective geostrophic fluxes of oxygen (kmol s^{-1} m^{-2}) over several neutral density surfaces. For this purpose the dissolved oxygen (kmol m^{-3}) climatological field (WOA-2013) is multiplied by the absolute geostrophic velocity field (m s^{-1}), $\vec{v}O_2 = (uO_2, vO_2, 0)$. For our calculations we use the convention of the *x* axis along parallels and the *y* axis along meridians, with the positive directions towards the East and North, respectively.

4.2.2 Annual-mean turbulent diffusive field

Dissolved oxygen data from WOA-2013, interpolated onto reference neutral surfaces, are used to compute the horizontal (epineutral) and vertical (dianeutral) oxygen gradients for the whole ESP. Once we know the oxygen gradients, in order to compute the turbulent diffusive flux we use the classical analogy with diffusion in molecular motions, where the n component of the turbulent flux of oxygen is parameterized as directly proportional to a diffusion coefficient (K, m^2 s^{-1}) times the gradient of oxygen in the n direction, with a negative sign to account that the property diffuses in the counter-gradient direction.

For the epineutral eddy diffusivity, we use the zonal (K_x ~3.1×10^3 m^2 s^{-1}) and meridional (K_y ~1.8×10^3 m^2 s^{-1}) surface values calculated by Chaigneau et al. (2005) in the region covering the South Equatorial Current (SEC) (10º-20ºS, 100º-80ºW), which includes most of the ESP OMZ. For the subsurface values we follow Hahn et al. (2014); according to these authors, the eddy diffusivity decreases by 78% in the depth interval from 100 a 1000 m in the North Atlantic OMZ. Due to the lack of similar studies for the ESP OMZ, we fit an exponentially decreasing function to the sea surface eddy diffusivity coefficients (Chaigneau et al., 2005) which leads to the same 78% decrease at 1000 m depth.

The dianeutral eddy diffusivity coefficient was taken from Fischer et al. (2013) who estimated a mean value of 1×10^{-5} m^2 s^{-1} for the North Atlantic OMZ. This value is well within the range of values inferred by Whalen et al. (2014) using Argo data from the ESP. Note that epineutral diffusivity coefficients (K_x, K_y) are much larger (~10^3 m^2 s^{-1}) than the dianeutral diffusivity coefficient (K_z, ~10^{-5} m^2 s^{-1}).

Finally, we computed the epineutral and dianeutral turbulent diffusive oxygen fluxes at the reference neutral density surfaces for the whole ESP as the eddy diffusion coefficient times the horizontal gradient of the dissolved-oxygen concentration, ($-K_x \partial O_2/\partial x$, $-K_y \partial O_2/\partial y$, $-K_z \partial O_2/\partial z$). Figure 3 shows the annual mean advective and turbulent oxygen fluxes (kmol s^{-1} m^2) along the neutral surface that go through the ESP OMZ core.

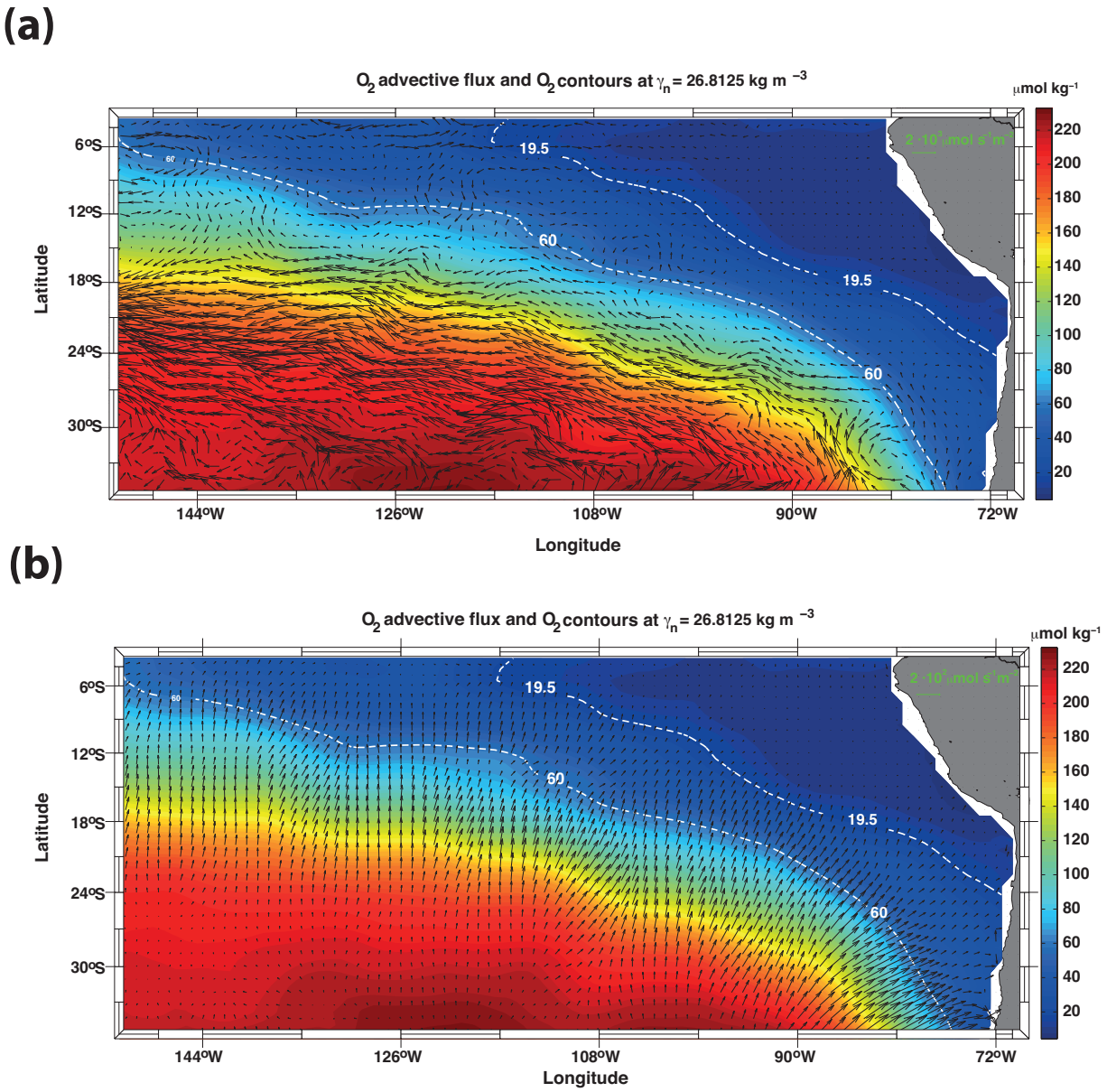

Fig.3. Distribution of **(a)** advective and **(b)** turbulent epineutral oxygen fluxes (μmol s^{-1} m^{-2}) over γ_n = 26.81 kg m^{-3}. The ESP OMZ boundary (contour of 60 μmol kg^{-1}) and its core (contour of 19.5 μmol kg^{-1}) are shown as white dashed lines.

4.2.3 Integrated transports

Integration of the water flux (or velocity, m s^{-1}) and oxygen flux (kmol s^{-1} m^{-2}) over elements of area lead to water transport (m^3 s^{-1}) and oxygen transport (kmol s^{-1}). Throughout this work we will use element of areas in isoneutral coordinates, i.e., with the vertical distance corresponding to the distance between two isoneutral surfaces separated by a constant difference δn. Specifically, we will

use two different elements of area: (1) those belonging to the contour of the OMZ to be used for the calculation of the fluxes into or out-of the ESP (section 2.4), and (2) those along constant parallels for the calculation of the ventilation patterns as described next. Finally, when assessing the total transports in or out of the ESP OMZ, we will add the transports for all individual isoneutral layers, effectively corresponding to a vertical integration of the transports.

In order to provide a view of the advective and diffusive ventilation patterns in the ESP, the accumulated meridional advective and diffusive oxygen (kmol s^{-1}) and volume (Sv) transports are calculated following two steps. First, the calculated epineutral advective and turbulent oxygen fluxes are interpolated onto the center of each vertical wall (composed of four grid points) and then converted into oxygen (and mass) transports across each of these individual walls. Second, for each reference neutral surface, the meridional transports are integrated in the negative x direction, i.e., westward from the South American coast:

$$\begin{aligned} O_2 v\,\hat{j} \quad &\rightarrow \quad \int_{x_c}^{x} O_2 v\hat{j}\,\delta z\,dx = \int_{coast}^{150°W} O_2 v\,\hat{j}\,\delta n\,\frac{\partial z}{\partial n}\,dx \\ -K_y \frac{\partial O_2}{\partial y}\,\hat{j} \quad &\rightarrow \quad \int_{x_c}^{x} -K_y \frac{\partial O_2}{\partial y}\,\hat{j}\,\delta z\,dx = \int_{coast}^{150°W} -K_y \frac{\partial O_2}{\partial y}\,\hat{j}\,\delta n\,\frac{\partial z}{\partial n}\,dx \end{aligned} \qquad (1)$$

where $\hat{j}$ refers to the unitary vector in the meridional direction, and $\delta z = \delta n(\partial z/\partial n)$ is the vertical distance corresponding to an isoneutral layer of thickness δn = 0.125 kg m^{-3}; as the vertical distance is a function of the horizontal location, it is maintained inside the integral. The integration runs from the meridian at the coast, x_c, through every meridian up to 150°W.

4.2.4 Closed oxygen budget terms

In order to calculate the divergence of the flux inside the ESP OMZ we use the Gauss theorem, i.e., we integrate the advective and diffusive flux vectors over the region enclosing this volume:

$$\iiint_V \vec{\nabla} \cdot \vec{F} dV = \oiint_S \vec{F} \cdot d\vec{S} \qquad (2)$$

where the vector $\vec{F}$ stands for either the diffusive or the advective flux of oxygen, and S stands for the area of integration (made out of elements $d\vec{S} = dS\,\hat{n}$, where $\hat{n}$ is the outward unitary vector perpendicular to the surface) englobing the OMZ of volume V (made of elements dV). Here, the closed surface considered as the ESP OMZ boundary is the oxygen isosurface of 60 μmol kg^{-1}; this is a tilted surface, discretized as a combination of horizontal slabs superimposed one onto another. Each slab represents the volume of the ESP OMZ found inside each isoneutral layer and its shape is defined by the oxygen contour of 60 μmol kg^{-1} at the neutral surface located in the centre of each isoneutral layer. The thickness of each slab is not uniform in space and is defined as the thickness of the isoneutral layer at each point inside the OMZ. Thus, this thickness is idealized as several contiguous vertical planes, being the size of each vertical plane dependent on the spatial location.

We calculate the divergence of the advective and turbulent (epineutral and dianeutral) oxygen fluxes within the ESP OMZ, $\iiint_V \vec{\nabla} \cdot \vec{F} dV$, by integrating the projection of these fluxes over the ESP OMZ boundary surface enclosing the volume of study, $\oiint_S \vec{F} \cdot d\vec{S}$

The epineutral advective and turbulent oxygen fluxes, previously computed for the whole ESP, are interpolated onto the OMZ boundary for all isoneutral layers. Then, for each isoneutral layer, the vectors of the advective flux are rotated and projected over the unitary vectors $\hat{n}$ perpendicular to the ESP OMZ boundary. This process is not necessary for the turbulent fluxes as they are defined in the counter-gradient direction, i.e., normal to the OMZ boundary. The projected oxygen fluxes are finally integrated over the vertical walls of all isoneutral layers; the area crossed by each projected flux vector is calculated taking into account the width of each horizontal boundary segment and the height of the isoneutral layer at each segment. Finally, the integration is computed as the addition of all individual contributions.

For each isoneutral layer, the dianeutral turbulent oxygen flux is integrated over the region delimited by the oxygen contour of 60 μmol kg^{-1} found in the neutral surface representing its upper limit. The same is done at the neutral surface representing its lower limit. Then, the oxygen flux divergence for each isoneutral layer within the OMZ is calculated. When computing the oxygen flux divergence for the whole volume of the ESP OMZ we should integrate all the flux crossing the closed oxygen surface used as the boundary. As we discretized the OMZ volume as a series of superimposed slabs, only the flux crossing the upper and lower limits of each slab that is not covered by contiguous slabs should is taken into account.

Karstensen et al. (2008) assessed oxygen consumption in the Pacific OMZs as an apparent oxygen utilization rate (aOUR), through the combination of apparent oxygen utilization (AOU) values and the water mass ages derived from the CFC-11/^{14}C, both provided in the GLODAP dataset (Sabine et al., 2005). They fitted a depth dependent logarithmic function to their data in order to represent the biological consumption of oxygen (aOUR, in μmol kg^{-1}year^{-1}). This function represents an exponential decay of the dissolved oxygen with increasing depth (z):

$$\text{aOUR}(z) = -0.5 + 12.0\exp(-0.0021z) \quad (3)$$

We have first applied this expression over the depth range of each layer and integrated the results over the volume of each isoneutral layer of the ESP OMZ. In this way we have calculated the mean biological consumption of oxygen within each isoneutral layer and for the whole volume of the ESP OMZ.

By definition, positive divergence of a parameter flux within the volume of study indicates a decrease of the concentration of the parameter inside such volume, whereas negative divergence or convergence indicates an increase in the concentration of the parameter. Once calculated the divergence of the advective and turbulent oxygen fluxes and the biological oxygen consumption (oxygen sink), the annual mean oxygen budget can be unveiled as follows:

$$\frac{\partial O_2}{\partial t} = -\oiint_S O_2\vec{v}\cdot d\vec{S} + \oiint_S\left(-K_x\frac{\partial O_2}{\partial x}\hat{i} - K_y\frac{\partial O_2}{\partial y}\hat{j}\right)\cdot d\vec{S} + \oiint_S -K_z\frac{\partial O_2}{\partial z}\hat{k}\cdot d\vec{S} + \iiint_v aOUR\cdot dV \quad (4)$$

where $\hat{i}$, $\hat{j}$ and $\hat{k}$ represent the unitary vectors in the (*x, y, z*) directions.

4.2.5 Error propagation analysis

In the above computations there are several sources of error. Chaigneau et al. (2005) estimated the zonal and meridional eddy diffusivity coefficient errors to be respectively $\pm 0.3\times10^3$ m^2 s^{-1} and $\pm 0.2\times10^3$ m^2 s^{-1} for a 95% confidence interval. Fischer et al. (2013) estimated the vertical turbulent diffusivity coefficient error to be $\pm 0.2\times10^{-5}$ m^2 s^{-1}, whereas Karstensen et al. (2008) acknowledged a 40% error for the 95% confidence interval in their logarithmic function to derive the oxygen consumption as ± 0.4 [-0.5 + 12.0 exp(-0.0021z)]

In addition, oxygen concentration standard errors are provided in WOA-13. These error values are averaged within the volume of study and the resulting value is multiplied by 1.96 (assuming a Gaussian distribution) to obtain the oxygen concentration error with a 95% confidence interval: $\pm 4.543 \times 10^{-6}$ kmol m^{-3}.

The hydrographic Argo dataset is also subjected to errors that influence our results and which can be synthesized in the form of a geopotential field error. From Roemmich and Gilson (2009) we know that the steric-height maximum variance at the sea surface is 0.75 cm^2 for the region between 30º-4ºS. We assume that the square root of this maximum variance represents the error for the 95% confidence interval, i.e., $\sqrt{(0.75\ cm^2)} = \pm 0.8660$ cm = ±1.96 × standard deviation. This error in steric height (cm) is converted into geopotential anomaly error multiplying by the gravity acceleration constant (9.8 m s^{-2}) resulting in a maximum absolute error of geopotential anomaly of $\pm 0.0849\ m^2\ s^{-2}$ for the 95% confidence interval. Recall the geopotential anomaly is calculated integrating the specific volume anomalies in the water column from the reference pressure level, therefore the geopotential anomaly error may be understood as a vertically-integrated value that is directly proportional to the error in the computed sea surface geostrophic velocity field.

The error in the advective oxygen flux calculation is the combined result of the error in the velocity and oxygen calculations, as calculated using standard propagation error techniques. On the other hand, the error in the turbulent diffusive fluxes results from the errors in oxygen data (from WOA-13) and the errors associated to the turbulent diffusivity coefficients.

We have conducted an error propagation analysis where errors are estimated for the 95% confidence interval for each term involved in the closed oxygen budget. First, we assess the error propagation from the geopotential anomaly field to the geostrophic velocity field by a series of Monte Carlo simulations, obtaining an average error for the geostrophic velocity field of 0.074 cm s^{-1}. Second, we calculated the same propagation error but with the classical error propagation formula. We obtained an average error for the geostrophic velocity field of 0.163 cm s^{-1}. As expected, the classical method produces larger error estimates than the Monte Carlo method, approximately by a factor of two; we will now show the results using the more negative scenario (the classical method) though it may over-estimate the errors by up to a factor of two. Therefore, we calculate the error propagation for each term as follows:

$$\delta_v = \sqrt{\left(\frac{\delta v}{|\bar{v}_2|}\right)^2 + \left(\frac{\delta O_2}{|\overline{O}_2|}\right)^2}$$

$$\delta_{K_h} = \sqrt{\left(\frac{\delta K_H}{|K_h|}\right)^2 + \left(\frac{\delta O_2}{|\overline{O}_2|}\right)^2} \quad , \quad K_h = \sqrt{K_x{}^2 + K_y{}^2} \qquad (5)$$

$$\delta_{K_Z} = \sqrt{\left(\frac{\delta K_z}{|K_z|}\right)^2 + \left(\frac{\delta O_2}{|\overline{O}_2|}\right)^2}$$

$$\delta_{fluxes} = \sqrt{\delta_v{}^2 + \delta_{K_h}{}^2 + \delta_{K_Z}{}^2}$$

$$\delta_{respiration} = \pm 0.4 \iiint aOUR \, dV$$

Finally, an independent error estimate may be drawn from the observation of non-zero volume conservation. The error in the volume unbalance (Sv) is simply converted into an average error of velocity through the division of the volume error by the area of the volume of study. The error obtained (0.0496 cm s^{-1}), is about three times smaller than the propagation error in the geostrophic velocity (0.163 cm s^{-1}).

4.3 Results

4.3.1 Oxygen supply pathways into the ESP OMZ

It has been traditionally assumed that the ventilation (by advection) of the ESP OMZ is only achieved by the eastward flowing currents of the Equatorial Current System (e.g. Reid, 1965; Stramma et al. 2010). However, our results show the relevance of the subtropical supply of oxygen, representing an unexplored southern pathway. This pathway includes contributions from two equatorward flows: the north-eastern portion of the subtropical gyre that flows equatorward leaving the gyre and the eastern boundary current, either known as the Peru-Chile Current (PCC) or the Humboldt Current (HC) (Figures 4a, 4b, 5a, 5b). To assess the relevance of the equatorial and subtropical pathways we have computed the (advective) supply and net gain of oxygen corresponding to each pathway.

As the geostrophic velocity calculations are limited to the south of 4ºS, we can only directly examine the equatorial pathways of oxygen supply southward of this latitude. Nevertheless, we assume that the oxygen supply fluxes crossing the 4ºS parallel come from the Equatorial Current System and account them within the equatorial supply pathway. The currents considered to belong to the

equatorial route have a predominant zonal flow whereas the currents associated with the subtropical route have a clear meridional component. However, to objectively distinguish between these two routes, we use the region of minimum geopotential anomaly separating the subtropical gyre and the equatorial current system and look for the point where the contour of minimum geopotential anomaly (or its axis when possible) intersects with the boundary of the ESP OMZ. The flow getting into the ESP OMZ to the south of such point is considered to belong to the subtropical route and the flow entering the ESP OMZ to the north of this point is considered to belong to the equatorial route.

a)

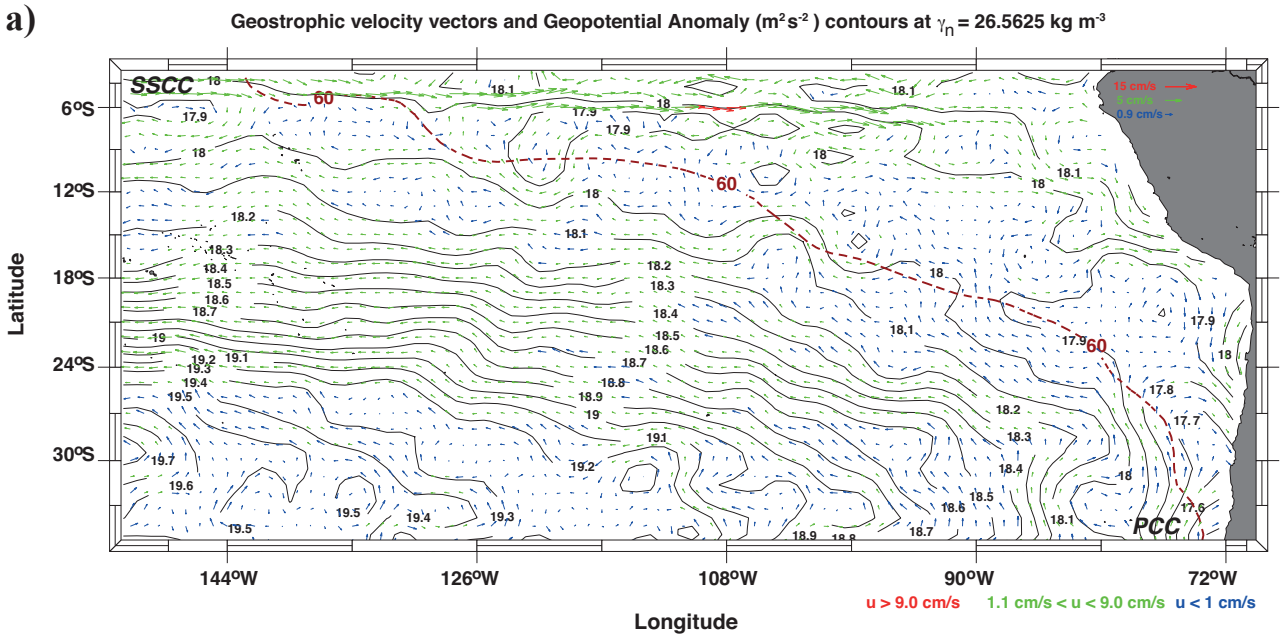

b)

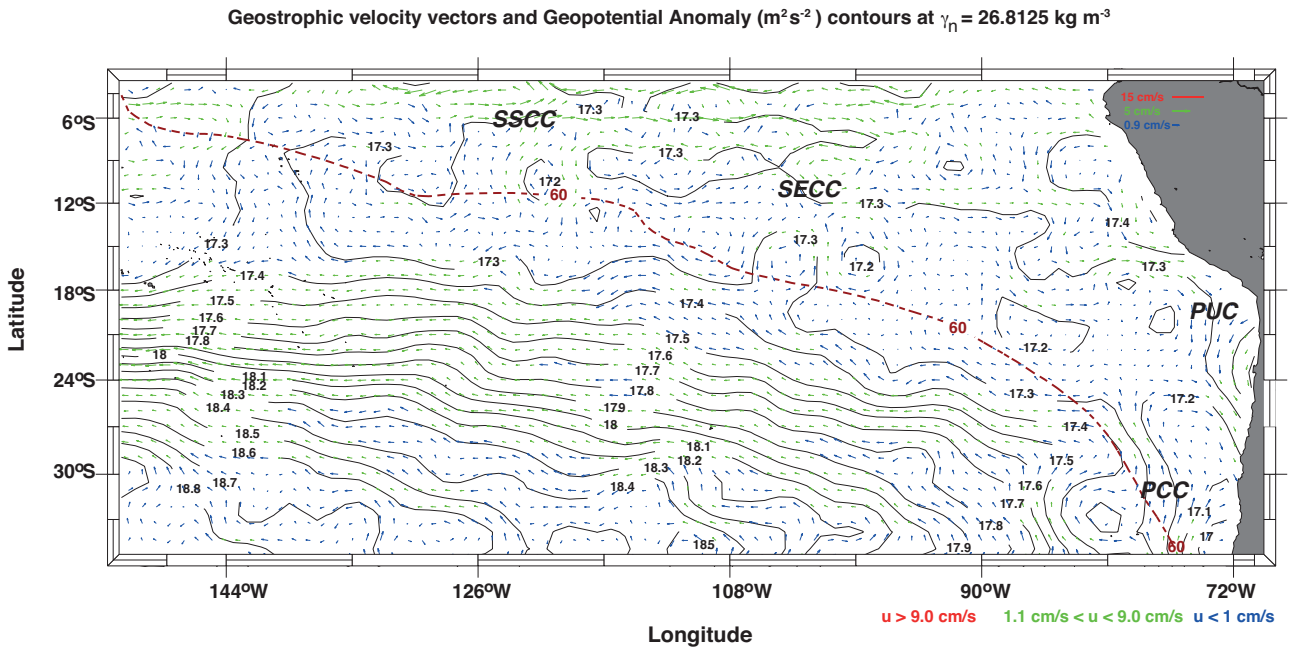

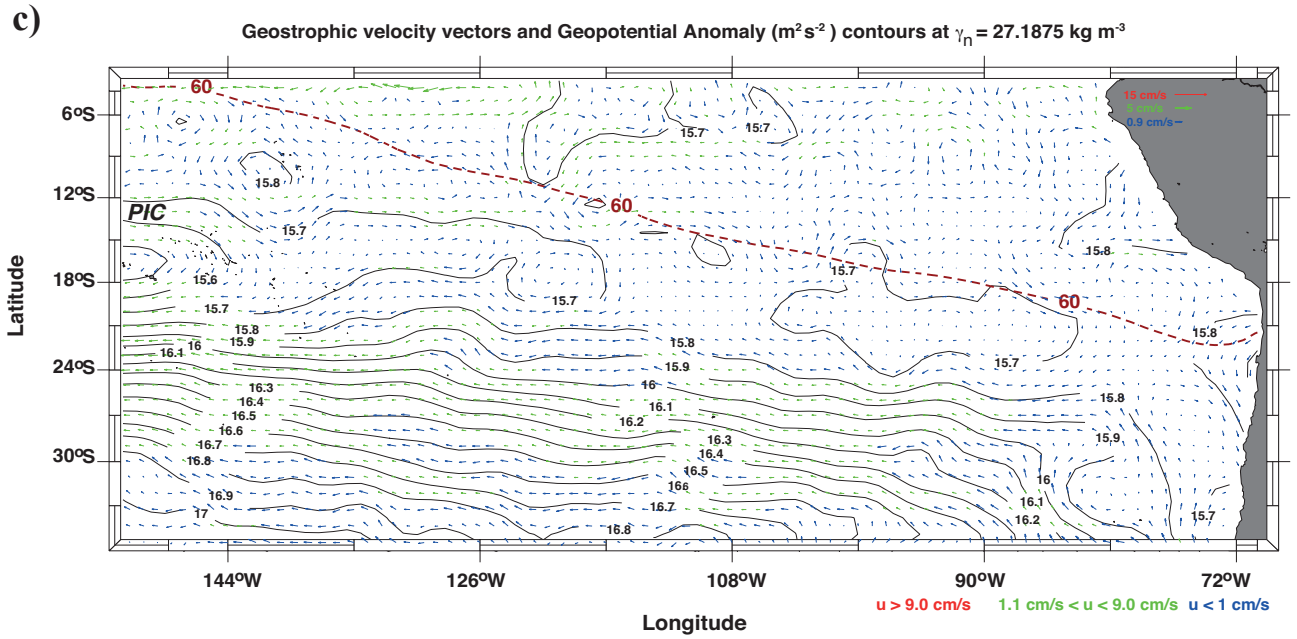

Fig.4 Geostrophic velocity vectors scaled (cm s^{-1}) and geopotential anomaly contours (m^2 s^{-2}). **(a)** Over γ_n = 26.56 kg m^{-3} (~247 m). **(b)** Over the core of the ESP OMZ at γ_n = 26.81 kg m^{-3} (~350 m); the southern Subsurface Countercurrent (SSCC) and the Peru-Chile Current (PCC) are shown. **(c)** Over γ_n = 27.18 kg m^{-3} (~590 m); the Polynesian Intermediate Current (PIC) is shown.

Figure 4a clearly shows a zonal current flowing eastward between 4º-6ºS into the ESP OMZ at the neutral surface of γ_n = 26.56 kg m^{-3} (~247 m), which we identify with the South Pacific Tsuchiya Jet (Tsuchiya 1975), also known as the southern Subsurface Counter Current (SSCC) (Kessler, 2006; Stramma et al., 2010). At 126ºW, the SSCC core depth is found at γ_n = 26.5 kg m^{-3} (~240 m) (Figure 5c, 5d) but this neutral surface rises in depth eastward and the core of SSCC is found at 150 m at 110ºW (Johnson and Moore, 1997; Rowe et al., 2000). According to our results, the SSCC contributes with 37.2% (174.7 kmol s^{-1}) of the advective equatorial supply of oxygen between γ_n = 26.125 kg m^{-3} and γ_n = 26.87 kg m^{-3} (~ 110-370 m) (Table 1). East of 150ºW, we do not find the secondary Southern Subsurface Countercurrent (sSSCC), described by Rowe et al., (2000) as an eastward flowing current at 8ºS over the same neutral surface. This agrees well with Stramma et al., (2010) who did not find either the sSSCC east of 170ºW.

A previously unreported zonal current is found flowing eastward between 12-15ºS all the way into the ESP OMZ, with its core at γ_n = ~27.1 kg m^{-3} (~590 m) (Figures 4c, 5c, 5d). This current, here referred as the Polynesian Intermediate Current (PIC), has not been taken into account in previous studies regarding ventilation of the ESP OMZ; nevertheless, we find it contributes with 18.0% (79.8 kmol s^{-1}) of the advective equatorial oxygen supplied between γ_n = 27 kg m^{-3} and γ_n = 27.375 kg m^{-3} (~450-780 m). The PIC should not be confused with the shallower (γ_n < = 26.81 kg m^{-3}, <350 m) and closer to the equator (10º-12ºS) South Equatorial Countercurrent (SECC) (Reid, 1959; Czeschel et al., 2011), which in Figure 4b is found between 117ºW and 80ºW, well inside the ESP OMZ boundary.

Table 1. Mean advective currents involved in the oxygen supply to the ESP OMZ.

Pathway	Current	O_2 supply (kmol s^{-1})	% of pathway supply	γ_n layers (kg m^{-3})
equatorial	SSCC	174.7	37.2	26.125 - 26.87
	Others	294.9	62.8	
equatorial	PIC	79.8	18	27 - 27.375
	Others	363.5	82	
subtropical	PCC	100.3	52.8	26.125 - 27
	STG	89.5	47.2	

Regarding the subtropical oxygen supply, we distinguish between the supply by the northeastern part of the subtropical gyre, branching towards the equator, and the supply by the Peru-Chile Current (PCC) (Table 1), which is an eastern boundary current (Figure 5a, 5b). We will consider these flows separately because of their different dynamical origin: the PCC is part of the eastern boundary current upwelling system whereas the broad northward flow further west belongs to the subtropical gyre regime (e.g. Talley et al., 2001). At 30ºS (Figure 4a), the flow brought by the subtropical gyre can be recognized by its lower zonal gradient in geopotential anomaly (~ -4×10^{-7} m^2 s^{-2}) with contours broadly distributed, negative value means westward gradient), whereas the flow due to the PCC can be identified as the region to the east of 81ºW with a larger zonal gradient in geopotential anomaly (~ 10^{-6} m^2 s^{-2}, contours more tightly distributed). In fact, at 30ºS the PCC zonal width (302 km) is several times the size of the internal Rossby radii of deformation (Ro ~ 50-100 km) as expected for jets associated to the eastern boundary coastal upwelling front.

As the PCC flows equatorward into the ESP OMZ, it transports well oxygenated Subantarctic Water (SAAW) and upper Antarctic Intermediate Water (AAIW) (Llanillo et al., 2013). We observe the PCC crossing the ESP OMZ boundary between 91º-73ºW on the neutral surface of γ_n = 26.56 kg m^{-3} (Figure 4a). Further deep (γ_n = 26.81 kg m^{-3}), it crosses the boundary between 81º-73ºW (Figure 4b). The PCC contributes with 52.8% (100.3 kmol s^{-1}) of the advective subtropical supply of oxygen between γ_n = 26.125 kg m^{-3} and γ_n = 27 kg m^{-3} (~ 110-450 m) (Table 1). The subtropical gyre (STG) supplies the remainder, representing 47.2% (89.5 kmol s^{-1}) of the subtropical supply of oxygen to the ESP OMZ (Figures 4a, 4b, 5a, 5b).

The subsurface Poleward Undercurrent (PUC) flows southward along the South American continental slope (Strub et al., 1998), probably feeding from the SSCC and the SECC at γ_n = 26.81 kg m^{-3} (Figures 4b, 5a, 5b). The PUC transports Equatorial Subsurface Water (ESSW) with very low oxygen content due to the long term spent in the stagnant circulation zone of the ESP OMZ (Silva et al., 2009). ESSW occasionally feeds the upwelling in the coastal region (Strub et al., 1998) and the

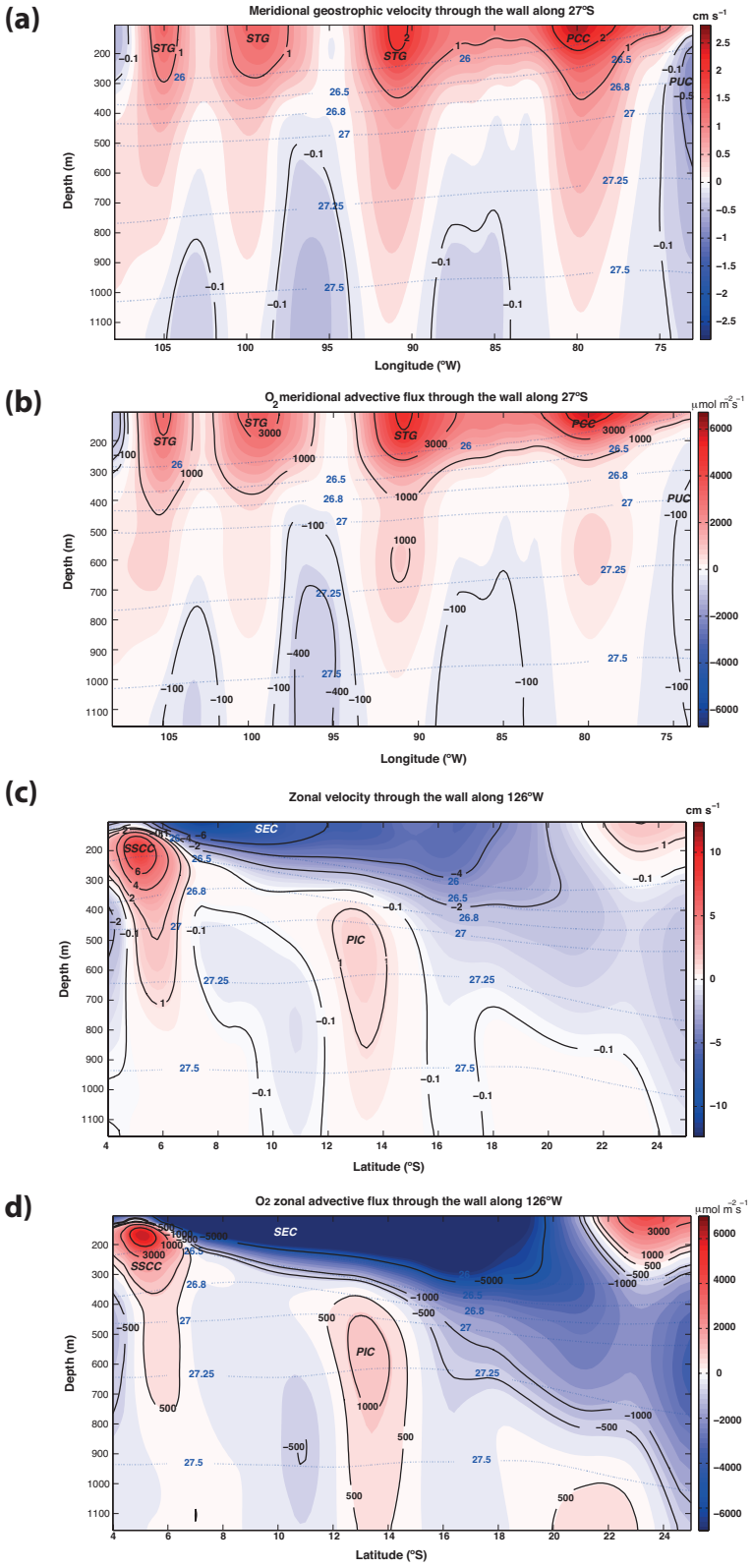

Fig.5 (a) Meridional geostrophic velocity (cm s^{-1}) and **(b)** meridional advective oxygen flux (kmol s^{-1} m^{-2}) across a zonal section at 30ºS (positive northward). **(c)** Zonal velocity (cm s^{-1}) and **(d)** zonal advective oxygen flux (kmol s^{-1} m^{-2}) across a meridional section at 126ºW (positive eastward). The Peru-Chile Current (PCC), the subtropical gyre meridional flow (STG), the Poleward Undercurrent (PUC), the southern Subsurface Countercurrent (SSCC), the South Equatorial Current (SEC), the Polynesian Intermediate Current (PIC) and relevant neutral surfaces (blue dotted lines) are shown.

PUC carries the low oxygen ESSW signature poleward along the Chilean slope (Silva et al., 2009; Llanillo et al., 2012).

The accumulated annual-mean meridional volume transport (Sv) is calculated every 1° integrating westward from the South American coast to 150°W for the neutral surface layer containing the core of the ESP OMZ (Figure 6a). The flux within one isoneutral layer approximately satisfies the continuity equation:

$$\frac{\partial U}{\partial x}+\frac{\partial V}{\partial y}=0 \quad \rightarrow \quad U=\frac{\partial \psi}{\partial y}, \quad V=-\frac{\partial \psi}{\partial x} \tag{6}$$

where (U,V) stand for zonal and meridional transports per unit length ($m^2\ s^{-1}$). A westward integration from the coast, at constant latitude, gives the integrated transport ($m^3\ s^{-1}$) or streamlines

$$\psi(x)-\psi(x_e)=\int_{x_e}^{x}\frac{\partial \psi}{\partial x}\,dx=\int_{x_e}^{x}V\,dx, \tag{7}$$

after assuming the zero streamline flows along the coast (no normal-flow condition). These streamlines show the paths of the PCC mass transport (east of 81ºW) and those of the broad gyre into the ESP OMZ. As expected, the influence of the equatorial pathway becomes more relevant to the northwest of 12ºS, 81ºW as the decreasing values indicate larger influence of the southward mass transport. Notice that the streamlines, to a large degree, resemble the geopotential anomaly lines, the differences responding to the change of the Coriolis parameter with latitude, i.e., a certain constant increment in geopotential anomaly drives a geostrophic current which decreases in latitude.

A similar argument could be used for oxygen transport, calculating the accumulated annual-mean meridional oxygen transport (kmol s^{-1}) through advection (Figure 6b) and turbulent diffusion, and their joint contribution (Figure 6c). However, the contours obtained are not streamlines anymore as oxygen is a non-conservative parameter (i.e. it is influenced by biological consumption). Therefore, these contours should be understood as indicative of regions where the supply of oxygen is of equatorial (negative values) or subtropical (positive values) origin.

In all isoneutral layers the equatorial advective supply of oxygen (calculated by integrating only those streamlines entering into the OMZ) is larger than the subtropical advective supply (Figure 7a, 7b). Since not all of the oxygen transported into the OMZ remains there, we must also compute the net oxygen supply, where the oxygen advected out of the OMZ is also considered. In this case, the equatorial pathway is also dominant in most of the layers, except precisely for those layers containing

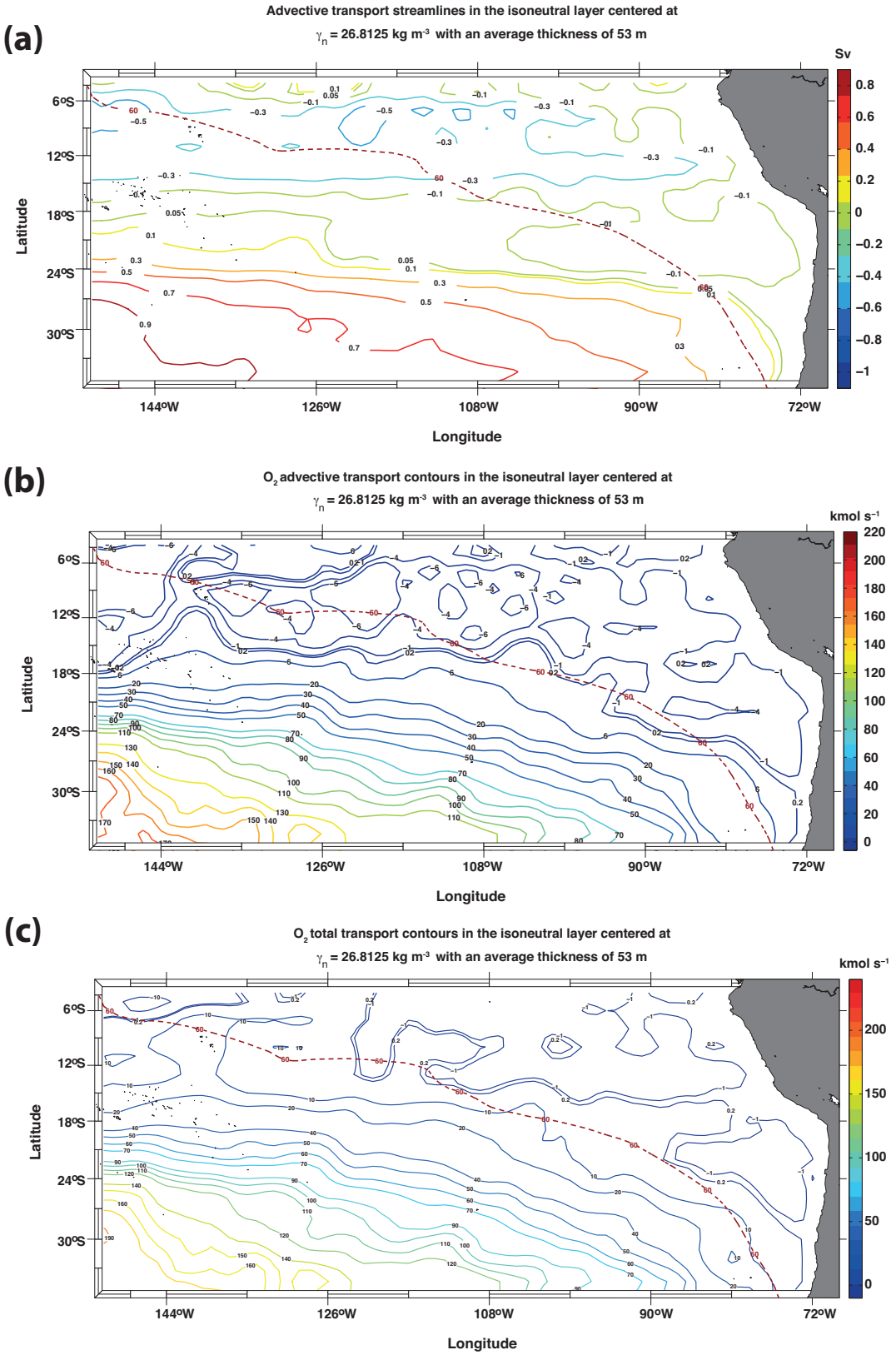

Fig.6 Accumulated transports at γ_n = 26.81 kg m^{-3}. **(a)** Streamlines of meridional accumulated volume transport (Sv) with the ESP OMZ boundary (contour of 60 µmol kg^{-1} as a brown dashed line). **(b)** Contours of meridional accumulated advective transport of oxygen (kmol s^{-1}) at γ_n = 26.81 kg m^{-3}. **(c)** Contours of meridional accumulated net epineutral (advection + turbulent diffusion) transport of oxygen (kmol s^{-1}). Contour of 60 µmol kg^{-1} is shown as a brown dashed line.

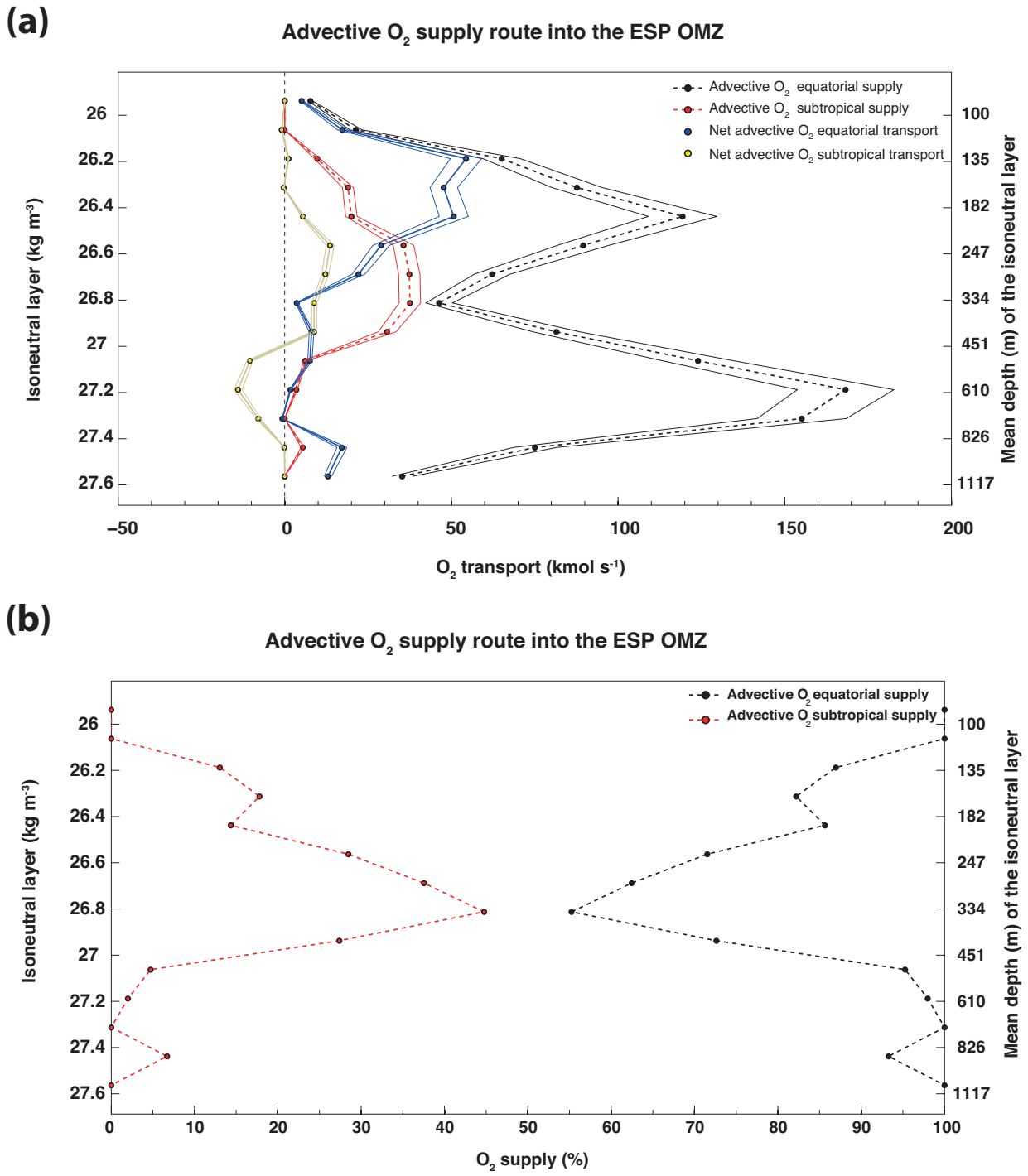

Fig.7. a) Advective oxygen supply (kmol s^{-1}) pathways per isoneutral layer (comparison between supply and net gain) . Thin lines represent the 95 % confidence interval for each term after an error propagation analysis. **b)** Advective oxygen supply (percentages) per pathway and per isoneutral layer.

the core of the OMZ, where the subtropical pathway becomes a relevant supplier of oxygen (Figures 7 and 8). In fact, at the core of the ESP OMZ (γ_n = 26.8 kg m^{-3}, ~350m), the subtropical pathway represents around 45% (~40 kmol s^{-1}) of the advective oxygen supply (Figure 7a, 7b). Furthermore, it provides more net oxygen gain (~8.8 kmol s^{-1}) at this neutral surface layer than the equatorial pathway (~3.6 kmol s^{-1}) (Figure 8a). Regarding the total net gain of oxygen (~70 kmol s^{-1}) at the OMZ core

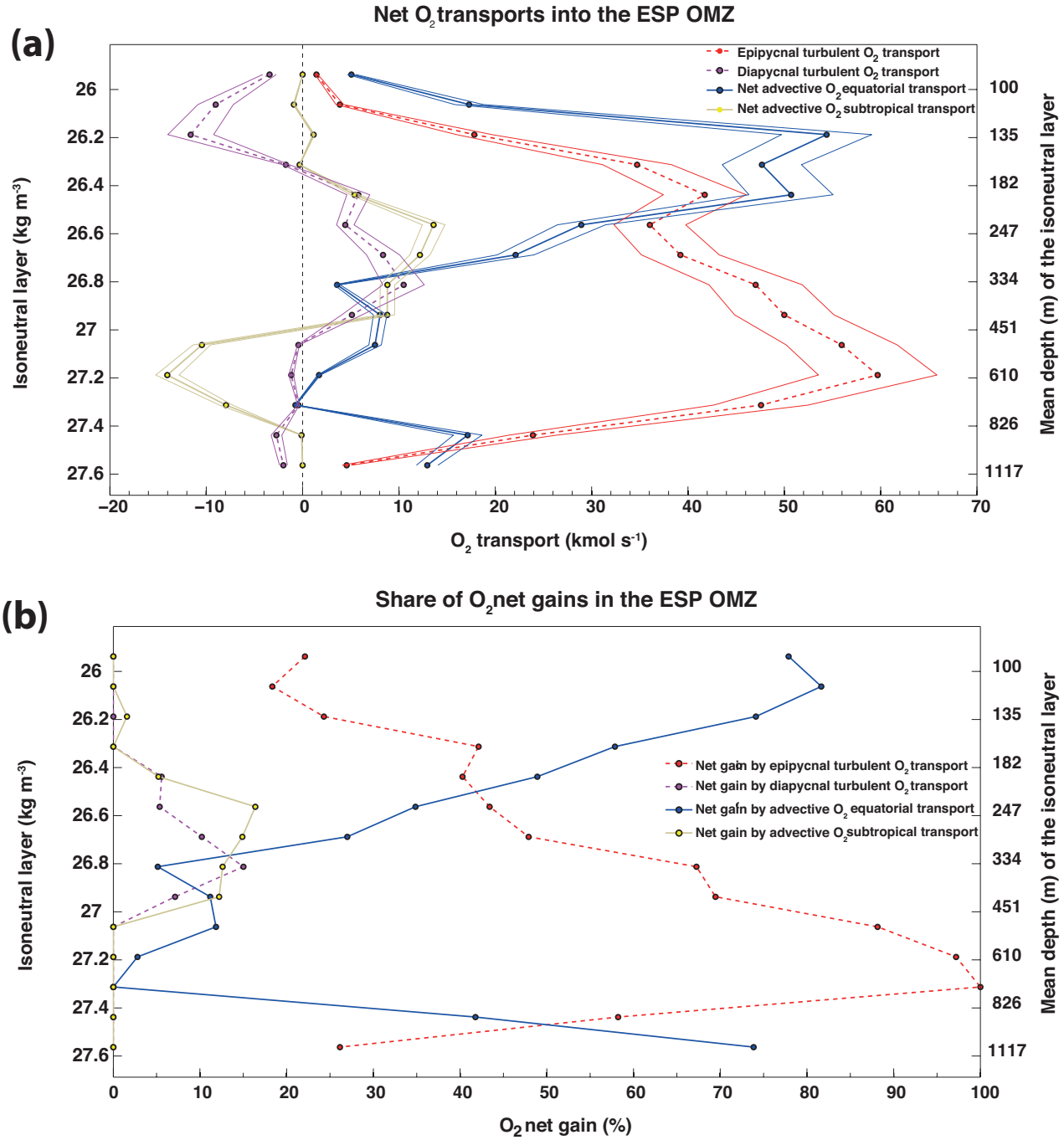

Fig.8 a) Net oxygen transports (kmol s^{-1}) into the ESP OMZ due to epineutral advection, epineutral turbulent diffusion and dianeutral turbulent diffusion per isoneutral layer. Thin lines represent the 95% confidence interval for each term after an error propagation analysis. **b)** Share of net oxygen gains (percentages) due to epineutral advection, epineutral turbulent diffusion and dianeutral turbulent diffusion per isoneutral layer.

layer (including turbulent fluxes), the subtropical pathway is responsible of ~12% of this gain, and the equatorial pathway provides only the ~5% of the oxygen gain (Figure 8b). This clearly reveals the importance of turbulent diffusion which provides the rest of the oxygen supply in this layer. In the next section we will disentangle the relevance and role played by the different terms involved in the oxygen supply, closing the annual mean oxygen budget for the ESP OMZ by computing the required biological consumption per isoneutral layer.

4.3.2 Oxygen supply terms and closed oxygen budget for the ESP OMZ

Besides mean advection, both epineutral and dianeutral turbulent diffusion play an important role in the oxygen supply to the ESP OMZ. In the upper layers (γ_n < 26.6 kg m^{-3}, <250 m), mean advection is the dominant term, being responsible for ~224 kmol s^{-1} (~60%) of the net oxygen supply (Figures 8a, 9). This is due to a large equatorial supply (204 kmol s^{-1}) by the eastward flowing zonal currents, which peaks at the isoneutral layer centered at γ_n = 26.18 kg m^{-3} (~112 m) with 54 kmol s^{-1} (~74% of the total oxygen gain at this layer) (Figures 7a, 7b).

Between about γ_n = 26.75 kg m^{-3} and γ_n = 27.5 kg m^{-3} (~325-960 m), epineutral turbulent diffusion becomes the dominant term, with ~284 kmol s^{-1} (~80%) of integrated net oxygen supply for these layers (Figures 8a, 8b, 9). This is related to the weakening of the mean advective currents with increasing depth (~52 kmol s^{-1}, ~14.6%), leading to reduced ventilation through advection in these layers and the consequent strengthening of the epineutral dissolved-oxygen gradients.

The subtropical advection of oxygen becomes most relevant between γ_n = 26.4 kg m^{-3} and γ_n = 27 kg m^{-3} (~180-450 m), providing ~49 kmol s^{-1} (~12%) of the total oxygen gain in these layers (Figures 8a, 8b). In the same isoneutral layers, oxygen supply by dianeutral turbulent diffusion becomes important providing ~34 kmol s^{-1} (~8.3%). This is somewhat an expected result as the parameterized turbulent dianeutral flux of oxygen inversely follows the vertical oxygen gradient promoting a convergence of the flux in the layers with the lowest values of oxygen and divergence of

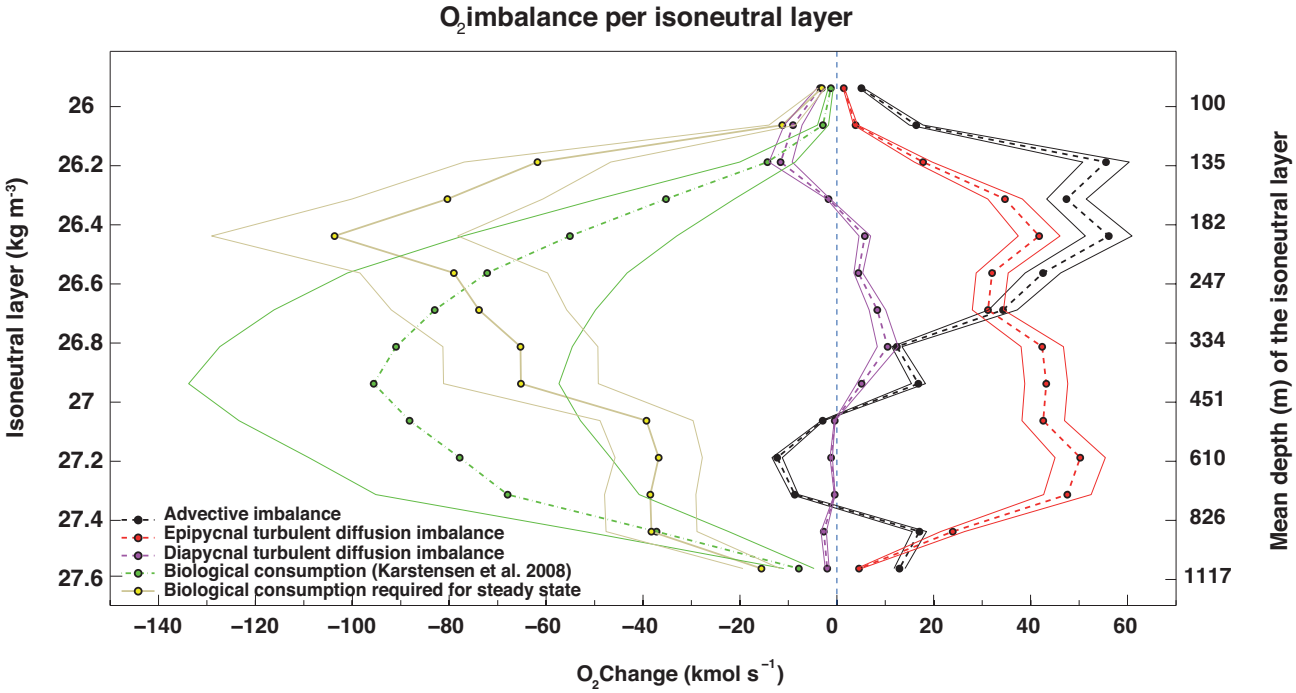

Fig.9. Terms involved in the annual mean oxygen budget (kmol s^{-1}) for the ESP OMZ. Thin lines represent the 95% confidence interval for each term after an error propagation analysis.

the flux in the layers surrounding them.

At the core of the ESP OMZ (γ_n = 26.81 kg m^{-3}, ~350 m), the epineutral turbulent diffusion is the dominant term with a net oxygen supply of ~47 kmol s^{-1} (~67.25% of the total oxygen gain). The net advective oxygen supply is ~12.4 kmol s^{-1} (~17.75%) whereas the dianeutral turbulent diffusion provides up to ~10.5 kmol s^{-1} (15%) (Figures 8a, 8b, 9).

Between γ_n = 27 kg m^{-3} and γ_n = 27.25 kg m^{-3} (~450-650 m), there is a weak equatorial advective net supply ~9.3 kmol s^{-1} (partially due to the PIC described before); this supply cannot compensate for the net loss of oxygen ~-24.5 kmol s^{-1} in the subtropical part of the OMZ, due to a predominant poleward flow in this region (Figures 8a, 4c). This is also revealed when examining the advective term in Figure 9 as it is only in these neutral surfaces where there is divergence of the advective flux, with a net loss of ~-15.2 kmol s^{-1}.

Although OMZs are thought to be expanding, the volume of the ESP OMZ can be assumed to be approximately constant in time for the purposes of this study. Furthermore, for a much more reduced area in the eastern equatorial Pacific, Stramma et al. (2008) found the long-term trend to be quite small and noisy (i.e.–0.13 ± 0.32 μmol kg^{-1} year^{-1}).

Assuming that the ESP OMZ volume is in steady state, the oxygen budget for the whole volume of the ESP OMZ must be zero, i.e. oxygen supply must be balanced by biological consumption. Therefore, after computing the net oxygen supply at each neutral surface layer, we may calculate the mean biological consumption required to maintain the ESP OMZ volume in steady state, i.e., the oxygen sink required to close the oxygen budget.

The mean biological consumption estimated for the whole volume of the ESP OMZ (795.91 kmol s^{-1}) fits remarkably well with the value obtained (718.13 kmol s^{-1}) for the same volume of study after applying Karstensen et al. (2008) logarithmic function. The consumption of oxygen computed here is slightly larger in the upper layers (γ_n < 26.5 kg m^{-3}) but most of it fits inside the range of the 95% confidence interval given in Karstensen et al. (2008) between γ_n = 26.62 kg m^{-3} and γ_n = 27.5 kg m^{-3} (~270-960 m), showing also a substantial decrease within the deepest isoneutral surfaces (Figure 9).

The spatially integrated annual-mean oxygen budget for the ESP OMZ shows that epineutral turbulent diffusion provides a net oxygen supply of 417.4 ± 43.0 kmol s^{-1} (~2.15 μmol kg^{-1}), advection supplies 292.7 ± 25.2 kmol s^{-1} (~1.49 μmol kg^{-1}) and dianeutral turbulent diffusion provides 85.8 ± 17.6 kmol s^{-1} (~0.43 μmol kg^{-1}). Consequently, a biological consumption of 795.9 ± 195.0 kmol s^{-1} (4.07 μmol kg^{-1}) is required to close the budget.

4.3 Conclusions

This study has accomplished two main goals. The first goal was to describe the whole picture of oxygen supply into the ESP OMZ. The second goal was to disentangle the role and importance of each term involved in the oxygen budget of the ESP OMZ.

Regarding the oxygen supply by mean ocean currents, it has been traditionally assumed that the ESP OMZ is ventilated by the eastward flowing currents of the Equatorial Current System. Here we show the relevance of the subtropical supply of oxygen, both from the broad northeastern part of the subtropical gyre and from the equatorward eastern boundary current (Humboldt or Peru-Chile Current). The subtropical pathway into the ESP OMZ represents around 45% of the advective oxygen supply at the core of the ESP OMZ (γ_n= 26.8 kg m^{-3}, ~350 m). Furthermore, at the core it provides much more net oxygen gain (~12%) than the equatorial pathway (~5%). We found that the Humboldt Current is responsible for ~53% of the advective subtropical oxygen supply, while the rest is supplied by the northeastern limb of the subtropical gyre. The subtropical oxygen supply has been described and quantified here for the first time and, given its importance, it should be taken into account in future studies dealing with the maintenance or evolution of the ESP OMZ

The Southern Subsurface Countercurrent (SSCC) provides 37.15% of the advective equatorial supply of oxygen between γ_n = 26.125 kg m^{-3} and γ_n = 26.9 kg m^{-3}. In addition, a new zonal current (here designated as the Polynesian Intermediate Current) has been described flowing eastward all the way into the ESP OMZ between 12-15ºS, with its core located at γ_n = 27.1 kg m^{-3}. This current, despite contributing with 18% of the advective equatorial oxygen supplied between γ_n = 27 kg m^{-3} and γ_n = 27.4 kg m^{-3}, has not been taken into account in previous studies regarding the ventilation of the ESP OMZ.

The reduction of the advective supply leads to a more acute OMZ and, consequently, drives an intensification of the turbulent fluxes. The steady-state arises as long as the biological consumption of oxygen is capable of compensating the joint effect of advective and turbulent supply of oxygen. We have assessed the role played by the mean advection and turbulent diffusion (epineutral and dianeutral) in the global oxygen supply to the whole ESP OMZ. In the upper layers (γ_n < 26.6 kg m^{-3}), mean advection is the dominant term regarding net oxygen supply (~60%), mainly due to a large equatorial supply by the eastward flowing zonal currents. Between about γ_n = 26.75 kg m^{-3} and γ_n = 27.5 kg m^{-3}, epineutral turbulent diffusion becomes the dominant way for oxygen supply (~80%).

At the core of the ESP OMZ, epineutral turbulent diffusion is the dominant term with a net oxygen supply of ~47 kmol s^{-1} (~67.25%). The net advective oxygen supply is ~12.4 kmol s^{-1} (~17.75%) whereas the dianeutral turbulent diffusion provides up to ~10.5 kmol s^{-1} (15%).

Combining all the results obtained, the annual mean oxygen budget for the whole volume of the ESP OMZ is revealed. Epineutral turbulent diffusion provides a net oxygen supply of 417.4 ± 43.0 kmol s^{-1} (~2.15 µmol kg^{-1}), advection supplies 292.7 ± 25.2 kmol s^{-1} (~1.49 µmol kg^{-1}) and dianeutral turbulent diffusion provides 85.8 ± 17.6 kmol s^{-1} (~0.43 µmol kg^{-1}). The mean biological consumption of oxygen required to close the budget is 795.9 ± 195.0 kmol s^{-1} (4.07 µmol kg^{-1}). This value agrees remarkably well with previous independent estimates (Karstensen et al., 2008) giving us confidence on the results obtained in this work. The analysis of the seasonality in the supply pathways, which shall clarify the relative importance of the mean and seasonal contributions, constitutes the basis of a future study which is currently underway.

Acknowledgements

We are very grateful to the anonymous reviewers who provided constructive and useful comments which certainly helped to improve this manuscript. The authors would like to thank Trevor McDougall and Paul Barker for support when using their routine to calculate neutral densities. We would also like to thank John Gilson for his help to solve a size problem when downloading their Argo climatology. The altimeter products were produced by Ssalto/Duacs and distributed by Aviso, with support from CNES (http://www.aviso.oceanobs.com/duacs/).

CHAPTER

5

Conclusions and Future Research

"Everything is theoretically impossible,
until it is done".
Robert A. Heinlein

CONCLUSIONS

The ESP remains one of the least sampled areas of the world ocean. Before the advent of the Argo program era, only a handful of hydrographic sections with modern CTD sensors had been accomplished in this region. However, the ESP is a key region to understand the global climate. The ENSO phenomenon takes place in the equatorial and tropical Pacific but disrupts weather patterns around the world (Philander, 1983). Furthermore, the vigorous upwelling of cold waters found in the ESP has been partially blamed for the observed slowdown in the rise of global mean air temperatures (England et al., 2014). The ESP contains one of the most intense OMZs in the world ocean whose existence not only impacts marine life but also has implications for the global climate by the release of a powerful GHG and the weakening of the biological carbon pump (Kalvelage et al., 2011). Future expansion of the ESP OMZ may threaten one of the most productive fisheries in the world and further disrupt the global climate.

In this dissertation we have used two different approaches in order to contribute towards an improved knowledge on the ESP. The first approach is based on the use of tracer analysis and inverse modeling techniques to examine the water mass structure, its variability and its role in the ventilation of the ESP OMZ. The second approach uses Argo and oxygen climatological data to study the ventilation of the ESP OMZ from a dynamical perspective, computing advective and turbulent oxygen transports.

In the second chapter we have carried out an in-depth characterization of the water types present off the Chilean slope, which has allowed us to describe their detailed spatial distribution. Furthermore, the inferred pathways of the water masses involved in the ventilation and maintenance of the ESP OMZ have been discussed. However, the water mass analysis offshore Chile only captures the southern part of the ESP OMZ. In the third chapter we have completed the vision arising from the previous chapter by conducting a water mass analysis which includes biogeochemical processes for the region offshore Peru and Ecuador, thus capturing the central and northern parts of the ESP OMZ. In addition, we assess the changes induced by two opposite phases of ENSO in the water mass distribution and in the biogeochemical activity, with special emphasis in how these changes modify the ventilation patterns of the ESP OMZ.

The analyses in chapters 2 and 3 have shown the presence of water masses of subantarctic and antarctic origin within the ESP OMZ. These water masses must have reached the ESP OMZ

either through equatorward eastern boundary currents or through contributions from the subtropical gyre. This has been investigated in the fourth chapter, where we provide a global picture of the mean advective pathways of oxygen supply into the ESP OMZ. In addition, we examine the relative roles played by mean advection and mean turbulent diffusion in the net oxygen supply, and compute the biological consumption required to close the oxygen budget of the ESP OMZ.

Two models have been developed as part of this dissertation. The first model involves oceanic tracer analysis. It is an extension of the Optimum Multiparameter Analysis (Tomczak and Large, 1989) and enables to elucidate not only water mass distribution and mixing but also the biogeochemical cycling occurred within the water masses. The second model uses Argo and oxygen data (optionally, also satellite altimetry) in order to calculate the advective flux of oxygen, through the geostrophic currents and the turbulent diffusive oxygen transport, both in the epineutral and dianeutral directions.

Main scientific contributions:

- ✓ In-depth characterization of the water masses found in the ESP. We have provided, for the first time, a set of inorganic nutrients and dissolved oxygen water types for the ESP.

- ✓ The Summer Subantarctic Water (SSAW) has been described as a surface water mass that results from the freshening of subantarctic waters by intensified river runoff, caused by glacier melting during austral summer at the Chilean fjord region.

- ✓ The spatial distribution of water masses off Chile, Peru and Ecuador has been depicted and their inferred spreading pathways have been discussed.

- ✓ The ESP OMZ is mainly formed of low oxygen ESSW. Eventually, this water mass is advected by the PUC poleward along the Chilean slope, spreading the ESP OMZ further south.

- ✓ The ESP OMZ is partially ventilated from the south by the AAIW and SAAW water masses which are advected into this region by the PCC/HC or by detaching from the subtropical gyre.

- ✓ During El Niño conditions (1993) relatively more oxygenated surface waters replace the low-oxygen ESSW in the upper 250 m. Consequently, the upper part of the ESP OMZ is found deeper in the water column and the nitrogen loss by denitrification is reduced in the upper layers.

- ✓ During La Niña conditions (2009), a relatively more vigorous upwelling promotes the rise in depth of the upper part of the ESP OMZ. Consequently, the nutrient-rich and oxygen-poor ESSW replaces the STW in the upper layers north of 10ºS. The amount of oxygen available for respiration is reduced whereas the nitrate loss by denitrification increases.

- ✓ The upward displacement of isopycnals (isopycnal heave) associated with La Niña conditions favors the ventilation of the OMZ by the upper part of the AAIW stratum.

- ✓ A larger supply of oxygen-rich AAIW during 2009 enabled a more vigorous biological consumption, resulting in a net oxygen change of small amplitude. This is in good agreement with a previous interpretation by Paulmier et al. (2006) that pointed to an "oxygen-driven" remineralization inside the Chilean OMZ. This suggests that there is an excess of organic matter waiting to be remineralized whenever oxygen supply increases and this situation favors the existence and maintenance of the ESP OMZ.

- ✓ A recent study found AAIW shoaling south of 15ºS in the ESP (Schmidtko and Johnson, 2012). We have found that, north of 15ºS, AAIW still flowed along shallower isopycnals in 2009 than in 1993. Such shoaling changes the way AAIW ventilates the ESP OMZ and might explain the reported increase in oxygen content off Chile between 200 and 700 m (Stramma et al., 2010b).

- ✓ A global picture of the oxygen supply into ESP OMZ has been provided for the first time. Two main routes contribute to the advective supply of oxygen, the traditional equatorial pathway and the previously unreported subtropical pathway.

- ✓ The subtropical pathway represents ~45% of the advective oxygen supply at the core of the ESP OMZ (γ_n = 26.81 kg m^{-3}) and provides more net oxygen gain (~8.8 kmol s^{-1}) than the equatorial pathway (~3.6 kmol s^{-1}) at this neutral surface layer. This finding challenges the common assumption that the ESP OMZ is only ventilated by the eastward flowing currents of the Equatorial Current System.

- ✓ A previously unreported zonal current, flowing eastward all the way into the ESP OMZ, has been described between 12-15ºS with its core at γ_n = 27.1 kg m^{-3}. This current, here referred as the Polynesian Intermediate Current (PIC), provides about 18% of the advective equatorial oxygen supply between γ_n = 27.0 kg m^{-3} and γ_n = 27.4 kg m^{-3}.

Conclusions and Future Research

- ✓ The role played by the mean advective and turbulent diffusive (epineutral and dianeutral) oxygen supply to the ESP OMZ has been assessed. In the upper layers ($\gamma_n < 26.6$ kg m^{-3}), mean advection dominates the net oxygen supply (~60%), thanks to a large equatorial supply by the eastward flowing zonal currents. However, deeper than $\gamma_n = 26.75$ kg m^{-3}, epineutral turbulent diffusion becomes the dominant source of oxygen (~80%).

- ✓ At the core of the ESP OMZ, epineutral turbulent diffusion is the dominant term with a net oxygen supply of ~47 kmol s^{-1} (~67.25%). The net advective oxygen supply is ~12.4 kmol s^{-1} (~17.75%) whereas the dianeutral turbulent diffusion provides for up to ~10.5 kmol s^{-1} (15%).

- ✓ The annual mean oxygen budget for the whole volume of the ESP OMZ has been unveiled. Epineutral turbulent diffusion provides a net oxygen supply of 417.4 ± 43.0 kmol s^{-1} (~2.15 μmol kg^{-1}), advection supplies 292.7 ± 25.2 kmol s^{-1} (~1.49 μmol kg^{-1}) and dianeutral turbulent diffusion provides 85.8 ± 17.6 kmol s^{-1} (~0.43 μmol kg^{-1}). The mean biological consumption of oxygen required to close the budget is 795.9 ± 195.0 kmol s^{-1} (4.07 μmol kg^{-1}).

FUTURE RESEARCH

"Science will always be a search,
never a real discovery.
It is a journey, never a finish"
Karl Popper

The following lines of research were initiated during the doctoral research period. However, due to time limitations, they could not be completed and have been left out of this dissertation. Nevertheless, they will constitute the basis of future endeavours.

An analysis of the seasonal patterns in the pathways and in the terms involved in the oxygen supply to the ESP OMZ is currently underway. The same model presented in the fourth chapter of this dissertation, with only slight modifications, is being used. We intend to add an Ekman layer module to the model in order to make it capable of accounting for nutrient fluxes in the surface layer as well as abiding better by the mass conservation principle.

During my stay at Scripps Institution of Oceanography we adapted the long-distance geostrophy method, originally developed by Matthias Lankhorst for the North Atlantic (Lankhorst et al., 2008), for its use in the ESP. With this method we intend to derive volume transport time series of the main currents supplying oxygen to the ESP OMZ. The combination of this method with the expected increase in the number of Argo floats carrying an oxygen sensor shall enable deriving oxygen transport time series for the main currents involved in the ventilation of the ESP OMZ.

The use of Lagrangian models might complement the Eulerian vision of the dynamics of oxygen supply to the ESP OMZ. On the other hand, further analysis of the water mass structure in the ESP during different time intervals should help to better understand the long-term variability.

Finally, the analyses accomplished in this dissertation could be applied to other OMZs in the world ocean in order to further understand the mechanisms behind their existence and evolution in time. In particular, the model developed in the fourth chapter could be easily applied to compute transports and budgets of other oceanographic tracers (heat, salt, nutrients) almost everywhere in the world ocean with the exception of the equatorial band.

References

References

Anderson, J. J., Okubo, A., Robbins, A. S., and Richards, F. A.: A model for nitrate distributions in oceanic oxygen minimum zones, Deep Sea Res. Part A. Oceanogr. Res. Pap., 29(9), 1113–1140, 1982.

Anderson, L. A., and Sarmiento, J. L.: Redfield ratios of remineralization determined by nutrient data analysis, Global Biogeochem. Cy., 8, 65-80, 1994.

Anderson, L. A.: On the hydrogen and oxygen content of marine phytoplankton, Deep Sea Res. Part I Oceanogr. Res. Pap., 42(9), 1675–1680, 1995.

Bange, H. W., Naqvi, S. W. A., and Codispoti, L. A.: The nitrogen cycle in the Arabian Sea, Prog. Oceanogr., 65(2-4), 145–158, 2005.

Barber, R. T., and Chavez, F. P.: Biological consequences of El Niño, Science, 222, 1203-1210, 1983.

Bindoff, N. L., and McDougall, T. J.: Diagnosing climate change and ocean ventilation using hydrographic data, J. Phys. Oceanogr., 24, 1137-1152, 1994.

Bopp, L., Le Quéré, C., Heimann, M., Manning, A. C., and Monfray, P.: Climate-induced oceanic oxygen fluxes: Implications for the contemporary carbon budget, Global Biogeochem. Cycles, 16(2), 6–1–6–13, 2002.

Brandt, P., Hormann, V., Körtzinger, A., Visbeck, M., Krahmann, G., Stramma, L., Lumpkin, R., and Schmid, C.: Changes in the ventilation of the oxygen minimum zone of the tropical North Atlantic, J. Phys. Oceanogr., 40(8), 1784–1801, 2010.

Brink, K. H., Halpern, D., Huyer, A., and Smith, R. L.: The physical environment of the Peruvian upwelling system, Progr. Oceanogr., 12, 285-305, 1983.

Broecker, W. S.: “NO”, a conservative water-mass tracer, Earth Planet. Sci. Lett., 23(1), 100–107, 1974.

Chaigneau, A.: Mean surface circulation and mesoscale turbulent flow characteristics in the eastern South Pacific from satellite tracked drifters, J. Geophys. Res., 110(C5), C05014–C05014, 2005.

References

Chavez, F. P., Ryan, J., Lluch-Cota, S. E., and Ñiquen C, M.: From anchovies to sardines and back: multidecadal change in the Pacific Ocean, Science, 299, 217-221, 2003.

Chavez, F. P., Bertrand, A., Guevara-Carrasco, R., Soler, P., and Csirke, J.: The northern Humboldt Current System: Brief history, present status and a view towards the future, Progr. Oceanogr., 79, 95-105, 2008.

Cline, J. D., and Richards, F. A.: Oxigen deficient conditions and nitrate reduction in the eartern tropial north Pacific Ocean, Limnol. Oceanogr. 1, 885–900, 1972.

Codispoti, L. A., and Christensen, J. P.: Nitrification, denitrification and nitrous oxide cycling in the eastern tropical South Pacific ocean, Mar. Chem., 16(4), 277–300, 1985.

Codispoti, L. A., Brandes, J. A., Christensen, J. P., Devol, A. H., Naqvi, S. W. A., Paerl, H. W., and Yoshinari, T.: The oceanic fixed nitrogen and nitrous oxide budgets: Moving targets as we enter the anthropocene?, Scientia Marina, 65, 85-105, 2001.

Czeschel, R., Stramma, L., Schwarzkopf, F. U., Giese, B. S., Funk, A., and Karstensen, J.: Middepth circulation of the eastern tropical South Pacific and its link to the oxygen minimum zone, J. Geophys. Res., 116, C01015, 2011.

Czeschel, R., Stramma, L., and Johnson, G. C.: Oxygen decreases and variability in the eastern equatorial Pacific, J. Geophys. Res., 117, C11019, 2012.

De Pol-Holz, R., Ulloa, O., Lamy, F., Dezileau, L., Sabatier, P., and Hebbeln, D.: Late quaternary variability of sedimentary nitrogen isotopes in the eastern South Pacific Ocean, Paleoceanography, 22, PA2207, 2007.

Deutsch, C., Brix, H., Ito, T., Frenzel, H., and Thompson, L.: Climate-forced variability of ocean hypoxia, Science, 333, 336-339, 2011.

Diaz, V. M.: Distribución de fosfatos, nitratos y nitritos en una sección. Frente a Iquique (201160S), Investig. Pesq. - Inst. Fom. Pesq., (31), 103–108, 1984.

Diaz, R.J., and Rosenberg, R.: Spreading dead zones and consequences for marine ecosystems, Science 321, 926–929, 2008.

References

Duteil, O., and Oschlies, A.: Sensitivity of simulated extent and future evolution of marine suboxia to mixing intensity, Geophys. Res. Lett., 38(6), 2011.

Duteil, O., Schwarzkopf, F. U., Böning, C. W., and Oschlies, A.: Major role of the equatorial current system in setting oxygen levels in the eastern tropical Atlantic Ocean: A high-resolution model study, Geophys. Res. Lett., 41, 2033-2040, 2014.

England, M. H., McGregor, S., Spence, P., Meehl, G. A., Timmermann, A., Cai, W., Gupta, A. Sen, McPhaden, M. J., Purich, A., and Santoso, A.: Recent intensification of wind-driven circulation in the Pacific and the ongoing warming hiatus, Nat. Clim. Chang., 4(3), 222–22, 2014.

Fiedler, P. C., and Talley, L. D.: Hydrography of the eastern tropical Pacific: A review, Progr. Oceanogr., 69, 143-180, 2006.

Fischer, T., Banyte, D., Brandt, P., Dengler, M., Krahmann, G., Tanhua, T., and Visbeck, M.: Diapycnal oxygen supply to the tropical North Atlantic oxygen minimum zone, Biogeosciences, 10(7), 5079–5093, 2013.

Fraga, F., Ríos, A. F., Pérez, F. F., and Figueiras, F. G.: Theoretical limits of oxygen:carbon and oxygen:nitrogen ratios during photosynthesis and mineralisation of organic matter in the sea, Scientia Marina, 62(1-2), 161–168, 1998.

Frölicher, T. L., Joos, F., Plattner, G. K., Steinacher, M., and Doney, S. C.: Natural variability and anthropogenic trends in oceanic oxygen in a coupled carbon cycle-climate model ensemble, Global Biogeochem. Cycles, 23(1), 2009.

Garcia, H. E., and Gordon, L. I.: Oxygen solubility in seawater: Better fitting equations. Limnol. Oceanogr., 37, 1307-1312, 1992.

Garcia, H. E., Locarnini, R. A., Boyer, T. P., Antonov, J. I., Baranova, O.K., Zweng, M.M., Reagan, J.R., and Johnson, D.R.: World Ocean Atlas 2013, Volume 3: Dissolved oxygen, apparent oxygen utilization, and oxygen saturation. S. Levitus, Ed., A. Mishonov Technical Ed.; NOAA Atlas NESDIS 75, 27 pp, 2014.

Gouretski, V., and Jahnke, K.: A new world ocean climatology. WHP Special Analysis Centre. Technical Report No. 3, Hamburg, Germany (unpublished), 1998.

References

Gouretski V. V., and Koltermann K.P.: WOCE Global Hydrographic Climatology. Berichte des BSH 35: 52 pp, 2004.

Grasse, P., Stichel, T., Stumpf, R., Stramma L., and M. Frank, M.: The distribution of neodymium isotopes and concentrations in the Eastern Equatorial Pacific: Water mass advection versus particle exchange, Earth and Planetary Science Letters, 353-354, 198-207, 2012.

Gruber, N., and Sarmiento, J. L.: Global patterns of marine nitrogen fixation and denitrification, Global Biogeochem. Cy., 11, 235-266, 1997.

Gruber, N.: The dynamics of the marine nitrogen cycle and its influence on atmospheric CO_2 variations, in The Ocean Carbon Cycle and Climate SE - 4, vol. 40, edited by M. Follows and T. Oguz, pp. 97–148, Springer Netherlands, 2004.

Guillén, O., Cárcamo, E., and Calientes, R.: Oxígeno disuelto, nutrientes y clorofila frente a la costa peruana durante El Niño 1987., Memorias del Simposio Internacional de los Recursos Vivos y las Pesquerías en el Pacífico Sud-Este. Rev. Comisión Permanente del Pacífico Sur., Número especial, 83-94, 1988.

Hahn, J., Brandt, P., Greatbatch, R. J., Krahmann, G., and Körtzinger, A.: Oxygen variance and meridional oxygen supply in the Tropical North East Atlantic oxygen minimum zone, Clim. Dyn., 2014.

Halpin, P. M., Strub, P. T., Peterson, W. T., and Baumgartner, T. R.: An overview of interactions among oceanography, marine ecosystems, climatic and human disruptions along the eastern margins of the Pacific Ocean, Rev. Chil. Hist. Nat., 77, 371-409, 2004.

Hamersley, M. R., Lavik, G., Woebken, D., Rattray, J. E., Lam, P., Hopmans, E. C., Sinninghe Damsté, J. S., Krüger, S., Graco, M., Gutiérrez, D., and Kuypers, M. M. M.: Anaerobic ammonium oxidation in the Peruvian oxygen minimum zone, Limnol. Oceanogr., 52, 923-933, 2007.

Hartin, C. A., Fine, R. A., Sloyan, B. M., Talley, L. D., Chereskin, T. K., and Happell, J.: Formation rates of Subantarctic mode water and Antarctic intermediate water within the South Pacific, Deep Sea Res. PtI, 58, 524-534, 2011.

Helly, J. J., and Levin, L. a: Global distribution of naturally occurring marine hypoxia on continental margins, Deep Sea Res. Part I Oceanogr. Res. Pap., 51(9), 1159–1168, 2004.

References

Holte, J. W., Talley, L. D., Chereskin, T. K., and Sloyan, B. M.: The role of air-sea fluxes in Subantarctic Mode Water formation, J. Geophys. Res., 117, C03040, 2012.

Hupe, A., and Karstensen, J.: Redfield stoichiometry in Arabian Sea subsurface waters, Global Biogeochem. Cy., 14, 357-372, 2000.

IOC, SCOR and IAPSO: The international thermodynamic equation of seawater: Calculations and use of thermodynamic properties. Intergovernmental Oceanographic Commission, Manuals and Guides No.56, UNESCO (English), 196 pp., 2010. Available from http://www.TEOS-10.org.

Jackett, D. R., and McDougall, T. J.: A Neutral Density Variable for the World's Oceans, J. Phys. Oceanogr., 27(2), 237–263, 1997.

Johnson, G. C., Sloyan, B. M., Kessler, W. S., and McTaggart, K. E.: Direct measurements of upper ocean currents and water properties across the tropical Pacific during the 1990s, Progr. Oceanogr., 52, 31-61, 2002.

Kalnay, E., Kanamitsu, M., Kistler, R., Collins, W., Deaven and D., and Gandin, L. The NCEP-NCAR 40-year reanalysis project. B. Am. Meteorol. Soc. 77, 437e471, 1996.

Kalvelage, T., Jensen, M. M., Contreras, S., Revsbech, N. P., Lam, P., Günter, M., LaRoche, J., Lavik, G., and Kuypers, M. M. M.: Oxygen sensitivity of anammox and coupled N-cycle processes in oxygen minimum zones, PLoS ONE, 6, e29299, 2011.

Kalvelage, T., Lavik, G., Lam, P., Contreras, S., Arteaga, L., Löscher, C. R., Oschlies, A., Paulmier, A., Stramma, L., and Kuypers, M. M. M.: Nitrogen cycling driven by organic matter export in the South Pacific oxygen minimum zone, Nat. Geosci., 6(3), 228–234, 2013.

Karstensen, J., and Tomczak, M.: Age determination of mixed water masses using CFC and oxygen data, J. Geophys. Res., 103, 18599-18609, 1998.

Karstensen J., and Tomczak M.: Manual for OMP Analysis Package for MATLAB, version 2.0. http://www.ldeo.columbia.edu/~jkarsten/omp_std/, 1999.

Karstensen, J.: Formation of the South Pacific shallow salinity minimum: A Southern Ocean pathway to the tropical Pacific, J. Phys. Oceanogr., 34, 2398–2412, 2004.

References

Karstensen, J., Stramma, L., and Visbeck, M.: Oxygen minimum zones in the eastern tropical Atlantic and Pacific oceans, Prog. Oceanogr., 77(4), 331–350, 2008.

Keeling, R. F., and Garcia, H. E.: The change in oceanic O(2) inventory associated with recent global warming., Proc. Natl. Acad. Sci. U. S. A., 99(12), 7848–53, 2002.

Kessler, W. S.: The circulation of the eastern tropical Pacific: A review, Progr. Oceanogr., 69, 181-217, 2006.

Kuypers, M. M. M., Lavik, G., Woebken, D., Schmid, M., Fuchs, B. M., Amann, R., Jørgensen, B. B., and Jetten, M. S. M.: Massive nitrogen loss from the Benguela upwelling system through anaerobic ammonium oxidation, P. Natl. Acad. Sci. USA, 102, 6478-6483, 2005.

Laird, N. P.: Panama Basin deep-water: properties and circulation, J. Mar. Res., 29, 226–234, 1971.

Lam, P., Lavik, G., Jensen, M. M., van de Vossenberg, J., Schmid, M., Woebken, D., Gutiérrez, D., Amann, R., Jetten, M. S. M., and Kuypers, M. M. M.: Revising the nitrogen cycle in the Peruvian oxygen minimum zone, P. Natl. Acad. Sci. USA, 106, 4752-4757, 2009.

Lankhorst, M., Send, U., and Biastroch, A.: Transport Time Series of Northeastern Atlantic Currents Derived from Long-Distance Geostrophy, Geophys. Res. Abstr., 10, 7962, EGU General Assembly 2008.

Leth, O., Shaffer, G., and Ulloa, O.: Hydrography of the eastern South Pacific Ocean: results from the Sonne 102 cruise, May–June 1995, Deep Sea Res. Part II Top. Stud. Oceanogr., 51(20-21), 2349–2369, 2004.

Lipschultz, F., Wofsy, S. C., Ward, B. B., Codispoti, L. A., Friedrich, G., and Elkins, J. W.: Bacterial transformations of inorganic nitrogen in the oxygen-deficient waters of the Eastern Tropical South Pacific Ocean, Deep Sea Res. Pt A., 37, 1513-1541, 1990.

Llanillo, P. J., Pelegrí, J. L., Duarte, C. M., Emelianov, M., Gasser, M., Gourrion, J., and Rodríguez-Santana, A.: Meridional and zonal changes in water properties along the continental slope off central and northern Chile, Ciencias Marinas; Vol 38, No 1B: Special issue on Descriptive Oceanography with Tracers in Coastal and Deep Oceans, 307-332, 2012.

References

Llanillo, P. J., Karstensen, J., Pelegrí, J. L., and Stramma, L.: Physical and biogeochemical forcing of oxygen and nitrate changes during El Niño/El Viejo and La Niña/La Vieja upper-ocean phases in the tropical eastern South Pacific along 86° W, Biogeosciences, 10, 6339-6355, 2013.

Luyten, J. R., Pedlosky, J., and Stommel, H.: The ventilated thermocline, J. Phys. Oceanogr., 13, 292–354, 1983.

Mackas, D. L., Denman, K. L., and Bennett, A. F.: Least squares multiple tracer analysis of water mass composition, J. Geophys. Res., 92, 2907-2918, 1987.

Mackas, D.L., Strub, P.T., Thomas, A., and Montecino, V.: Eastern ocean boundaries pan-regional overview. In: Robinson, A.R., Brink, K.H. (Eds.), The Sea, Vol. 14A: The Global Coastal Ocean: Interdisciplinary Regional Studies and Syntheses. Harvard University Press, 21-60, 2006.

Mantua, N. J., Hare, S. R., Zhang, Y., Wallace, J. M., and Francis, R. C.: A Pacific interdecadal climate oscillation with impacts on salmon production, B Am. Meteorol. Soc., 78, 1069-1079, 1997.

Matear, R. J., and Hirst, a. C.: Long-term changes in dissolved oxygen concentrations in the ocean caused by protracted global warming, Global Biogeochem. Cycles, 17(4), 2003.

McDougall, T. J.: Neutral Surfaces, J. Phys. Oceanogr., 17(11), 1950–1964, 1987.

McDougall, T. J., and Klocker, A.: An approximate geostrophic stream function for use in density surfaces, Ocean Model., 32(3-4), 105–117, 2010.

Morales, C., Hormazábal, S., and Blanco, J. L.: Interannual variability in the mesoscale distribution of the depth of the upper boundary of the oxygen minimum layer off northern Chile (18º–24ºS): Implications for the pelagic system and biogeochemical cycling, J. Mar. Res., 57, 909-932, 1999.

Naqvi, S. W. A., Bange, H. W., Farías, L., Monteiro, P. M. S., Scranton, M. I., and Zhang, J.: Marine hypoxia/anoxia as a source of CH_4 and N_2O, Biogeosciences, 7(7), 2159–2190, 2010.

Niiler, P.P., Maximenko, N.A. and McWilliams, J.C.: Dynamically balanced absolute sea level of the global ocean derived from near-surface velocity observations. Geophys. Res. Lett. 30, 22., 2003.

References

NOAA PMEL: Impacts of El Niño and benefits of El Niño prediction. NOAA Pacific Marine Environmental Laboratory, 2009. http://www.pmel.noaa.gov/tao/elnino/impacts.html

Oguz, T., Ducklow, H. W., and Malanotte-Rizzoli, P.: Modeling distinct vertical biogeochemical structure of the Black Sea: Dynamical coupling of the oxic, suboxic, and anoxic layers, Global Biogeochem. Cycles, 14(4), 1331–1352, 2000.

Paulmier, A., Ruiz-Pino, D., Garçon, V., and Farías L.: Maintaining of the East South Pacific Oxygen Minimum Zone (OMZ) off Chile, Geophys. Res. Lett., 33, L20601, 2006.

Paulmier, A., and Ruiz-Pino, D.: Oxygen minimum zones (OMZs) in the modern ocean, Progr. Oceanogr., 80, 113-128, 2009.

Pastor, M. V., Peña-Izquierdo, J., Pelegrí, J. L., and Marrero-Díaz, A.: Meridional changes in water properites of NW Africa during November 207/2008, Cienc. Mar., 38, 233, 244, 2012.

Penven, P.: Average circulation, seasonal cycle, and mesoscale dynamics of the Peru Current System: A modeling approach, J. Geophys. Res., 110, C10021–C10021, 2005.

Pérez, F. F., Mourino, C., Fraga, F., and Ríos, A. F.: Displacement of water masses and remineralization rates off the Iberian Peninsula by nutrient anomalies, J. Mar. Res, 51, 1–24, 1993.

Pérez, F. F., Mintrop, L., Llinás, O., González-Dávila, M., Castro, C. G., Álvarez, M., Körtzinger, A., Santana-Casiano, M., Rueda, M. J., and Ríos, A. F.: Mixing analysis of nutrients , oxygen and inorganic carbon in the Canary Islands region, J. Mar. Syst, 28, 183–201, 2001.

Philander, S. G. H.: El Niño Southern Oscillation phenomena, Nature, 302, 295-301, 1983.

Pizarro, O.: Dynamics of seasonal and interannual variability of the Peru-Chile Undercurrent, Geophys. Res. Lett., 29(12), 1581, 2002.

Plattner, G. K., Joos, F., and Stocker, T. F.: Revision of the global carbon budget due to changing air-sea oxygen fluxes, Glob. Biogeochem. Cycles, 16(4), 2002.

Poole, R., and Tomczak, M.: Optimum multiparameter analysis of the water mass structure in the Atlantic Ocean thermocline, Deep Sea Res. PtI, 46, 1895-1921, 1999.

References

Redfield, A. C., Ketchum, B. H., and Richards, F. A.: The influence of organisms on the composition of sea-water, in The Sea: ideas and observations on progress in the study of the seas (vol. 2), edited by M. N. (ed) Hill, pp. 26–77, Wiley, London., 1963.

Reid, J. L.: The shallow salinity minima of the Pacific Ocean, Deep Sea Res., 20, 51-68, 1973.

Reid, J. L.: On the total geostrophic circulation of the Pacific Ocean: Flow patterns, tracers, and transports. Prog. Oceanog. Vol. 39, pp. 263-352, 1997.

Roemmich, D., Gilson, J., Davis, R., Sutton, P., Wijffels, S., and Riser, S.: Decadal spinup of the South Pacific Subtropical Gyre, J. Phys. Oceanogr., 37, 162-173, 2007.

Sabine, C.L., Key, R.M., Kozyr, A., Feely, R.A., Wanninkhof, R., Millero, F.J., Peng, T.-H., Bullister, J.L., and Lee, K.: Global Ocean Data Analysis Project: Results and Data. ORNL/CDIAC-145, NDP-083. Carbon Dioxide Information Analysis Centre, Oak Ridge National Laboratory, U.S. Department of Energy, Oak Ridge, Tennessee, 110 pp. (unpublished), 2005.

Schmidtko, S., and Johnson, G. C.: Multidecadal warming and shoaling of Antarctic Intermediate Water, J. Climate, 25, 207-221, 2012.

Schmittner, A., Oschlies, A., Matthews, H. D., and Galbraith, E. D.: Future changes in climate, ocean circulation, ecosystems, and biogeochemical cycling simulated for a business-as-usual CO_2 emission scenario until year 4000 AD, Global Biogeochem. Cycles, 22(1), 2008.

Schneider, W., Fuenzalida, R.F., Núñez R.G., Garcés-Vargas, J., Bravo, L., and Figueroa, D.L.: Discussion of the Humboldt Current system and water masses in the north zone and center off Chile. Cienc. Tecnol. Mar., 30 (1), 21-36, 2007.

Scripps Institution of Oceanography: Physical and chemical data from SCORPIO Expedition in the South Pacific Ocean. USNS Eltain Cruises 28 and 29, 12 March–21 July 1967. SIO Reference 69-15; WHOI Reference 69-56, La Jolla, CA, 89pp., 1969.

Scripps Institution of Oceanography: Data report physical and chemical data. PIQUERO Expedition, 16 December 1968–16 April 1969. SIO Reference 74-27, 59pp., 1974.

Shaffer, G., Hormazabal, S., Pizarro, O., and Ramos, M.: Circulation and variability in the Chile Basin, Deep Sea Res. Part I Oceanogr. Res. Pap., 51(10), 1367–1386, 2004.

References

Shaffer, G., Olsen, S. M., and Pedersen, J. O. P.: Long-term ocean oxygen depletion in response to carbon dioxide emissions from fossil fuels, Nat. Geosci., 2(2), 105–109, 2009.

Silva, N., and Konow, D.: Contribución al conocimiento de las masas de agua en el Pacífico Sudoriental Expedición Krill. Crucero 3–4 July–August 1974, Rev. Comis. Permanente Pacífico Sur, 3, 63–75, 1975.

Silva, N., Rojas, N., and Fedele, A.: Water masses in the Humboldt Current System: Properties, distribution, and the nitrate deficit as a chemical water mass tracer for Equatorial Subsurface Water off Chile, Deep Sea Res. PtII, 56, 1004-1020, 2009.

Smethie, W. M.: Nutrient regeneration and denitrification in low oxygen fjords, Deep Sea Res. Part A. Oceanogr. Res. Pap., 34(5-6), 983–1006, 1987.

Stommel, H., Stroup, E.D., Reid, J. L., and Warren, B.A.: Transpacific hydrographic sections at Lats. 43°S and 28°S: the SCORPIO expedition—I. Preface, Deep Sea Res. Oceanogr. Abstr., 20(1), 1–7, 1973.

Stommel, H.: Determination of water mass properties of water pumped down from the Ekman layer to the geostrophic flow below., Proc. Natl. Acad. Sci. U.S.A., 76(7), 3051–3055, 1979.

Stramma, L., Peterson, R. G., and Tomczak, M.: The South Pacific Current, J. Phys. Oceanogr., 25, 77-91, 1995.

Stramma, L., Johnson, G. C., Sprintall, J., and Mohrholz, V.: Expanding oxygen-minimum zones in the Tropical Oceans, Science, 320, 655-658, 2008.

Stramma, L., Johnson, G. C., Firing, E., and Schmidtko, S.: Eastern Pacific oxygen minimum zones: supply paths and multidecadal changes, J. Geophys. Res., 115, C09011, 2010a.

Stramma, L., Schmidtko, S., Levin, L. A., and Johnson, G. C.: Ocean oxygen minima expansions and their biological impacts, Deep Sea Res. PtI, 57, 587-595, 2010b.

Stramma, L., Prince, E. D., Schmidtko, S., Luo, J., Hoolihan, J. P., Visbeck, M., Wallace, D. W. R., Brandt, P., and Kortzinger, A.: Expansion of oxygen minimum zones may reduce available habitat for tropical pelagic fishes, Nature Clim. Change, 2, 33-37, 2012a.

References

Stramma, L., Oschlies, A., and Schmidtko, S.: Mismatch between observed and modeled trends in dissolved upper-ocean oxygen over the last 50 yr, Biogeosciences, 9, 4045-4057 2012b.

Stramma, L., Bange, H. W., Czeschel, R., Lorenzo, A., and Frank, M.: On the role of mesoscale eddies for the biological productivity and biogeochemistry in the eastern tropical Pacific Ocean off Peru, Biogeosciences, 10, 7293-7306, 2013.

Strub, P., Mesias, J., Montecino, V., Rutllant, J., and Salinas, S.: Coastal ocean circulation off western South America, in: The Sea: The global coastal ocean, edited by: Robinson, A. and B., K. (eds.), Wiley, New York, 272-313, 1998.

Talley, L. D., Pickard, G. L., Emery, W. J., and Swift, J. H.: Descriptive Physical Oceanography, Elsevier., 2011.

Thamdrup, B., Dalsgaard, T., Jensen, M. M., Ulloa, O., Farías, L., and Escribano, R.: Anaerobic ammonium oxidation in the oxygen-deficient waters off northern Chile, Limnol. Oceanogr., 51, 2145-2156, 2006.

Thomas, W. H.: On denitrification in the northeastern tropical Pacific Ocean, Deep Sea Res. Oceanogr. Abstr., 13(6), 1109–1114, 1966.

Tomczak, M.: A multi-parameter extension of temperature/salinity diagram techniques for the analysis of non-isopycnal mixing, Prog. Oceanogr., 10(3), 147–171, 1981.

Tomczak, M., and Large, D. G. B.: Optimum multiparameter analysis of mixing in the thermocline of the Eastern Indian Ocean, J. Geophys. Res., 94, 16141-16149, 1989.

Tomczak, M., and Godfrey, J. S.: Regional Oceanography: An Introduction (2nd edition), Daya Publising House,Delhi., 2003.

Tomczak, M., and Liefrink, S.: Interannual variations of water mass properties and volumes in the Southern Ocean, Ocean Sci. Discuss., 3(3), 199–219, 2006.

Tsuchiya, M.: Subsurface countercurrents in the eastern equatorial Pacific, J. Mar. Res., 33, 145–175, 1975.

Tsuchiya, M., and Talley, L. D.: A Pacific hydrographic section at 88°W: Water-property distribution, J. Geophys. Res., 103, 12899-12918, 1998.

References

Vaquer-Sunyer, R., and Duarte, C. M.: Thresholds of hypoxia for marine biodiversity, P. Natl. Acad. Sci. USA, 2008.

Whalen, C. B., Talley, L. D., and MacKinnon, J. A.: Spatial and temporal variability of global ocean mixing inferred from Argo profiles, Geophys. Res. Lett., 39(18), 2012.

Wooster, W.S., Chow, T.J., and Barrett, I.: Nitrite distribution in Peru Current waters, J. Mar. Res., 23 (3), 210–221, 1965.

Wyrtki, K.: The oxygen minima in relation to ocean circulation, Deep Sea Res. Oceanogr. Abstr., 9(1-2), 11–23, doi:10.1016/0011-7471(62)90243-7, 1962.

Wyrtki, K.: Oceanography of the eastern equatorial Pacific Ocean, Ocean. Mar. Biol. Ann. Rev, 4, 33–68, 1966.

Wyrtki, K.: Circulation and water masses in the eastern equatorial Pacific Ocean, Int. J. Oceanol. Limnol., 1(2), 117-147, 1967.

Zuta, S., and Guillén, O.: Oceanografía de las aguas costeras del Perú, Bol. Inst. Del Mar de Perú, 2, 157-324, 1970.

ACKNOWLEDGEMENTS/AGRADECIMIENTOS

En primer lugar me gustaría agradecer a mi director de tesis, José Luis Pelegrí, por su trato cercano y por su puerta siempre abierta. Gracias por enseñarme a trabajar de manera autónoma, por ayudarme a ganar confianza poniendo mis pequeños logros como avances positivos e interesantes. Gracias por haberme dado la libertad de investigar aquello que me parecía más interesante. Gracias por tu flexibilidad y por haberme dado la oportunidad de participar en campañas oceanográficas en varios océanos. Gracias también por el apoyo económico y por tu comprensión y cercanía en este acelerado tramo final de la tesis. Agradezco también a mis compañeros doctorandos por su compañía y apoyo y por los buenos ratos pasados en medio del océano o alrededor de unas cervezas. En especial agradezco a Suso por su amistad y sus consejos ya fuese entre las olas o discutiendo nuestras dudas científicas. Gracias a Fernando Mat. y al Dr. Carrillo por su buena acogida a mi llegada a Barcelona y por darme tan buenas energías. Gracias a Sergio, a Paola, a Carmen, a Patricia, a Miquel, a Kintxo, a mis compañeras de despacho, a mis compañeros de campañas y a todos los demás que habéis compartido conmigo distintas fases de este proceso, gracias por vuestra cercanía en esta etapa tan especial. Agradezco a Lothar Stramma por haberme acogido en Alemania durante unos meses y haberme transmitido su manera de entender la ciencia. A Johannes Karstensen, a Lynne Talley y a Matthias Lankhorst por su buena acogida y consejos científicos. Agradezco a la tripulación del BIO Hespérides su buena disposición y buen ambiente. Agradezco también al CSIC el haberme dado la oportunidad de convertirme en científico junior gracias a una beca JAE Predoc. Por ultimo agradezco a mi madre, a mi hermano y a Bea su fe constante en mí y las energías y optimismo que me han transmitido a lo largo de los años. Sin Bea esta tesis tendría un aspecto mucho más gris y simplón, gracias por tu ayuda fundamental con la maquetación y por tu compañía y los buenos momentos compartidos a lo largo de este camino.